NASA CR - 165,253
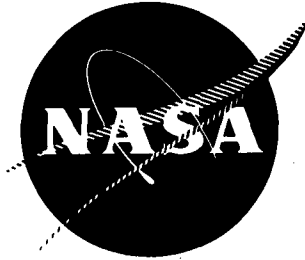
NASA-CR-165253

1981 0016609

ION AND ADVANCED ELECTRIC THRUSTER RESEARCH

PREPARED FOR

LEWIS RESEARCH CENTER

NATIONAL AERONAUTICS AND SPACE ADMINISTRATION

GRANT NGR-06-002-112

Annual Report

December 1980

Paul J. Wilbur
Department of Mechanical Engineering
Colorado State University
Fort Collins, Colorado

1. Report No. NASA CR 165253	2. Government Accession No.	3. Recipient's Catalog No.
4. Title and Subtitle Ion and Advanced Electric Thruster Research		5. Report Date Dec. 1980
		6. Performing Organization Code
7. Author(s) Paul J. Wilbur		8. Performing Organization Report No.
9. Performing Organization Name and Address Department of Mechanical Engineering Colorado State University Fort Collins, Colorado 80523		10. Work Unit No.
		11. Contract or Grant No. NGR-06-002-112
12. Sponsoring Agency Name and Address National Aeronautics and Space Administration Washington, D.C. 20546		13. Type of Report and Period Covered Contractor Report Dec. 1. 1979 – Dec. 1, 1980
		14. Sponsoring Agency Code
15. Supplementary Notes Grant Monitor – William Kerslake, NASA Lewis Research Center, Cleveland, Ohio 44135.		

16. Abstract
    A phenomenological model of the orificed, hollow cathode based on the field-enhanced, thermionic mechanism of electron emission is presented. Experimental results obtained on a mercury hollow cathode are presented and they are seen to support the validity of the model. High frequency oscillations associated with the orificed, hollow cathode are shown to be a consequence of current flow through the cathode orifice. A procedure for Langmuir probing of the hollow cathode discharge and analyzing the resulting probe characteristics is discussed. The results of sputter yield measurements made for molybdenum, tantalum, type 304 stainless steel and copper surfaces being bombarded by low energy argon or mercury ions are presented. The experimentally determined effects of nitrogen and alternated copper layers on the sputter yields of molybdenum, tantalum and 304 stainless steel are also discussed. A dynamic model of electrothermal rocket and ramjet thrusters is developed. The gross performance of these devices is compared to that of an electromagnetic gun for the case of a high acceleration, earth launch mission. The theoretical performance of electrothermal rockets and ramjets is shown to be comparable to that of the electromagnetic gun. The experimental apparatus that will be used to measure the divergence and deflection characteristics of ion beamlets as a function of grid aperture misalignment is discussed. Preliminary results obtained with this apparatus are presented. The experimentally determined operating characteristics of two hollow cathodes connected in parallel to supply electrons to a thruster discharge chamber are presented. Results show these cathodes can be started and forced to share equally in the required electron emission. A model describing the effect of primary electron energy on the ion velocity needed for a stable sheath (Bohm velocity) is presented.

17. Key Words (Suggested by Author(s)) Electrostatic Thruster Hollow Cathode Electrothermal Thruster	18. Distribution Statement Unclassified – Unlimited		
19. Security Classif. (of this report) Unclassified	20. Security Classif. (of this page) Unclassified	21. No. of Pages 130	22. Price*

* For sale by the National Technical Information Service, Springfield, Virginia 22161

N81-25144

TABLE OF CONTENTS

Table of Contents (Continued)

LIST OF FIGURES

iv

LIST OF TABLES

ION EXTRACTION FROM A PLASMA

Graeme Aston

An experimental investigation of the physical processes governing ion extraction from a plasma was completed during this grant period. The results of this work are described in Reference 1, so they will not be reproduced here. In Reference 1 the screen hole plasma sheath of a multi-aperture ion accelerator system is defined by equipotential plots for a variety of accelerator system geometries and operating conditions. A preacceleration region, which might be called the sheath, having a thickness of at least fifteen Debye lengths is shown to be typical. The electron density variation within the sheath is shown to satisfy a Maxwell-Boltzmann density distribution at an effective electron temperature dependent on the discharge plasma primary-to-Maxwellian electron density ratio. Plasma ion flow up to and through the sheath is shown to be predominately one-dimensional with the ions entering the sheath at a modified Bohm velocity. Low values of the screen grid thickness-to-screen hole diameter ratio are shown to give good ion focusing and high extracted ion currents because of the effect of screen webbing on ion focusing.

BAFFLE APERTURE DESIGN STUDY OF HOLLOW CATHODE EQUIPPED ION THRUSTERS

John Brophy

A simple, theoretical model which can be used as an aid in the design of the baffle aperture region of a hollow cathode equipped ion thruster was developed during this grant period. The results of this study are described in detail in Reference 2 and its contents will also not be

reproduced here. The document contains an analysis of the ion and electron currents in both the main and cathode discharge chambers. From this analysis a model of current flow through the aperture, which is required as an input to the design model, is developed. This model is verified experimentally. The dominant force driving electrons through the aperture is shown to be the force due to the electrical potential gradient. The diffusion process is modeled according to the Bohm diffusion theory. A number of simplifications are made to limit the amount of detailed plasma information required as input to the model and to facilitate the use of the model in thruster design. This simplified model can be used to predict the magnetic field intensity required to produce a given current through the baffle aperture in terms of the anode/keeper voltage difference and the baffle aperture/magnetic field geometric parameters. The magnetic field intensities computed from the model are shown to be remarkably consistent with experimentally measured values obtained with a given thruster geometry over substantial changes in operating conditions. Dramatic changes in the thruster geometry can introduce effects that cause a coefficient in the equation describing the model to vary by as much as a factor of two. The design usefulness of the model may be limited by this factor of two un-certainty, which exists when the thruster geometry is altered substantially, and by the accuracy to which the plasma parameters required as inputs to the model can be specified.

A PHENOMENOLOGICAL MODEL DESCRIBING
ORIFICED, HOLLOW CATHODE OPERATION

Dan Siegfried

Because of the importance of the orificed, hollow cathode to ion thruster design and performance, there has been considerable interest in recent years in understanding hollow cathode physical processes and in developing a model for cathode operation. Numerous experiments have been performed under the support of this grant which have provided important physical data regarding hollow cathode operation. These data have included plasma properties within the cathode, insert temperature profiles, internal cathode pressure, and emission current density profiles over a wide range of cathode operating conditions.[3,4] The physical understanding gained through this work has led to the development of a simple phenomenological model to describe cathode operation. This report will discuss our current understanding of the physical processes which take place inside the hollow cathode and describe the proposed model. Work on the model has suggested additional experiments for verifying the model and these will also be discussed.

Background

The orificed, hollow cathode in its simplest form is shown in Fig. 1. The cathode consists of an outer refractory metal tube, usually tantalum, covered on its downstream end by an orifice plate usually made of thoriated tungsten. The cathode also normally incorporates a refractory metal insert either coated or impregnated with such chemicals as various barium compounds, which aid the emission process by reducing the work function of
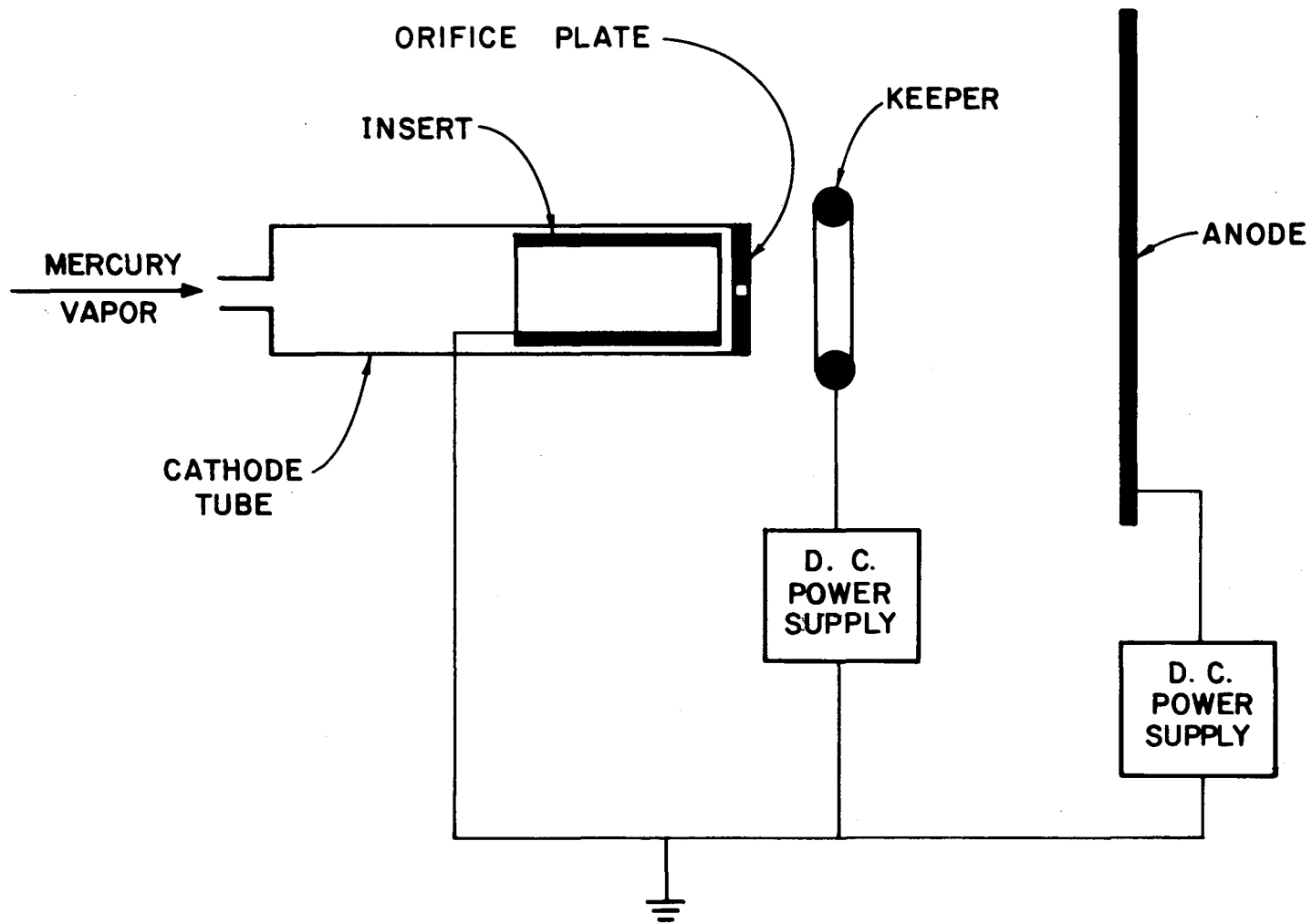
Fig. 1. Typical Orificed, Hollow Cathode

the insert surface. Cathodes used in ion thrusters typically have tube inside diameters of a few millimeters and orifice diameters of a few tenths to one millimeter. The insert length is usually a few tube diameters. The electron current is collected by an anode biased positive of the cathode. Thruster applications also utilize a small secondary anode, called a keeper, which acts to maintain a stable discharge in the event of fluctuations in discharge chamber conditions. Mercury vapor flows through the cathode in the direction shown in the figure. An external heater (not shown) is normally used to heat the cathode as an aid to starting the emission process. However, the process is self-sustaining once the cathode discharge is established and the heater can then be turned off.

The earlier experimental studies mentioned in the introduction have led to a number of important conclusions which have helped to define the nature of the hollow cathode operation. These will be summarized very briefly here because they form the basis of the proposed phenomenological model. Langmuir probe measurements made within the cathode indicated that there is a very intense plasma discharge set up within the cathode.[3] For emission currents of a few amperes, typical plasma conditions found in the vicinity of the orifice plate were a plasma density of a few times 10^{14} cm^{-3}, a plasma potential of $\sim$ 8 volts, and an electron temperature of $\sim$ 0.8 eV. A series of experiments using a quartz body test cathode to isolate various cathode surfaces electrically was used to pinpoint the emission site in the cathode and to determine emission current profiles for the insert.[4] That study showed that the insert accounts for approximately 85% of the total emission current and that the emission region is localized on the last few millimeters at the downstream end of the insert. This same

series of tests also provided insert temperature profiles over a wide range of operating conditions. As expected the highest insert temperature was found to correspond to the location of the emission region, with temperatures on the order of 1000°C being typical for an emission current of a few amperes. Furthermore, it was found that the orifice diameter and mass flow rate were important only to the extent that they affected the internal cathode pressure, and that the cathode pressure was an important parameter affecting the emission temperature. The product of cathode internal pressure and emission surface diameter was suggested as an important parameter in determining the emission location and keeper voltage. This parameter is proportional to the ratio of the insert diameter to the electron mean free path, and therefore, is also proportional to the probability of an inelastic collision of an electron as it makes a single traverse of the cathode diameter. The simultaneous measurement of emission current and emission surface temperature in these studies provided sufficient information to facilitate estimation of the emissive surface work function. This provided reasonable evidence that the emission mechanism of the cathode could be that of field-enhanced, thermionic emission.

A Phenomenological Model

The following physical description of orificed, hollow cathode operation has emerged from these studies. The cathode orifice maintains a high neutral density inside the cathode by restricting the propellant flow and it also provides a current path to the downstream discharge. The electron emission comes uniformly from a narrow ($\sim$ 2 mm) band on the downstream end of the insert. The electrons are produced at the surface of the insert by field-enhanced, thermionic emission (the very strong electric field is a

consequence of a very dense plasma and the resulting potential drop across a very thin plasma sheath). The electrons produced at the insert surface are accelerated across the plasma sheath by a potential of 8 to 10 V. Since the mean free path for inelastic collisions of these energetic electrons is on the order of the internal cathode diameter, the "ion production" region can be idealized to be the volume circumscribed by the emitting region of the insert. The dense internal plasma is established by the ionization taking place in this region. Ions produced in this volume diffuse out of it at the Bohm velocity. These ions strike the insert surface with sufficient energy to heat it to the temperature necessary to provide the required electron emission. The emission surface temperature, however, is determined not only by the emission current but also by the local plasma properties.

The plasma properties in the ion production region are coupled into the problem by the energy balance at the insert surface in the following manner. The plasma properties determine the ion flux and therefore the energy input to the emission surface. For a given emission current, the surface temperature is determined by the energy balance which demands that the thermal losses from the surface due to electron production, radiation and conduction are balanced by the energy input from the ion flux. The plasma properties also affect the required emission temperature because they determine the magnitude of the electric field at the emission surface and thereby the degree of field-enhancement in the emission process. Therefore, for a given emission current the surface temperature and plasma properties must be consistent to the extent that they satisfy the energy balance at the surface. All cathode surfaces which contact the plasma receive ion currents proportional to the Bohm velocity and the plasma

density adjacent to the surface. Electron emission, on the other hand, can be assumed to come only from the 2 mm band on the downstream end of the insert. The total emission current* from the cathode is equal to the sum of the ion currents to the various cathode surfaces and the current of the emitted electrons.

Certain aspects of this phenomenological model can be expressed analytically in a simple form which will allow comparison with experimental results. The plasma density adjacent to a particular surface (n) can be calculated based on the Bohm condition using

$$n = \frac{j_i}{ev_{Bohm}} = \frac{I_i}{Ae\left[\dfrac{kT_e}{m_i}\right]^{\frac{1}{2}}} \tag{1}$$

where I_i is the ion current to the surface, A is the surface area, T_e is the Maxwellian electron temperature (°K), m_i is the ion mass, e is the electronic charge, and k is Boltzmann's constant. For an electron emitting surface the measured current to the surface is determined by both collected ions and emitted electrons, so that the total current density to the surface is

$$j_{total} = j_i + j_e \tag{2}$$

where j_i is the ion current density and j_e is the electron emission current density. The ratio of ion to electron currents can be estimated from an energy balance on the emitting surface. In such a balance the ion heating power is equated to power conducted and radiated from the surface plus the power required to boil off electrons. The equation[5] describing this is

---

* Total emission current (I_E) as used here refers to the total power supply current, that is the keeper current and the anode current.

$$j_e \, \overline{\phi}_e + \dot{q} = j_i \, (V_c + V_i - \phi_s) \tag{3}$$

where $\overline{\phi}_e$ is the effective work function of the surface, $\dot{q}$ is the thermal heat flux away from the surface, V_c is the potential drop across the plasma sheath, V_i is the ionization potential, and ϕ_s is the work function of the surface material (a material property). Equations 2 and 3 can be combined to give the electron emission current density from the surface,

$$j_e = \frac{j_{total} - a \, \dot{q}}{1 + a \, \overline{\phi}_e} \tag{4}$$

where

$$a \equiv (V_c + V_i - \phi_s)^{-1} \, .$$

In general the thermal loss is a function of the surface temperature and the cathode thermal design. For the quartz test cathode which will be discussed later most of the thermal loss is due to radiation from the outer surface of the insert to rather cold external surfaces, and can be estimated from

$$\dot{q} \approx \varepsilon \sigma T^4 \tag{5}$$

where ε is the emissivity (~ 0.5 for tantalum), σ is the Stefan-Boltzmann constant, and T is the surface temperature. Emission from the surface is assumed to be given by the Schottky equation[5] for field-enhanced, thermionic emission

$$j_e = A_0 T^2 \exp\left[-\frac{e\overline{\phi}_e}{kT}\right] \tag{6}$$

where $A_0 = 120$ A/cm^{2}K^2 and the other parameters are as previously defined. The average effective work function $\overline{\phi}_e$ is given by

$$\overline{\phi}_e = \phi_s - \left[\frac{e|E|}{4\pi\varepsilon_0}\right]^{\frac{1}{2}} \tag{7}$$

where ε_o is the permittivity of free space and E, the electric field adjacent to the surface, can be estimated using

$$E = \frac{-dV}{dx} = \frac{-4}{3} \frac{V_c}{\lambda_D} = \frac{-4V_c}{3} \left[\frac{ne^2}{\varepsilon_o kT_e} \right]^{\frac{1}{2}} . \qquad (8)$$

Here the factor of 4/3 comes from Child's Law considerations[5] and the sheath thickness is estimated as one Debye length (λ_D).

This model as it stands does not contain sufficient detail to make a priori predictions of plasma properties or their spatial variation. The model, therefore, cannot explain or predict the location at which the emission will take place or the performance, i.e. power requirements, of the cathode. This would require a more detailed modeling of the plasma processes in the ion production region. However, the model can provide an estimate of the insert temperature and this is a critical parameter in determining both the cathode lifetime and performance. This can be done for example, by picking an electron temperature and the plasma potential. These properties have been measured experimentally and found to be rather insensitive to operating conditions with typical values of ~0.8 eV and ~8.0 volts respectively for a cathode operating at a few amperes of discharge current. Using these values together with a specified surface work function (ϕ_s) and the desired emission current (j_{total}), Eqs 1 through 8 can be solved to provide the emission surface temperature (T). Note that the solution scheme would generally be an iterative one requiring an initial guess of a value for either j_e or T.

Comparison with Experiment

The model has been found to be consistent with the experimental results obtained to date. As a result of the work on the model a number of additional experiments were proposed. One such experiment was an overall

current balance on all of the cathode surfaces which can contribute to the total emission current. Such an experiment would provide a means of testing the assumptions related to the ion production region such as the extent of the region, the applicability of the Bohm velocity, and the energy balance at the insert surface.

The test cathode designed and built to facilitate the measurement of the currents necessary to perform the overall current balance is shown in Fig. 2. The cathode was fabricated from a quartz tube such that all of the internal surfaces were covered with tantalum foil and each surface of interest was isolated as a separate electrode. The insert was made 2.2 mm long to test the assumption regarding the location and extent of the emission region. Both the insert and the cathode tube were coated with the low work function chemical R-500*. This cathode had an inner diameter of 3.9 mm and an orifice diameter of 0.76 mm. The cathode discharge was coupled to a cylindrical anode which was completely enclosed within a stainless steel ground tube covered on its downstream end by a fine mesh screen. The current from each of the surfaces shown in Figure 2 was measured separately for total emission currents of 1.3, 2.3, 3.3 and 4.3 A at a flow rate ($\dot{m}$) of ∿100 mA. Data were also collected for an emission current of 3.3 A at internal cathode pressures (P) ranging from 1.3 to 5.8 torr. Internal pressures were measured using a U-tube manometer as described in the report of an earlier experimental study.[4] The internal pressure was adjusted by venting a portion of the mercury flow into the bell jar using a special throttle valve also described in that report. The results of these

---

* A double carbonate mixture - (Ba/Sr) CO_3 - manufactured by the J. T. Baker, Co.; Phillipsburg, New Jersey.
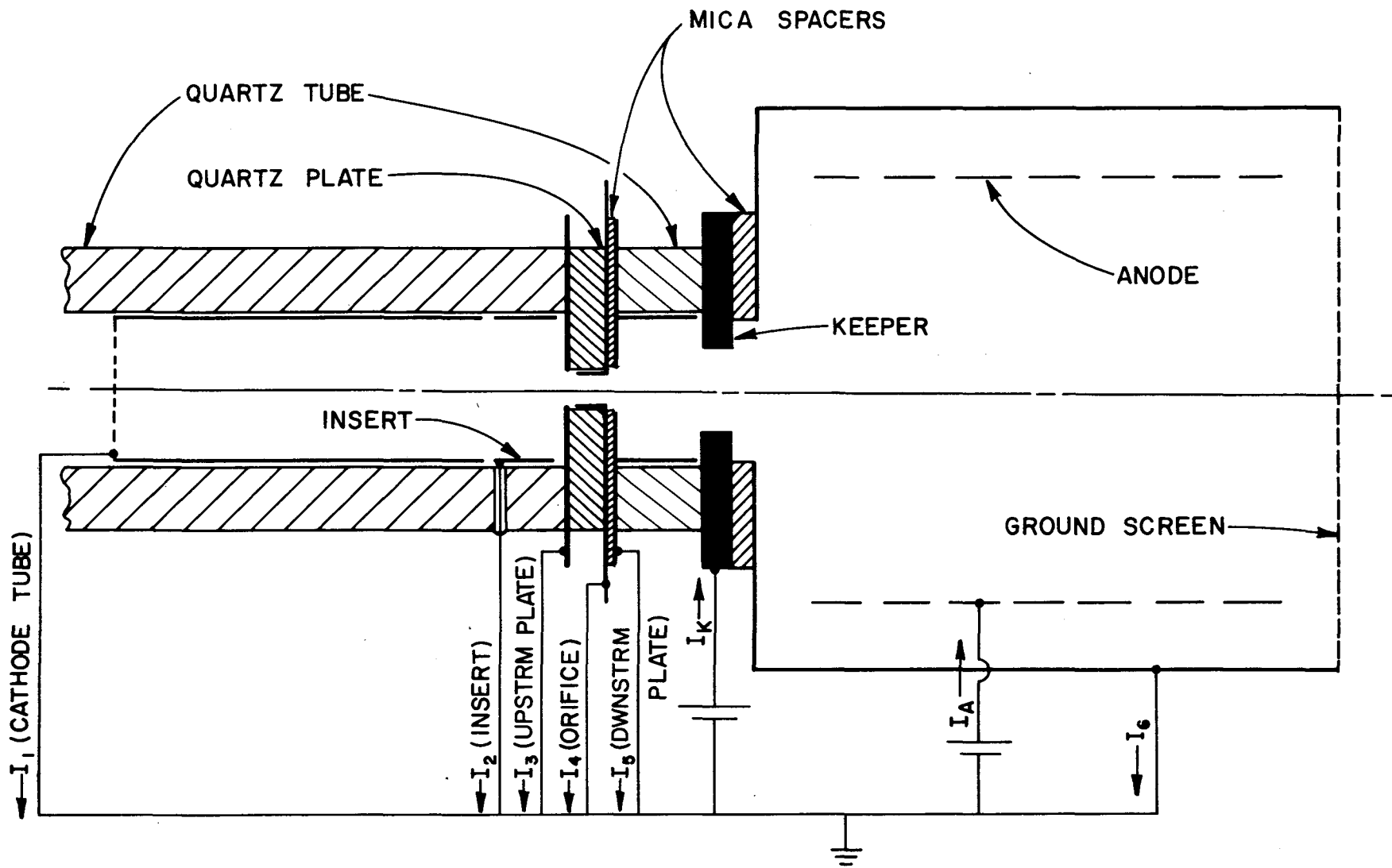
Fig. 2.   Test Cathode for Current Accounting

12

experiments are shown in Table I where the currents - I_1, I_2, etc. - are those from the surfaces identified in Fig. 2 and suggested by the diagram attached to Table I. The current I_T is the sum of these numbered currents. It appears that all of the currents necessary to perform the overall cathode current balance are accounted for because the total of the currents (I_T) agrees with the total emission current ($I_E = I_A + I_K$) within a few percent.

Plasma Density in the Ion Production Region

One of the purposes of this test was to determine the fraction of the total emission current resulting from the ion current returning to cathode potential surfaces. The insert segment, which in this test was 2.2 mm long, accounted for ~85% of the total emission current except at pressures below about 3 torr. According to the simple model proposed earlier, this insert current is equal to the sum of the electron emission current (given by the Schottky equation - Eq.6) and the ion collection current (based on the Bohm velocity - Eq.1). The ratio of the ion current to the electron current for the insert was estimated from the insert energy balance (Eq. 4) and was found to be in the range of 0.17 to 0.24 for the operating conditions of Table I. Using this ratio together with the measured insert current (I_2) one can estimate the ion current to the insert.

The cathode model which has been proposed, also assumed that electron emission took place only at the insert surface and that the current contribution of the other cathode surfaces is due solely to the ion currents to these surfaces. This assumption was tested experimentally by biasing each of the electrode surfaces (except the insert) with respect to ground and observing the effect on the collected current. A typical voltage current
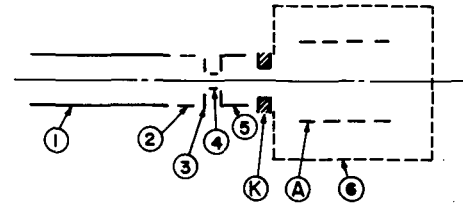
TABLE I

Cathode Current Accounting

$\dot{m}$(mA)	$P_{(torr)}$	I_A(A)	V_A(V)	I_K(A)	V_K(V)	I_1(A) (Cathode tube)	I_2(A) (Insert)	I_3(A) (Upstm. Orifice Plate)	I_4(A) (Orifice)	I_5(A) (Downstm. Orifice Plate	I_6(A) (Ground Screen)	I_T(A)	T_{insert} (°C)
102	3.6	1.0	15.8	0.3	13.9	0.03	1.10	0.10	0.04	∿0	0.002	1.27	965
102	4.6	2.0	14.2	0.3	12.8	0.05	1.99	0.16	0.09	0.01	0.004	2.30	1009
106	5.5	3.0	15.2	0.3	14.0	0.07	2.82	0.23	0.17	0.02	0.007	3.31	1039
105	6.2	4.0	15.7	0.3	14.2	0.09	3.63	0.29	0.26	0.025	0.013	4.30	1070
110	5.8	3.0	15.1	0.3	15.0	0.05	2.82	0.24	0.17	0.015	0.007	3.30	--
78	4.1	3.0	15.1	0.3	15.5	0.14	2.78	0.24	0.11	0.01	0.007	3.29	--
62	3.2	3.0	15.2	0.3	16.2	0.25	2.72	0.23	0.09	0.01	0.006	3.31	--
35	1.8	3.0	19.0	0.3	17.4	1.25	1.76	0.18	0.05	0.01	0.006	3.26	--
25	1.3	3.0	24.1	0.3	17.1	1.90	1.23	0.14	0.04	∿0	0.006	3.32	--

TABLE II

Calculated Plasma Densities

Cathode Internal Pressure (torr)	Total Emission Current I_E(A)	Insert Density n_2(cm^{-3})	Density Immediately Upstream of Orifice Plate n_3(cm^{-3})	Density Within Orifice n_4(cm^{-3})	Density Immediately Downstream of Orifice Plate n_5(cm^{-3})
3.6	1.3	0.79×10^{14}	0.91×10^{14}	0.75×10^{14}	∿0
4.6	2.3	1.21×10^{14}	1.46×10^{14}	1.70×10^{14}	2.39×10^{12}
5.5	3.3	1.58×10^{14}	2.10×10^{14}	3.21×10^{14}	4.78×10^{12}
6.2	4.3	1.96×10^{14}	2.64×10^{14}	4.90×10^{14}	5.98×10^{12}
5.8	3.3	1.58×10^{14}	2.19×10^{14}	3.21×10^{14}	3.58×10^{12}
4.1	3.3	1.58×10^{14}	2.19×10^{14}	2.08×10^{14}	2.39×10^{12}
3.2	3.3	1.55×10^{14}	2.10×10^{14}	1.70×10^{14}	2.39×10^{12}
1.8	3.3	1.21×10^{14}	1.64×10^{14}	0.94×10^{14}	2.39×10^{12}
1.3	3.3	0.98×10^{14}	1.28×10^{14}	0.75×10^{14}	∿0

14

trace obtained from these tests is shown in Fig. 3. Since the curve is approximately horizontal where it crosses the y-axis (i.e., at cathode potential), the current does appear to be primarily a collected ion current. This test demonstrates that the surfaces collect negligible electron current but does not prove whether or not electrons are being emitted from the surface. It is believed, however, that the surface work functions are sufficiently high to preclude significant electron emission from these surfaces at their prevailing temperatures. Electron production due to photoemission or from ion-induced, secondary emission have also been estimated analytically and found to represent insignificant components of the measured current. On the basis of these considerations currents I_1, I_3, I_4, I_5 and I_6 can be assumed to give the ion current to each corresponding cathode surface. Adding these to the insert ion current obtained in the preceding paragraph one obtains the total ion current to cathode surfaces. The result of this is that in general about 32% of the total emission current (I_E) is due to ions returning to cathode potential surfaces. About 17% of this total emission current is ion current[*] to the insert and the remainder (15%) to the other cathode surfaces. This distribution of currents appears to be valid over the full range of emission current investigated. As the cathode pressure is reduced the cathode tube begins to emit (I_1 in Column 7 of Table I), but the basic distribution of ion and electron currents suggested by this analysis is still considered to be valid (i.e., ~17% of the emission current is actually ion current to the emitting region and ~15% is ion current to other cathode surfaces).

---

[*] The ion current to the insert is ~20% of the total insert current and the total insert current is 85% of the total emission current.
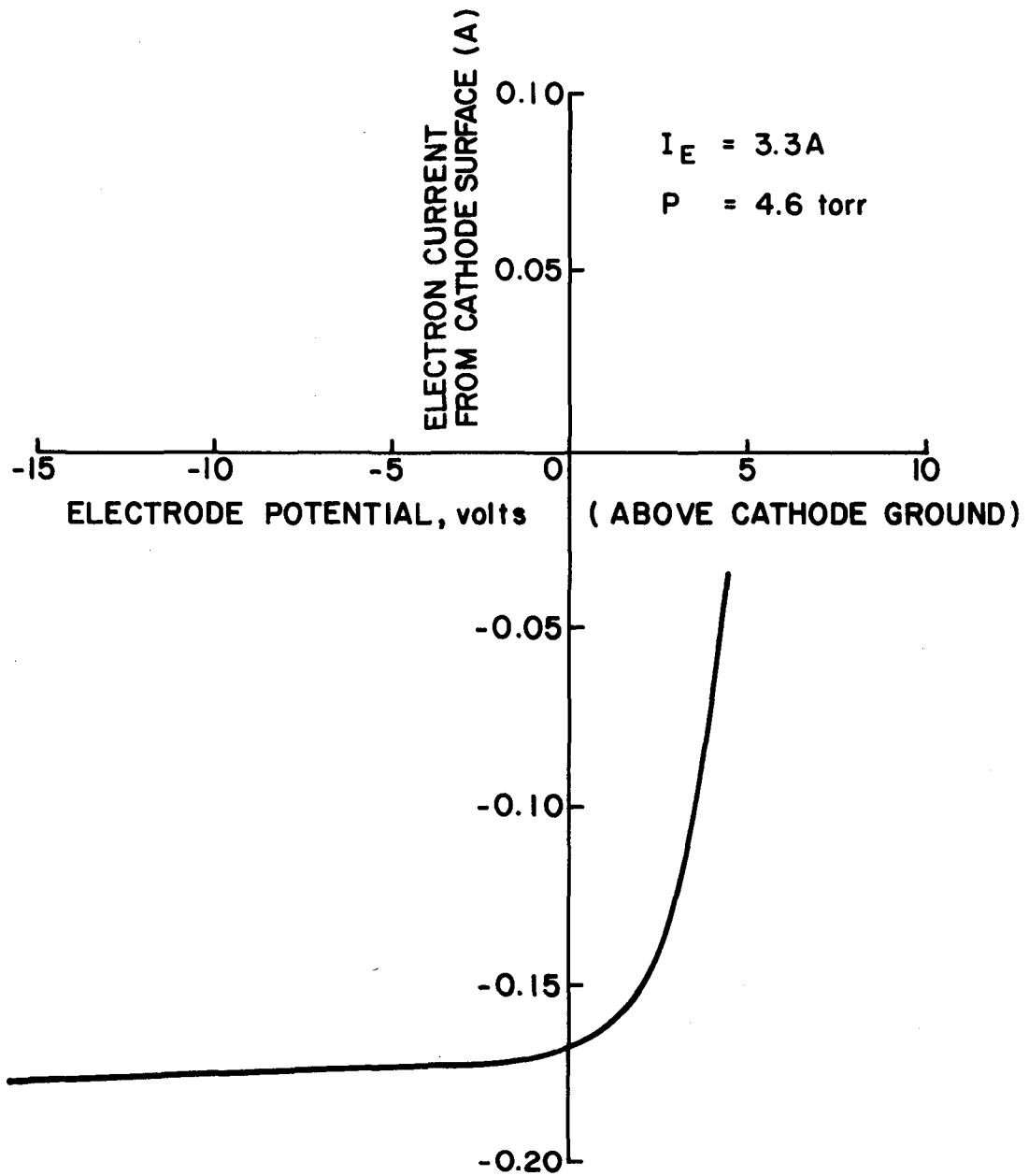
Fig. 3. Typical Current-Voltage Characteristic

Knowing the ion current to each surface makes it possible to estimate the plasma density adjacent to each surface. This is done by using Eq. 1, assuming that the surface is in a region of uniform plasma density and that the ions leave the plasma at the Bohm velocity based on an electron temperature obtained in previous experiments of $\sim$0.8 eV.[3] The calculated plasma densities adjacent to each surface are shown in Table II. The most notable result shown in this table is that the plasma densities adjacent to the insert (n_2) and upstream side of the orifice plate (n_3) are close to each other over the full range of experimental conditions. This suggests that the ionization is, in fact, taking place in a narrow slice bounded by the insert segment and the upstream side of the orifice plate. It also suggests that the plasma density is relatively uniform in that region, and that the energy balance used to estimate the ion current to the insert yields self-consistent results. It should also be noted that the plasma densities shown in Table II for the region adjacent to the insert (n_2) are in reasonable agreement with those found from Langmuir probe measurements made in earlier studies[3] under similar conditions.

An experiment was also conducted using the cathode configuration of Fig. 2 but with the insert moved back $\sim$2 mm from the orifice plate. The plasma densities adjacent to the various cathode surfaces are shown in Table III for both the case where the insert is moved back from the orifice plate and the case where it is in the normal position. A comparison of the results shows that while the plasma density is roughly the same adjacent to both the insert and the orifice plate with the insert in the normal position, this is definitely not the case when the insert is moved upstream. With the insert upstream, the density adjacent to the orifice plate is only about one-third of that in the insert region but it jumps

TABLE III

Effect of Insert Position on Cathode Densities

Insert Position	Cathode Internal Pressure (torr)	Total Emission Current $I_E(A)$	Insert Density $n_1(cm^{-3})$	Density Immediately Upstream of Orifice Plate $n_2(cm^{-3})$	Density within Orifice $n_3(cm^{-3})$	Density Immediately Downstream of Orifice Plate $n_4(cm^{-3})$
Normal	5.8	3.3	1.6×10^{14}	2.2×10^{14}	3.2×10^{14}	3.6×10^{12}
Upstrm 2 mm	5.8	3.3	1.2×10^{14}	0.36×10^{14}	3.9×10^{14}	4.3×10^{12}

TABLE IV

Effect of Point of Electron Collection on Cathode Operating Parameters
(Insert 2 mm Upstream of Orifice Plate)

Anode Surface	Cathode Internal Pressure (torr)	Anode Current $I_A(A)$	Anode Voltage $V_A(V)$	Keeper Current $I_K(A)$	Keeper Voltage $(V_K(V))$	Insert Density $n_1(cm-3)$	Density Immediately Upstream of Orifice Plate $n_2(cm^{-3})$
Normal	4.6	3.0	16.6	0	6.0	1.1×10^{14}	3.1×10^{13}
Downstream Side of Orifice Plate	4.5	3.0	12.3	0	5.5	1.1×10^{14}	3.1×10^{13}
Upstream Side of Orifice Plate	2.6	3.0	9.8	0	~ 0	1.1×10^{14}	--
Normal	2.6	3.0	17.8	0	6.3	1.1×10^{14}	3.1×10^{13}

by an order of magnitude as one proceeds into the orifice. This provides additional support for the assumption that the ion production region is that region circumscribed by the emitting portion of the insert and follows the insert when it is moved upstream. In addition, this suggests that the orifice is also an ion production region since with the insert moved upstream the density decreases in the region between the insert and the orifice plate presumably due to wall losses and then increases again within the orifice.

The effect of internal cathode pressure on the current distribution of the cathode with the insert in its normal position is shown in Fig. 4. In this figure the measured current to the internal surfaces (from Table II) including the orifice bore is plotted as a function of internal cathode pressure for the cathode operating at a constant total emission current of 3.3 A. This figure indicates that at pressures above ∿3 torr essentially all of the electron emission comes from the insert. Recall that according to the proposed model the electron emission current density (j_e) from an emitting surface is proportional to the measured current density (j_{total}) or in this case I_2/A_2. At pressures below ∿3 torr, the insert emission current begins to drop off and the current from the cathode tube (Curve I_1 in Fig. 4) begins to increase. This suggests that the electron emission region, and therefore the ion production region, spreads upstream along the cathode tube as the pressure is decreased below ∿3 torr. This increase in emission area in the upstream direction as pressure is decreased has been seen in earlier experiments and previously reported.[4] The curves in Fig. 4 for measured current to the orifice plate (I_3) and the orifice bore (I_4) are also interesting in that they display different sensitivities to internal pressure. Assuming that there is no electron emission from these surfaces, it was argued earlier that these currents must be purely ion currents and
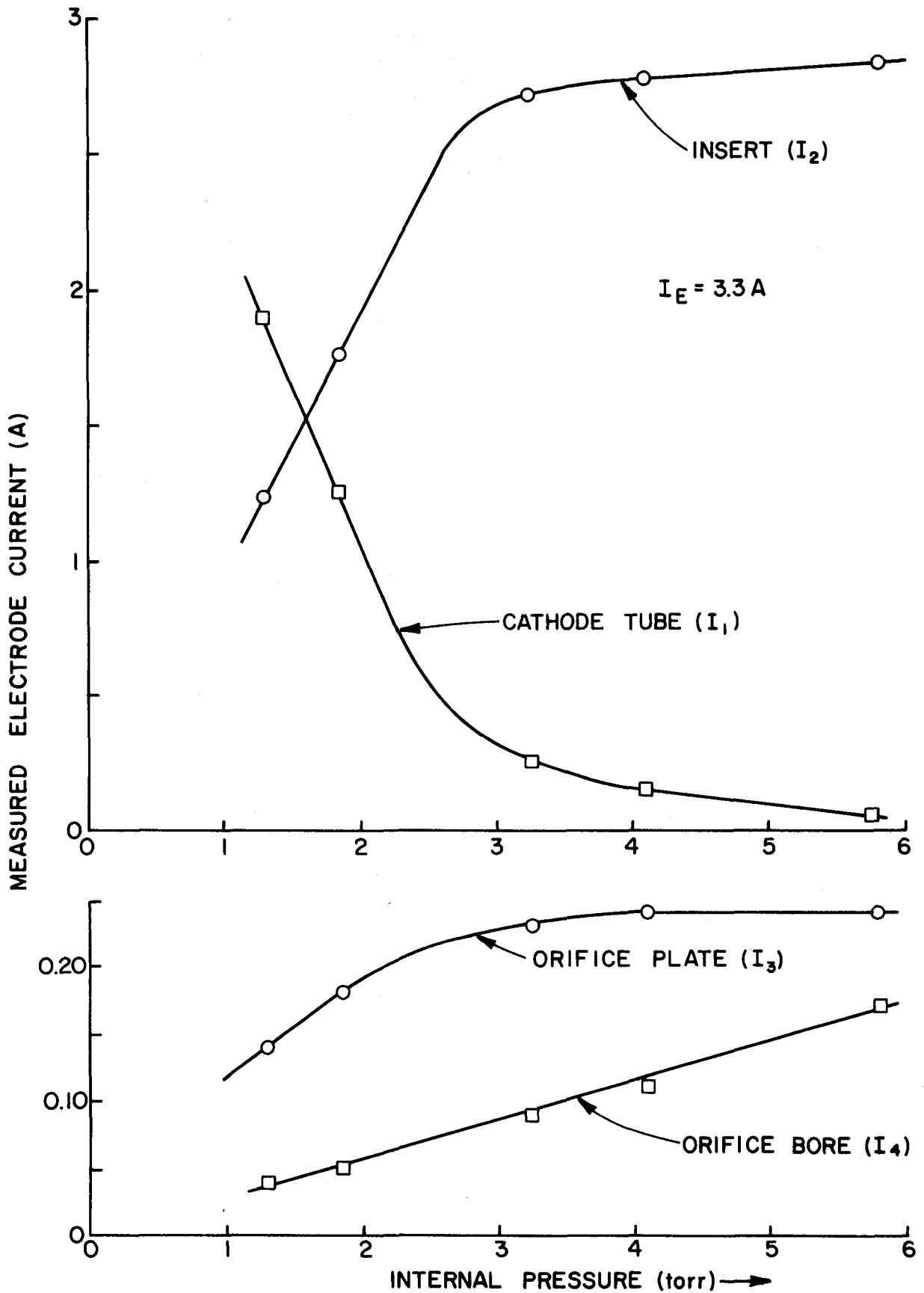
Fig. 4. Effect of Internal Cathode Pressure on Current Distribution

as such are proportional to the plasma density adjacent to the respective surfaces (values of these densities are indicated in columns 4 and 5 of Table II). The plasma density adjacent to the orifice plate, as indicated by Curve I_3 (Fig. 4) follows the same behavior as the insert Curve I_2. It is approximately constant at pressures above ∿3 torr and decreases for pressures below that. The interesting thing, however, is that the ion current to the orifice bore (Curve I_4, Fig. 4), and therefore the plasma density in that region (Column 5 of Table II), are linear functions of pressure. This is a different pressure dependance than that of plasma densities adjacent to the other internal surfaces. This suggests that the orifice plasma is isolated from the internal cathode plasma by either the gas dynamic effect of acceleration through the orifice or by the double-sheath commonly associated with a discharge constriction such as the orifice.[6]

The fact that the orifice plasma appears to be isolated from the internal cathode plasma by some sort of a boundary or sheath was also illustrated by another experiment. Since the surfaces of the cathode were electrically isolated from one another, it was possible to bias each of them sufficiently positive with respect to the insert so they would collect all or a portion of the emission current. Such an experiment was conducted with rather interesting results. The cathode was operated at a total emission current of 3.0 A, without any keeper current and with a mass flow rate of ∿100 mA. The insert just happened to be moved 2 mm upstream of the orifice plate in this test but this is not felt to be significant. The results of collecting the emission current on the downstream side of the orifice plate (Surface 5 on Fig. 2) and on the upstream side of the orifice plate (Surface 3) are shown in rows two and three respectively of Table IV. Row one of this table gives the characteristics of the normal operating mode where the electrons are collected on an anode downstream of the keeper. The

most notable comparisons that can be seen in Table IV are between the potentials of the surface collecting the current (Column 4) and the internal pressures within the cathode (Column 2). Collecting the current at the downstream side of the orifice plate drops the anode voltage from a normal value of 16.6 v to 12.3 v but has only a small effect on the internal pressure. Collecting the emission current at the upstream side of the orifice plate, however, not only drops the anode voltage to 9.8 volts (this should be near the internal plasma potential) but also causes the internal cathode pressure to drop by nearly a factor of two.

The fourth row in Table IV gives the results for the cathode coupled to the normal downstream anode but with a reduced flow so that the pressure is the same as in the case for results in the third row (collection at the upstream side of the orifice plate). Note that the calculated plasma densities adjacent to the insert are not significantly affected by any of these changes. The above results are consistent with earlier experimental results which have suggested that the orifice channel is a region that sustains strong potential gradients possibly in the form of a double sheath at the upstream end. These potential gradients could be responsible for the ion production which results in the high plasma densities in this region and are most certainly an indication of the plasma heating taking place there. This heating and the fact that ions in this region see an electric field driving them upstream may account for the reduction in upstream stagnation pressure which was observed when the heating in the orifice was removed by collecting the emission current at the upstream side of the orifice plate. It is also suggested that since the orifice provides the conduction path between the internal and external plasmas, that the orifice region relies on the potential drop across it to provide the energy for ion

production in the orifice region. When the emission current is collected downstream of the orifice, the resulting increased plasma density in the orifice region is needed to maintain current continuity in the presence of the large change in cross sectional area of the conduction path.

Surface Work Function and the Emission Mechanism

The most basic assumption of the proposed model is that the emission mechanism is that of field-enhanced, thermionic emission (described by Eqs. 6 and 7). The ability to verify this assumption will probably be the major test of the validity of the model. So far the experimental evidence points to field-enhanced, thermionic emission as being the dominant surface phenomenon producing electrons. This evidence was based at least in part on the ability of the Schottky equation (Eqs. 6 and 7) to predict reasonable values for estimates of the surface work function (ϕ_s).[4] Since the model through Eq. 4 provides a means for determing the electron emission portion of the measured insert current, that is the ratio of j_e/j_{total}, it is now possible, knowing the surface temperature, to calculate the surface work function with greater accuracy than was previously possible. Because the body of the cathode was fabricated from quartz and the insert temperatures could be measured using an optical pyrometer, it was decided to conduct an experiment designed specifically to determine the work function of the electron emitting surface. If the emission mechanism is the one proposed, the surface work function which is calculated from the results should agree with accepted values for the materials used.

The experiment consisted of first operating the cathode at a constant internal cathode pressure of ∿5 torr and emission currents ranging from 0.8 to 5.3 A, and then holding the emission current constant while operating the cathode at internal pressures ranging from 1.8 to 9.7 torr. The data

collected during the experiment were the current to each cathode surface, and the surface temperature of the insert segment which was doing most of the emitting. Using these data, the insert surface area, and the plasma properties obtained from previous tests, the surface work function (ϕ_s) of the insert segment was calculated from Eqs. 4, 6, 7, and 8. The results obtained from evaluation of these data are shown in Fig. 5 as the open symbols and dashed line, where the surface work function is plotted as a function of insert segment temperature. It should be noted that, although there were negligible temperature gradients in the axial direction of the rather short ($\sim$2 mm long) insert segment, there were locally hot regions around the circumference which were as much as 56°C hotter than the average temperature used in calculating the work function. Because of these temperature gradients, another experiment was designed in which a smaller portion of the insert would be electrically and thermally isolated to provide data for calculating the work function. A sketch of such an insert with a test "patch" is shown in Fig. 6. The work functions calculated for this "patch" experiment are shown as the solid symbols and solid line in Fig. 5.

The data of Fig. 5 suggest that the results for both the insert segment and the patch are similar and that in both cases the surface work function is a linearly increasing function of the surface temperature. Such a linear relationship between work function and surface temperature is, in fact, expected when the theoretical constant for A_o(120 A/cm^2°k^2) is used to calculate ϕ_s from the Schottky equation. In this case ϕ_s is known as the "true" work function, as opposed to the "Richardson" work function, which is not a function of temperature but relies on an empirically determined value for the constant A_o. The relationship between these two work functions is discussed in Ref. 7. A representative value of the "true" work function,
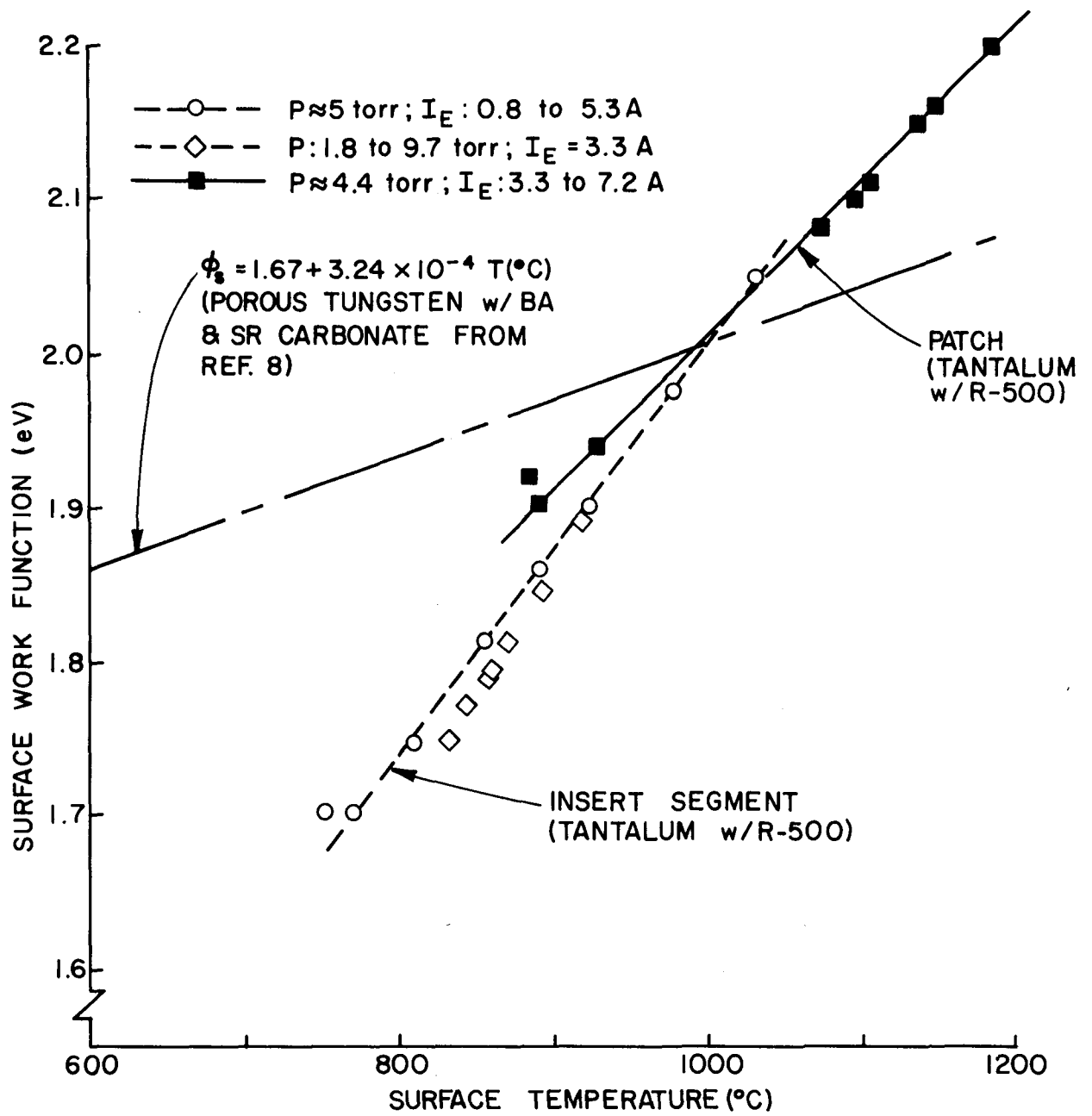
Fig. 5. Effect of Temperature on Insert Work Function

TANTALUM FOIL INSERT

TANTALUM FOIL "PATCH"
(1.25 mm × 1.50 mm)
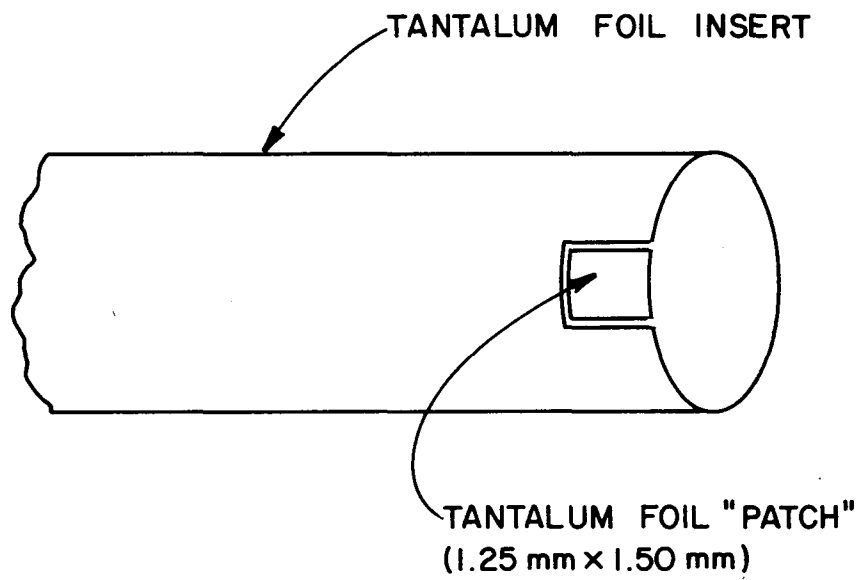
Fig. 6. Insert with Test Patch

ϕ_s, was not available for the tantalum insert coated with R-500 that was used in the experiment. However, Ref. 8 gives the work function of porous tungsten coated with a similar mixture of barium and strontium carbonates, as

$$\phi_s = 1.67 + 3.24 \times 10^{-4} T(°C) \ . \tag{9}$$

This is plotted as the center-dash curve in Fig. 5. When the experimental results in Fig. 5 are compared to the center-dash curve their magnitudes appear to be reasonable (1.7 to 2.2 eV). Also both the experimental results and the center-dash curve display a linear increase with temperature though with different slopes. It might be pointed out that for the operating conditions in these tests the electric field adjacent to the emission surface, as estimated from Eq. 8, is $\sim 3 \times 10^5$ V/cm. This means that when the cathode is operating, the field-enhancement results in an effective work function $\bar{\phi}_e$ which is reduced by ~ 0.2 eV (Eq. 7) from the surface work function ϕ_s shown in Fig. 5.

It should be noted that an incorrect estimate of the emission surface area can cause a change in the slope of the linear work function-temperature plot like the one shown in Figure 5. If the extent of the emission surface area is overestimated then the slope of the work function curve will be increased over what it would be if the true emission area were used for calculating the work function. The difference in slope is given by the expression

$$m_{act} - m_{est} = \frac{k}{e} \ln \left(\frac{A_{est}}{A_{act}} \right) \tag{10}$$

where m_{act} and m_{est} are the actual and estimated slopes of the curves, and A_{act} and A_{est} are the corresponding emission areas. To account for the difference in slope between the solid curve in Fig. 5 for the patch data

and the curve based on Ref. 8 solely on the basis of having overestimated the emission area would imply that the estimated area was 2300 times the actual emission area. Since the patch temperature was quite uniform it is rather unlikely that the emission was coming from such a small area unless the work function was highly nonuniform across the surface. A more likely explanation is that the actual surface work function for tantalum coated with R-500 deviates somewhat from that of porous tungsten coated with barium and strontium carbonates.

Future Work

The results shown in Fig. 5 indicate that the emission process is characterized by a work function that is reasonable because of its magnitude and its linear dependence on temperature. However, it is apparent from the discussion above that the exponential sensitivity of the emission current to the work function makes this evidence insufficient to permit one to determine conclusively whether field-enhanced, thermionic emission is the only emission mechanism acting. Such a judgement could be made, however, if the actual work function were accurately known for the emitting surface. One method of determining this work function would be to make an independent measurement of the work function of the surface without the discharge present. Because of the extreme sensitivity of the surface work function to contamination and operating history, it is considered imperative to make this measurement without having to remove the insert from the cathode. An experiment to perform such an in-situ measurement has been proposed and is currently in progress. The basic features of the apparatus to be used in this test are illustrated schematically in Fig. 7. The cathode would first be operated in a normal manner and the emission current and temperature
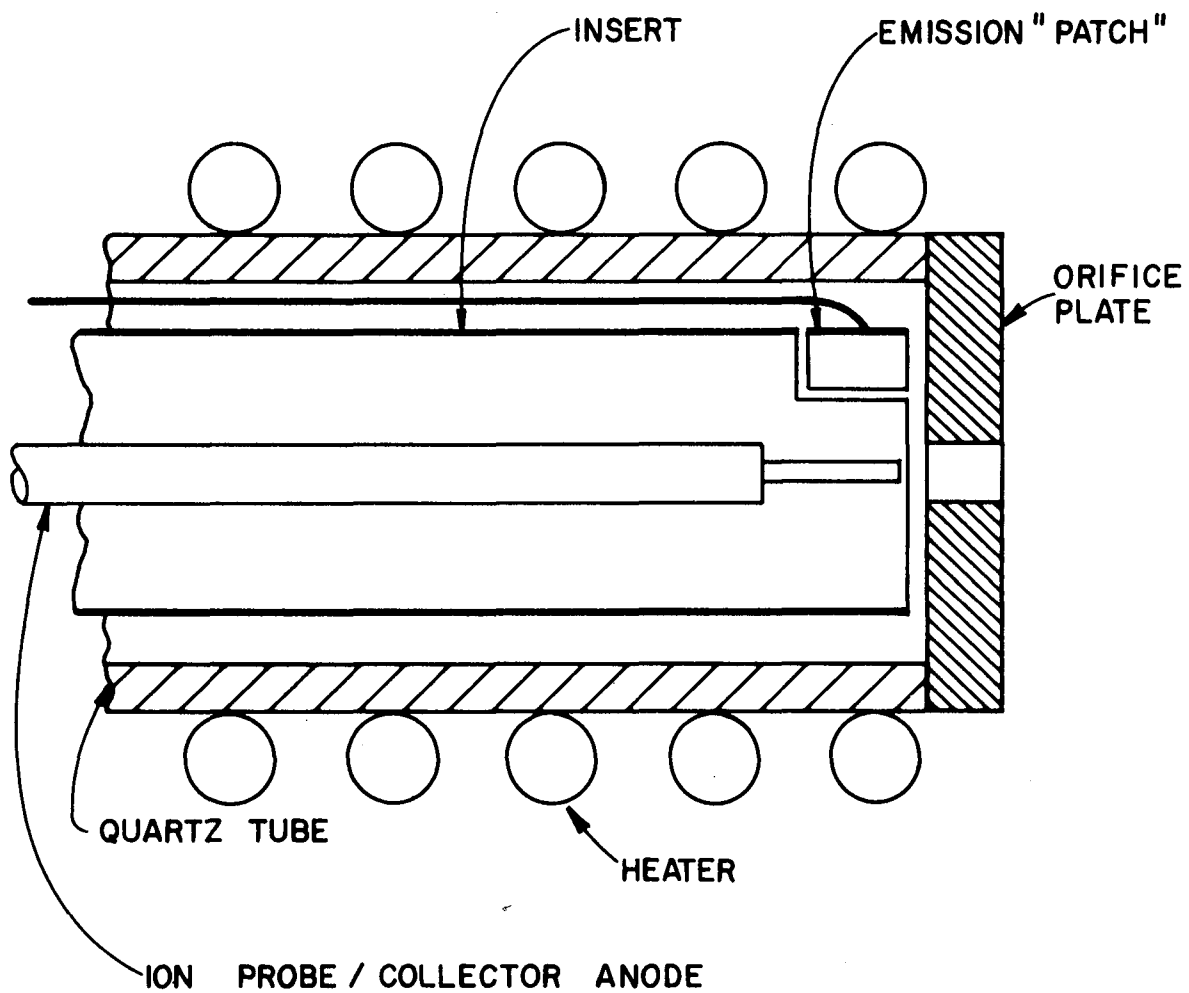
Fig. 7. Apparatus for In-situ Measurement of Insert Work Function

of the insert "patch" would be measured. An ion collecting probe would be used to measure plasma density and electron temperature adjacent to the "patch". The results of this test would be used as input to the field-enhanced, thermionic emission model, and the work function associated with this operating mode would be calculated. Next the discharge and mercury flow would be turned off, and the external heater would be used to heat the insert and "patch" to emission temperatures. The collector anode shown in Fig. 7 would then be biased positively to collect the emission current. The measured patch current and temperature would now be used to calculate a second, independently determined work function for the "Patch". Comparison of the two work functions should provide a conclusive test as to whether or not field-enhanced, thermionic emission is the dominant emission process in the hollow cathode.

As mentioned earlier, the model lacks the ability to explain the location and extent of the emission region or to make a priori predictions of the plasma properties. Additional efforts are planned to model the ion production region in greater detail in order to fill in these gaps. This work will look at modeling the ion production and loss rates within the ion production region using the present model to specify the boundary conditions for the region. It is hoped that this will allow prediction of the plasma properties in this region and provide some insight into a criteria for determining the emission location and extent.

Conclusions

The proposed phenomenological model describing orificed, hollow cathode operation is in good agreement both qualitatively and quantitatively with a number of recent experiments. The model's description of the ion production region for the internal discharge as the region bounded by the

electron emission surface is supported by the experimental results.
Further, the model makes reasonable and self-consistent predictions of
the plasma density in that region. The current to the cathode emission
surface makes up $\sim$ 85% of the total emission current with about 20%
of that being attributable to the ion current to the emission surface.
The remaining 15% of the total emission current is due to ion currents to
various cathode and facility ground surfaces. These surfaces do not
collect a significant electron current, nor do they appear to produce any
appreciable electron emission.

The "true" surface work function of the emission surface calculated
from experimental data using the model shows the expected linear dependence
with temperature and is of a reasonable magnitude. Though this is not
sufficient to prove conclusively that field-enhanced, thermionic emission
is the dominant emission mechanism in this type of cathode, it does tend
to support this assumption. An additional experiment which could possibly
provide such proof is suggested.

The orifice region sustains potential drops of a few volts and appears
to be an ion production region. The plasma density in this region shows a
different sensitivity to internal pressure changes than does the internal
discharge, making it likely that this region is isolated from the internal
discharge by phenomena such as a double-sheath or gas dynamic effects.

Finally, though the proposed model falls short of making a priori
predictions of plasma properties within the cathode, it can predict the
emission surface temperature if the plasma potential, electron temperature,
emission surface area and surface work function are assumed or specified.

HOLLOW CATHODE PLASMA OSCILLATIONS

Dan Siefried

Work directed at refining the Langmuir probe technique used for
making plasma measurements inside the hollow cathode identified plasma
oscillations in the megahertz range that appear to be an inherent feature
of orificed, hollow cathode operation. Initially investigated to de-
termine their effect on Langmuir probe results, these oscillations were
found to be an interesting and possibly important phenomena in their own
right. Although these oscillations were not studied in detail, it was
determined that they are due to some plasma phenomenon occurring in the
orifice or downstream of the orifice and that they are not dependent on
power supply characteristics.

Experimental Results

The quartz test cathode used in the experiments to be discussed below
was similar to the one used in earlier experiments and is shown in Fig. 8.
The cathode was operated in the normal manner while various parameters such
as discharge current, mass flow rate and orifice diameter were varied and
parameters such as anode voltage, keeper voltage and probe floating potential
were displayed on an oscilloscope. The frequency and amplitude of the
observed oscillations were found to be affected to some degree by each of
the parameters that was varied and also by operating mode (spot or plume).
The oscillations varied from very well defined, coherent waveforms at
frequencies around one megahertz to what appeared to be either random noise,
or possibly oscillations at frequencies beyond the range of the oscilloscope
which was being used (∿50 megahertz). These oscillations were not investi-
gated in sufficient detail to define the effects of various parameters on
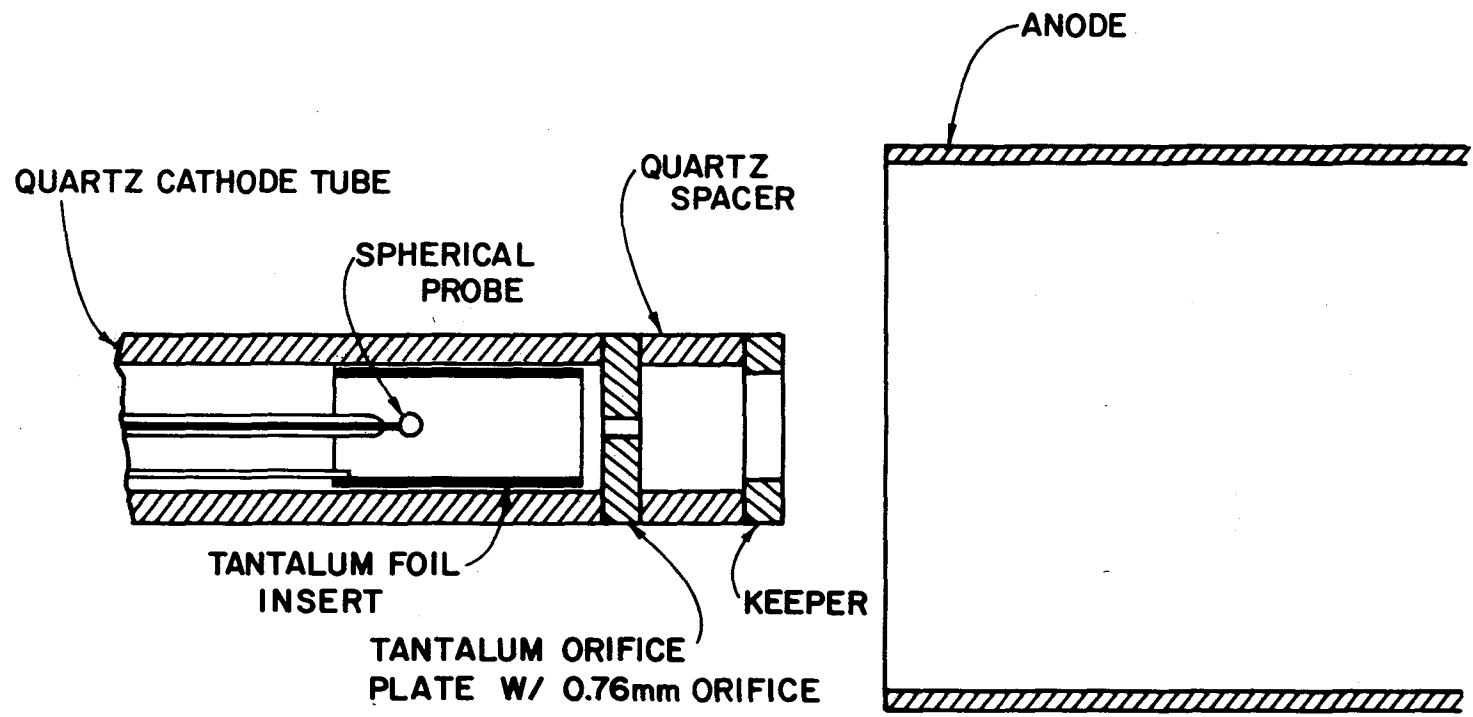
Fig. 8. Quartz Test Cathode

the oscillations, although it was noted that the most well-defined wave-
forms were found when the cathode was operating in the spot mode at currents
just above the transition point between the plume and spot modes. A
photograph of the oscilloscope trace displaying a typical waveform under
these conditions is shown in Fig. 9. This photo was taken for a test
cathode having a 0.76 mm diameter orifice operating at a total emission
current (I_E) of 3.5A, a discharge voltage (V_A) of 16.6v, and a mass flow
rate ($\dot{m}$) of $\sim$100 mA. The oscillations have a frequency of $\sim$0.9 MHz and an
amplitude of $\sim$0.15v. The oscillations in this case were sensed with a 0.8 mm
diameter spherical probe with the probe at floating potential ($\sim$2.5v) and located
$\sim$10 mm upstream of the orifice plate. The oscillations were also present
on the keeper and the anode at the same frequency but with larger amplitudes.
For comparison, Fig. 10 shows the oscillations present in the plume mode
at the same flow rate for a total emission current of 2.3 A and a discharge
voltage of 21.8 v. In this case the waveform is not as well defined and
appears to have a frequency of 0.67 MHz and an amplitude of $\sim$0.06 v (note
that the vertical or voltage scale in this figure is 0.1 v/division as
compared to 0.05 v/division in Fig. 9). The probe voltage fluctuations
at a higher current (I_E = 5.3 A; V_A = 17.5 v; spot mode) are shown in
Fig. 11. Results shown here were typical of higher current conditions
where the coherent oscillations appeared to break down into random noise.
Note that the horizontal, or time scale in this oscillograph is different
than that in the previous ones. However, even when displayed on the same
time scale, that is 0.5 μs/division (the limit for this oscilloscope), no
coherent oscillations could be detected at this higher current condition.

Since the test cathode was made of quartz with a tantalum orifice
plate, it was possible to disconnect the keeper and normal anode and
collect the discharge current at the upstream side of the orifice plate

→| |←—0.5 μs

0.05 v
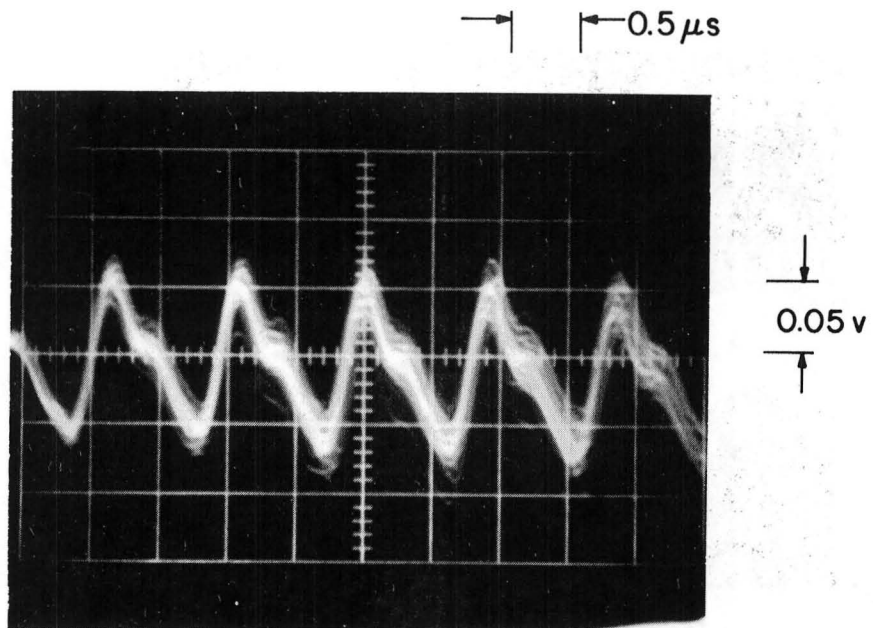
Fig. 9.   Probe Floating Potential Fluctuations
(I$_E$ = 3.5A, V$_A$ = 16.6v, ṁ = 100mA, Spot Mode)

→| |←—0.5 μs

0.l v
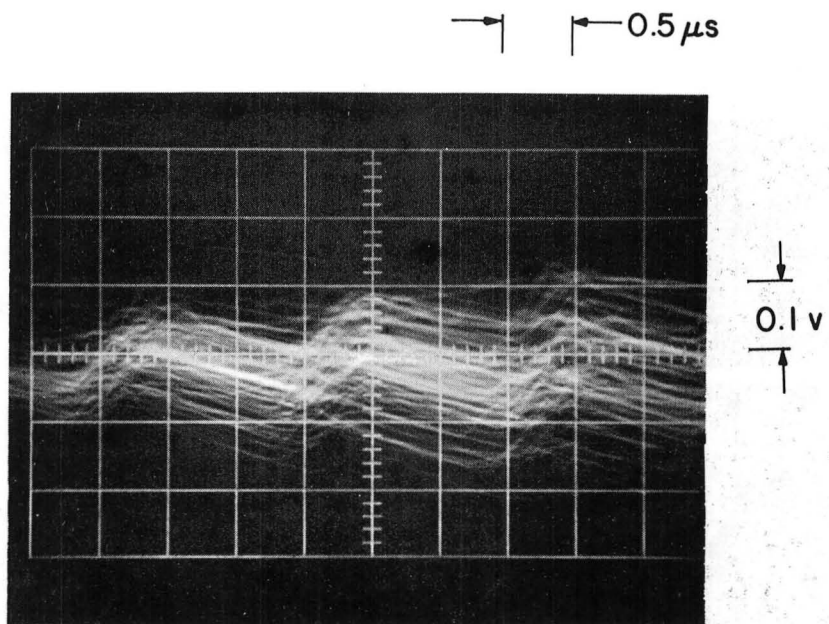
Fig. 10.   Probe Floating Potential Fluctuations
(I$_E$ = 2.3A, V$_A$ = 21.8v, ṁ = 100mA, Plume Mode)
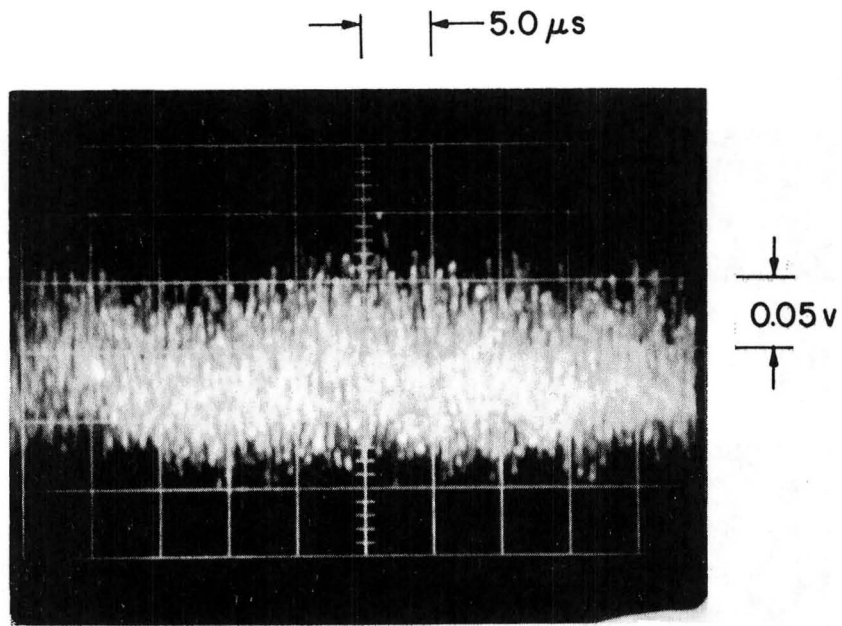
Fig. 11.   Probe Floating Potential Fluctuations
(I_E = 5.3A, V_A = 17.5v, $\dot{m}$ = 100mA, Spot Mode)
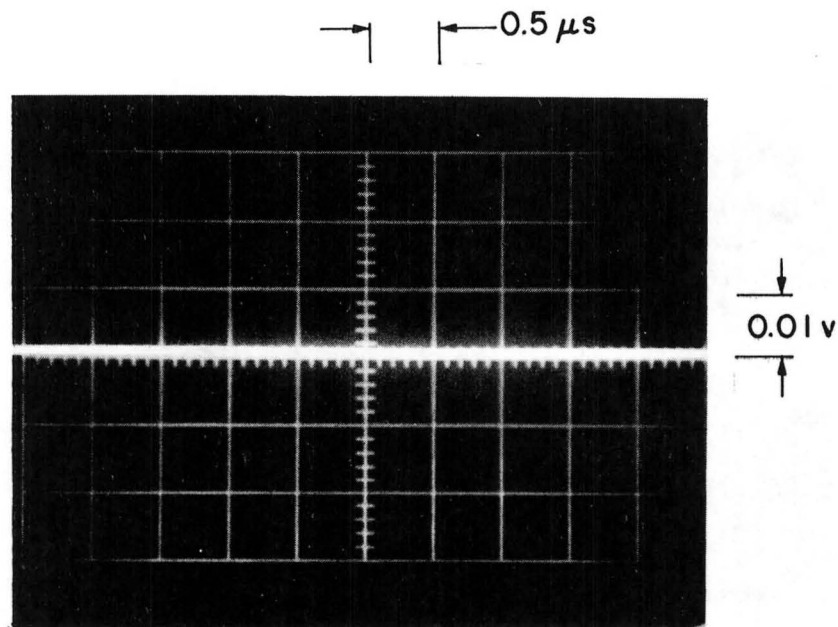
Fig. 12.   Probe Floating Potential-Electron Collection at Orifice Plate
(I_E = 2.3A, V_A = 12.1v, $\dot{m}$ = 100mA, Plume Mode)

by utilizing it as an anode. When this was done it was found that there was no visible discharge present downstream of the orifice. In this configuration the plasma oscillations disappeared completely and the internal discharge was quiescent. This is illustrated graphically by the oscillograph shown in Fig. 12 which shows no A.C. component for the probe floating potential when the oscilloscope was on its most sensitive scale. When the keeper was reconnected and its voltage increased, a portion of the discharge again coupled through the orifice to the keeper and the oscillations reappeared.

Byers,[9] studying the effect of power supply impedance on the SERT II neutralizer, also found coherent oscillations present at similar frequencies. Byers found that the oscillations were influenced by the output impedance of the cathode discharge power supply, depending in particular whether this impedance was capacitive or inductive. To determine if the oscillations observed in the present experiment were either caused or affected by power supply characteristics a test was run in which battery packs were substituted for the regulated power supplies normally used. In this test the cathode was started and operated in the normal manner and the oscillations were displayed on an oscilloscope. Both the keeper supply and the anode supply were then replaced with battery packs set to provide the same steady state operating conditions as those realized with the conventional power supplies. All peripheral supplies (heaters, vaporizer, etc.) were then shut off momentarily. The plasma oscillations were not affected either in amplitude, frequency, or waveform by this use of battery power supplies.

Discussion

These tests indicate that the oscillations are not due to power supply interactions and are apparently being produced either within the orifice

region or downstream of the orifice in the keeper region. One possible
source of oscillations in this frequency range is an ion acoustic wave.
Crawford[6,10] in an investigation of the double sheath which forms at a
discharge constriction has identified oscillations related to standing,
radial, ion acoustic waves. The expression for the fundamental frequency
for this type of phenomenon in a cylindrical geometry is

$$f_0 = (\frac{2.405}{\pi d})(\frac{\gamma k T_e}{m_i})^{\frac{1}{2}} \tag{11}$$

where d is the diameter of the constriction, γ is the adiabatic com-
pression coefficient (either 1, 5/3, or 3 but probably 3 for this case),
k is the Boltzmann constant, T_e is the electron temperature, and m_i is the
ionic mass. For mercury under conditions where $\gamma = 3$ and the electron
temperature is 0.8 eV

$$f_0 = \frac{820}{d} \quad . \tag{12}$$

If such a standing wave is present in the orifice, then for an orifice
diameter of 0.76 mm the fundamental frequency for the oscillation would
be $f_0 = 1.08$ MHz which is in good agreement with the observed frequency.

This still leaves a question regarding the mechanism for exciting
these oscillations. Crawford[6] suggests that the double sheath which he
observed at a plasma discharge constriction may be set into motion, like
a vibrating membrane, by the electrons which are being accelerated through
it. Experiments discussed in the preceding section showed that the
orifice region is probably an ion production region and suggested that it
may indeed be separated from the internal discharge by such a double sheath.
One way of viewing this excitation mechanism is that as the double sheath
is formed electrons are accelerated across the sheath with sufficient
energy to ionize neutrals in the orifice region. This establishes a higher

plasma density downstream of the sheath in the orifice constriction - such potential and plasma density differences between two regions are characteristic of the formation of a double-sheath boundary between two plasmas. The oscillations are then excited as the ions in the orifice region diffuse to the orifice wall and upstream through the sheath, thereby causing the double sheath to collapse or at least for the potential across the sheath to fluctuate. If this is the case, the characteristic time for an ion to escape from the production region should be related to the frequency of the oscillations. Based on the Bohm velocity for an electron temperature of 0.8 eV and using the orifice diameter as a characteristic length, a mean transit time for an ion formed in this region to be lost to the wall or upstream through the sheath can be calculated and is found to be on the order of 1.22 μsec. This would correspond to a frequency of 0.82 MHz which again is in reasonable agreement with the frequency of the observed oscillations. This calculation is presented for its physical descriptiveness and is just a simplification of Eq. 11. Equation 11 is in fact the ion acoustic velocity divided by the characteristic dimension with constants dependent on the geometry and boundary conditions.

Conclusions

Plasma oscillations appear to be an inherent feature of orificed, hollow cathode operation. The oscillations are due to some plasma process taking place either in the orifice region or downstream of this region. The oscillations are not due to power supply interaction with the cathode. The oscillations may be in the form of standing, radial, ion acoustic waves excited by fluctuations in the potential across a double sheath as ions are produced and then lost to the walls in the orifice region.

PROBE MEASUREMENTS INSIDE THE ORIFICED, HOLLOW CATHODE

Dan Siegried

Considerable effort was directed at developing and verifying a probe technique and analysis suitable for determining plasma properties within the orificed, hollow cathode. Previously, measurements[3] have been made within the cathode using a cylindrical Langmuir probe with a very fine 0.076 mm diameter tungsten electrode. This gave reasonably good results in regions where the plasma density was $10^{14}cm^{-3}$ or less. However, in regions where the emission is taking place which are of greatest interest the plasma densities are greater than $10^{14}cm^{-3}$ and the very fine wire probe is found to burn up when biased near plasma potential. In order to alleviate this problem, a new technique using a spherical probe having a larger surface area and an analysis based on the ion saturation region of the probe trace was investigated.

Because barium oxide compounds are used to reduce the surface work function in the cathode, probe contamination was also an important concern. Probe circuitry was developed which incorporated a probe cleaning bias and allowed a rapid sweep of the probe potential. This was used as a tool to examine the effects of contamination on the probe results. The effect of plasma oscillations on the probe results was also investigated.

Spherical Probe Design

A number of probe designs were tried with varying degrees of success before settling on the one shown in Fig. 13. In this design, the probe electrode consists of a $\sim$0.8 mm diameter sphere formed by melting the end of a 0.25 mm diameter tungsten wire in a D.C. helium arc. The 2 mm diameter quartz insulator is drawn down to a diameter of $\sim$0.4 mm over a
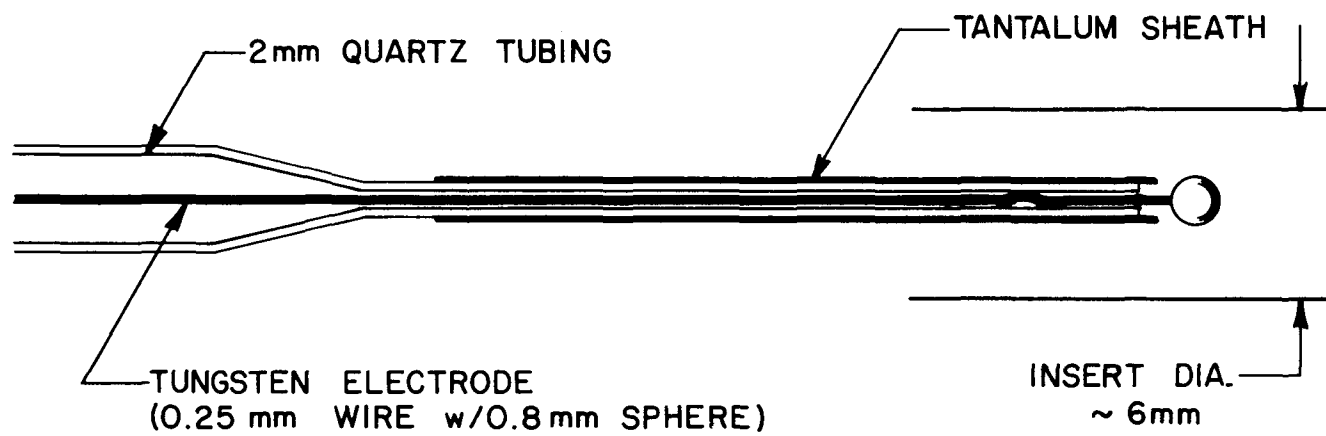
Fig. 13. Spherical Probe Design

length of about 2 cm to minimize its perturbing effect on the plasma.

The end of the insulator is wrapped with a couple of layers of 0.025 mm

tantalum foil. This acts as both a thermal shield and a sputter shield

for the end of the insulator. The wire is kinked just behind the sphere

to give a tight fit in the insulator. This helps to minimize the change

in probe surface area as the probe lead heats up and elongates during

probe operation. When used for making measurements inside of the hollow

cathode, the probe is inserted through a feedthrough on the upstream end

of the cathode mounting fixture in such a way that it can be moved to

various positions along the axis of the cathode. Figure 13 is approximately

to scale and shows the insert diameter in correct proportion to the probe

dimensions.

Data Analysis

Earlier probe measurements made inside the hollow cathode required

biasing the probe to potentials above the plasma potential to obtain a

probe trace such as the one shown in Fig. 14. As mentioned in the intro-

duction, biasing the probe to plasma potential in regions where the plasma

density is very high causes the probe to burn up. The large surface area

of the spherical probe (Fig. 13) however makes it sensitive to the ion

saturation current over the wide range of plasma densities found inside

the cathode. It also provides sufficient information to facilitate

determination of the plasma properties by biasing the probe to the floating

potential (see detail of Fig. 14). Operation at or below floating potential

has the additional advantage of causing less of a perturbation to the plasma

than does the large electron current drawn to a probe at plasma potential.

The use of the ion saturation region of the probe current-voltage character-

istic requires a different method of analysis than does the usual Langmuir
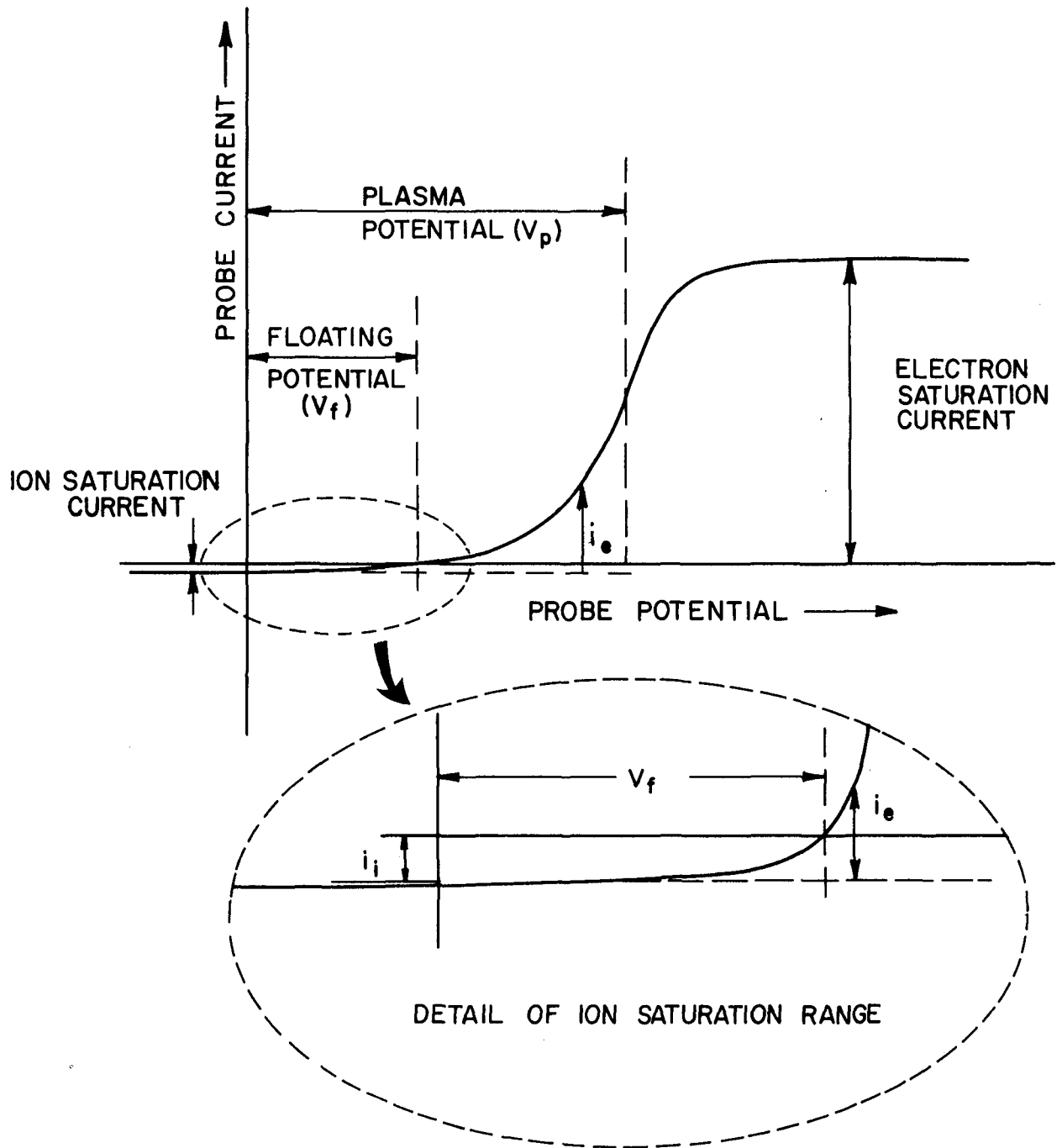
Fig. 14. Typical Probe Trace

probe trace. A method for performing this analysis will be presented, but first it will be useful to discuss some considerations which affect the type of analysis used.

In the past, characteristics taken from probes inside of the hollow cathode have been analyzed based on Langmuir's theory. This analysis applies in the limit where the sheath is collisionless and is thin with respect to probe size. This implies a low pressure, slightly ionized plasma. The hollow cathode plasma, however, is a relatively high pressure (a few torr) plasma with a high plasma density (10^{11} to 10^{15} cm^{-3}). Even though the pressure is high, it has been assumed in the past that because of the very thin Debye length (due to the high plasma density), the normal analysis could be applied with reasonable results. It still appears that this is the case, based on the argument contained in the following paragraphs.

The conditions found in the hollow cathode are such that, although the sheath is thin compared to the probe dimensions, the high neutral density within the cathode results in particle mean free paths which are of the same order as the probe dimensions. This usually causes a presheath to be established between the bulk plasma and the sheath itself in which particles approaching the probe undergo numerous collisions. Significant gradients in the plasma density and potential would normally be expected in the presheath as a consequence of these collisions. When the presheath is present, the conventional Langmuir analysis is usually inaccurate in that it significantly underestimates both the plasma potential and the plasma density of the undisturbed bulk plasma. A survey of literature has shown that there are a number of theories[11,12] which are available for analyzing the probe data in a situation where the sheath is thin and the high neutral density causes a significant presheath. In the case of the hollow cathode,

however, the region surrounding the probe is also one in which the ion production rate is large compared to the rate of ion loss to the probe. Further, the probing technique being proposed here involves the use of only the ion saturation portion of the characteristic probe curve so that large electron currents are not drawn to the probe. Under these conditions, it is believed that the presheath plasma gradients discussed above cannot be established.

Under typical hollow cathode operating conditions it is estimated that the production rate of ions in a volume of the order of the presheath volume is considerably greater than the loss rate of ions to the probe. Where this is the case it is considered justifiable to assume that no significant plasma gradients can be sustained and the conventional thin sheath analysis can be applied. This is almost certainly the situation in the high plasma density (10^{13} to 10^{15} cm^{-3}) region of the cathode where electron emission and ion production are concentrated. Upstream of this region where more moderate (10^{11} to 10^{13} cm^{-3}) plasma densities are expected some intermediate situation probably occurs in which the ion production rate is not great enough to compensate for the plasma gradients set up as ions diffuse to the probe. However, in order to standardize and simplify the analysis, and because the method of approach in the intermediate situation is uncertain, it is proposed that all of the probe results obtained inside of the hollow cathode be analyzed using the relatively simple, thin sheath, collisionless type of analysis.

Given the ion saturation portion of the probe characteristic shown in the detail of Fig. 14, the analysis for the thin sheath probe in an un-preturbed plasma (i.e. no presheath) is quite simple. First, the electron temperature is determined in the standard manner from the exponential portion of the trace. This is done by making a semilog plot of the electron current,

i_e (shown in the detail of Fig. 14) above the extrapolated ion saturation current, against probe potential. The electron temperature is then proportional to the inverse slope of this line. The plasma density is determined from the ion saturation current (i_i) based on the assumption that the ions enter the sheath with the Bohm velocity. This can be expressed as

$$n_e = \frac{i_i}{\alpha A_p e v_B} = \frac{i_i}{\alpha A_p e \left[\dfrac{kT_e}{m_i}\right]^{\frac{1}{2}}} \tag{13}$$

where A_p is the probe surface area, e is the electronic charge, k is Boltzmann's constant, T_e the electron temperature, and m_i is the ion mass. The parameter α is dependent on the ratio of ion temperature to electron temperature and the size of the probe in relation to the extent of the plasma but usually has a value of ~ 0.6.[13] The plasma potential can be estimated from the floating potential based on the condition that the ion and electron currents to the probe must be equal when the probe is floating. This leads to the following expression for the plasma potential:[13]

$$V_p = V_f - \left[\frac{kT_e}{e}\right] \ell n \left[4 \alpha \left(\frac{\pi m_e}{8 m_i}\right)^{\frac{1}{2}} \right] \tag{14}$$

where V_f is the floating potential, m_e the electron mass, and the rest of the symbols are as previously defined.

Probe Contamination

A common problem with probe traces taken in an oxide cathode environment is that the probe will be contaminated by the low work function compounds.[14] This can cause two problems: 1) the formation of resistive oxide coatings, and 2) a reduction in the probe work function. The resistive coatings cause a change in the shape of the characteristic, and thereby, give a false

indication of the velocity distribution of the electrons in the plasma. The probe work function affects the position of the probe characteristic with respect to the reference potential, and can therefore affect the value determined for the plasma potential. This comes about because a probe characteristic must be recorded with reference to some other electrode exposed to the plasma, and the work function acts essentially as a contact potential between the electrode and the plasma. Ideally the reference electrode would have the same work function as the probe. However, if this is not the case then the probe characteristic will undergo a parallel shift along the voltage axis depending on the difference in work functions between the probe and the reference electrode. Generally, this parallel shift is small compared to the plasma potential and is of little consequence.

A more important problem occurs if the probe work function changes during the period while the trace is being taken. This will result in a distortion of the shape of the probe characteristic again leading to false indications of the electron velocity distribution. These problems are generally addressed by taking precautions to maintain the probe in a clean condition and then recording the probe trace rapidly enough so that the probe surface conditions do not vary significantly. In the present case, this was accomplished by designing and building probe circuitry that maintains the probe at a bias potential sufficient to clean the probe and then allows one to sweep the probe potential rapidly to obtain the probe characteristic. The circuitry used to do this is described in Appendix A. This probe circuitry has proven to be a valuable tool for producing clean, consistent probe traces and for investigating the effects of probe contamination.

Using the probe circuitry described above, it was determined that probe contamination probably had been affecting probe traces taken inside of the cathode. Numerous probe traces were recorded with sweep times of ∿1 sec. (near the response limit of the recorder) while various cleaning biases were applied to the probe. The most effective cleaning was obtained by maintaining the probe about a hundred volts negative of cathode potential when a trace was not being recorded. This assured ion energies sufficient to sputter clean the probe surface. This was found to be preferable to electron heating of the probe to incandescence which was found to alter plasma conditions significantly and is generally not effective in removing resistive oxide coatings because of their very high evaporation temperatures. The effect of contamination on the probe was detected by varying the sweep time and also by varying the time delay between switching off the cleaning bias and starting the trace sweep. If the probe trace was swept in a few seconds immediately after turning off the probe cleaning circuit the traces were quite repeatable. However, if the trace sweep was taken slowly (5-10 seconds) or if the sweep was delayed for times on the order of 5-10 seconds, the floating potential of the trace would shift and the shape of the trace would begin to change. This suggested that in the cathode environment the time constant for probe contamination is on the order of 10 seconds and that the probe will probably not be significantly contaminated if the trace is swept within a few seconds immediately after the cleaning circuit is turned off.

At this point it was concluded that by using the above technique the probe should be substantially free of contamination. However, the probe traces that were being recorded indicated electron energy distributions that appeared to be non-Maxwellian at least in the lower energies (i.e.,

near plasma potential). As mentioned earlier, one possible cause for this is a change in probe work function as the trace is swept. If some type of contamination affecting the work function were still present, then a distorted probe trace would be obtained as the probe was heated causing the contaminants to evaporate during the trace sweep. To check whether or not this was occurring, it was considered desirable to run an experiment in which probe traces obtained at increasingly fast sweep speeds were compared. It was decided that the sweep speed should be increased up to the point where no significant probe heating could be taking place. Probe traces obtained more rapidly than ∿1 second could not be obtained using the x-y recorder, so the traces were taken using a storage oscillo-scope. It was found that no difference in the probe traces could be de-tected for sweep times ranging from a few seconds down to 2 milliseconds (the response limit of the differential amplifier used for measuring the probe current). Probe temperature changes were estimated based on calcula-tions of the thermal response of the probe. Under the conditions of the experiment, it was estimated that the probe temperature increase was a maximum of ∿20°C at 1 second and only a few tenths of a degree for a millisecond sweep time. This indicates that under the proposed probing technique the probe is probably in a clean condition and remains in that condition without significant work function changes during the few seconds required for recording the trace. The indicated non-Maxwellian nature of the electron energy distribution is apparently not attributable to con-tamination effects.

Plasma Oscillations

As discussed in the preceding section of this report, plasma oscillations in the megahertz range are an inherent feature of orificed,

hollow cathode operation. A question was raised as to whether or not these oscillations could be causing the indication of a non-Maxwellian electron distribution. In order to examine this question, an analysis was undertaken which looked at a Taylor series expansion of the electron current collected by a probe under the influence of a sinusoidally varying voltage. This analysis showed that, if the electron population is truly Maxwellian, the probe traces will have the same characteristic shape and indicate the same electron temperature regardless of whether or not oscillations are present. However, the oscillations will cause the electron density indicated by the probe trace to be greater than the actual density by a factor of

$$\frac{n_{ind}}{n_{act}} \simeq \left[1 + \frac{V_0^2}{4} \left(\frac{e}{kT_e}\right)^2 \right] \tag{15}$$

where V_0 is the amplitude of the plasma oscillation. Under prevailing conditions in the cathode, however, this effect results in a density variation of only a few percent. The analysis suggests that either the plasma electron population is truly non-Maxwellian or that there is another cause for the non-Maxwellian probe traces. The actual oscillations observed in cathodes have been found to be more saw tooth shaped than sinusoidal, but the basic results of this analysis are probably not changed significantly by this fact.

Additional Considerations

A few additional comments are in order regarding the non-Maxwellian nature of the probe traces. For most regions of the cathode the collection of the energetic electrons, that is the portion of the electron population collected at probe potentials between cathode potential and floating

potential, does in fact follow to a reasonable extent an exponential or Maxwellian pattern. It is only at lower electron energies, that is for probe potentials between floating potential and plasma potential that the electron distribution appears to be non-Maxwellian. Collisional effects[11, 12] are known to distort the exponential nature of the probe traces at these lower energies, and this was in fact the impetus for examining the collisional effects that were discussed in the section on probe analysis. However, even when collisional effects are present the electron retarding region near ion saturation is expected to show a Maxwellian behavior[11, 12] and it is this region which is used for determining the electron temperature. This suggests that the proposed analysis using the exponential portion of the probe trace found at potentials below the floating potential where probe perturbation effects are smallest is probably justified and gives the best estimate for the electron temperature. However, this statement should be qualified by acknowledging what it implies physically. The electrons being collected at probe potentials near cathode potential make up only a small fraction of the total electron population. Moreover, if the cathode model proposed in the preceding section is correct, then the electrons produced by acceleration from the emission surface into the plasma would be expected to form a reasonably mono-energetic population with an energy in the range that would be detected by a probe near cathode potential. This mono-energetic population is estimated to be as much as a few percent of the total electron population, so that based on the present physical under-standing of the cathode, one would predict that the probe trace, rather than being Maxwellian near cathode potential, would be non-Maxwellian probably showing a Maxwellian plus mono-energetic type of behavior. However, there has been no definite evidence that this is the case. At this point, it

appears that the best that can be done is to determine the electron temperature based on the energetic electrons collected at potentials below floating potential, and to assume that the bulk of the electron population is in fact Maxwellian at that temperature.

Conclusions

A spherical probe design suitable for making measurements inside the hollow cathode has been presented. The proposed method of analyzing the probe characteristics is shown to be reasonable for the plasma conditions prevailing within the cathode. Probe circuitry and operating procedure are presented which are capable of maintaining the probe in a clean condition between traces and of minimizing the effect of contamination during the recording of a trace. Plasma oscillations present during cathode operation do not have any substantial effect on the electron temperature or plasma density indicated by the probe characteristic.

SPUTTERING RATES OF DISCHARGE CHAMBER MATERIALS

Susumu Masaki

The lifetimes of discharge chamber components are frequently determined by the erosion rates of those components. This erosion is caused by discharge chamber ions (primarily doubly-charged ones) which strike these surfaces and sputter material away. It has been observed that impurity atoms present in the discharge chamber and on discharge chamber surfaces can affect the erosion rates of these components. Nitrogen for example has been shown to reduce sputtering rates of discharge chamber materials greatly even when it is present at very small partial pressures.[15] It is considered likely that even the mercury propellant may alter the erosion rate of a surface from that which might be expected for the case of doubly-charged mercury ions bombarding a clean surface. The measurement of sputter erosion rates has become a matter of considerable interest for these reasons.

Sputtering rates can be determined in a discharge chamber environment by actually operating a discharge chamber for a known period of time, measuring the depth of sputter erosion and then calculating the erosion rate. In order to obtain accurate values however very long test times are required. In order to facilitate shorter tests, other less direct methods have been pursued. One of these methods involves installing multilayer erosion test patches.[16] These patches are made by alternating very thin layers (several hundred angstroms thick) of the material being tested with copper layers of similar thickness. By counting the number of layers of known thickness that are eroded during a few hours of testing the erosion rate can be determined. A question can however be raised about the validity of such a test, namely; can the erosion rates of copper and the test

material in the layered configuration be assumed to be the same as those determined from measurements on pure copper and pure test metal? If this can be assumed then the test can be used, but if the presence of the copper induces an effect such as coning[17] then the results may not be accurate.

In order to determine the sputtering yields of various thruster materials at the ion energies observed in discharge chamber plasmas, and to investigate the effects of such impurities as copper and nitrogen on these erosion rates the tests described in the following paragraphs were conducted.

Apparatus and Procedure

These tests were conducted in an 18 in. dia. bell jar facility. The ion source used was a 15 cm dia. multipole design with its grid masked down to a 10 cm dia. This source produced current density profiles like those shown in Figure 15. Test samples to be sputter eroded in the beam were placed 6 cm downstream of the grids within the central 3 cm radius circle where the current density was very uniform. The source used either argon or mercury working fluids and the argon or mercury pressures were typically $\sim 5 \times 10^{-4}$ or 3×10^{-5} torr respectively during operation. Figure 16 shows the ion source with the test specimens. The specimens consisted of a flat glass substrate onto which a uniform layer of test material several thousand angstroms thick had been sputter deposited. These specimens were fabricated locally and considerable care was exercised to insure that they were kept clean. In order to minimize oxidation they were kept under vacuum except when they were being transferred between vacuum facilities. After fabrication the sputter coated substrate was partically covered by two ~ 1 mm thick graphite shields that had been undercut in the manner suggested in Figure 16. As a test specimen was exposed to the ion beam, material was

Fig. 15. Current Density Profile

MULTIPOLE ION
SOURCE

10cm DIA. BEAM

MOVABLE BEAM
SHUTTER & CURRENT
DENSITY SENSOR

3 cm

3 cm

TEST SAMPLE

SPUTTERED
TEST METAL
LAYER

GRAPHITE
SHIELD
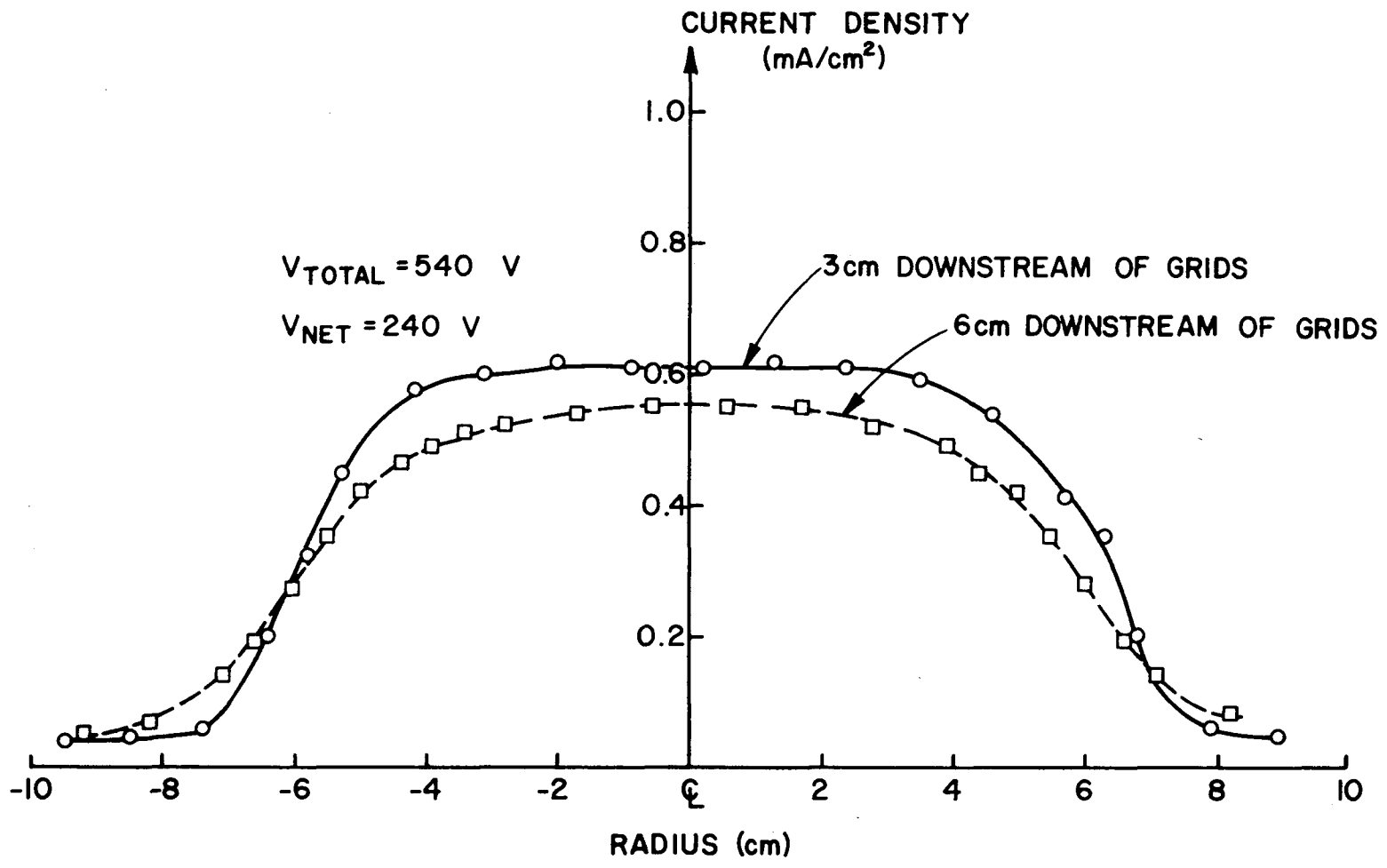
TEST SAMPLE
DETAIL

GLASS
SUBSTRATE
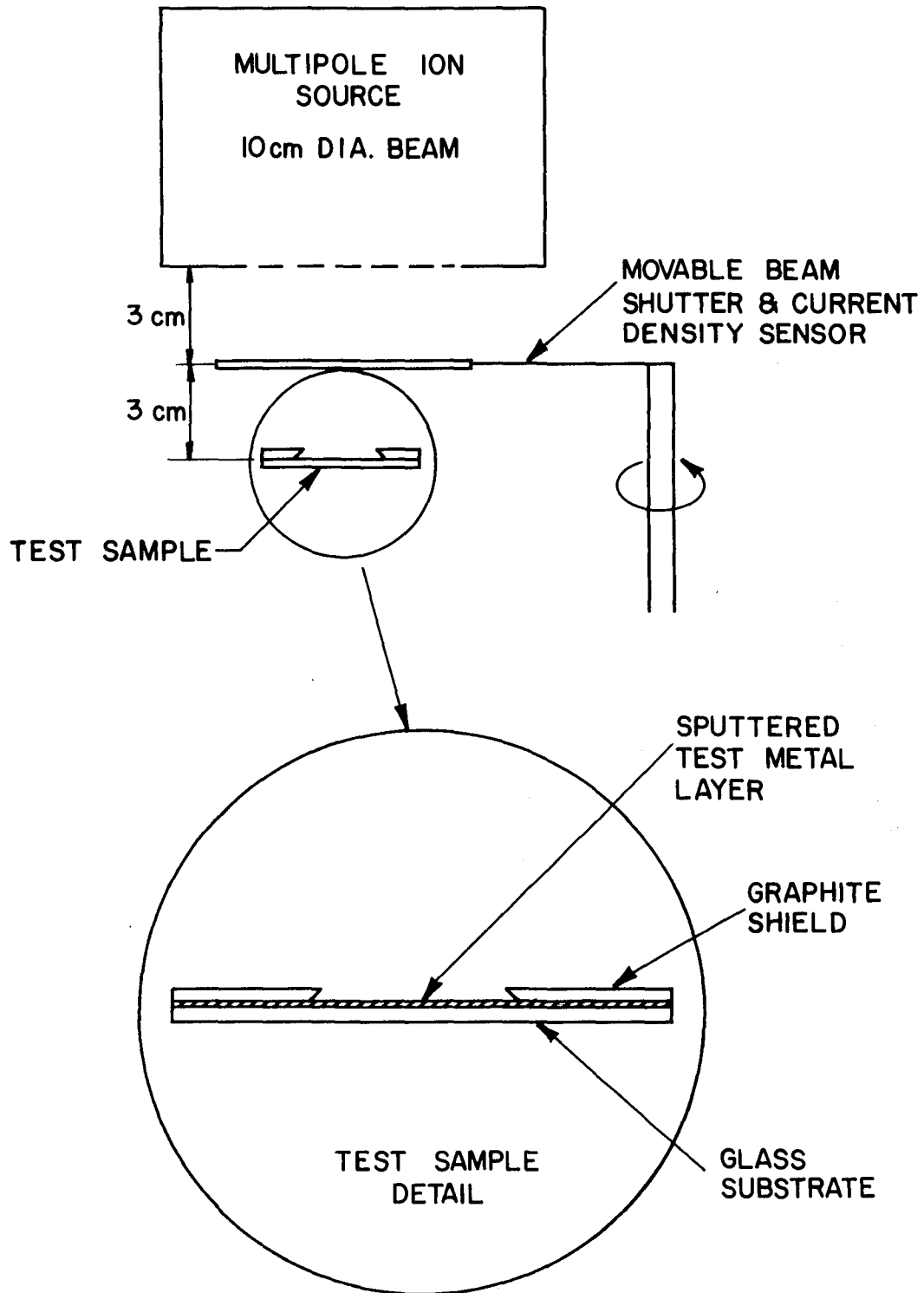
Fig. 16.   Sputter Erosion Test Apparatus

protected where it was covered by the graphite shield and eroded where it was not. As the figure suggests all test samples were exposed to normal incidence ion beams. This resulted in a gradual step having a height which could be measured using an optical interferometer (Angstrometer) after exposure to the beam had been terminated. Test specimens were 1 cm by 4 cm and five specimens could be fitted into the uniform current density portion of the beam so they could be exposed simultaneously. Several kinds of glass substrates ranging from optical flats to photographic plate glass were tried during the course of the tests and photographic plate glass was found to be sufficiently flat so non-uniformities in the glass did not cause errors in thickness measurements made with the optical interferometer.

In conducting the test, the test samples were installed in the vacuum facility and the system was pumped down to about 1×10^{-6} torr. The source was started with the shutter shown in Figure 16 covering the samples, and stable source operation at the desired current density and ion energy was established. The shutter was then opened and the test was initiated. Typically the samples were exposed to an ion beam of constant current density and energy for about 100 minutes. During exposure the samples were cooled radiatively and their temperature rose rapidly to a value of 120 to 140°C when they were exposed to the ion beam. Typically their temperature had risen through 90% of the final temperature rise within about 7 minutes after the shutter had been opened. The samples were allowed to cool for several hours after they had been sputtered. They were then removed from the vacuum facility and the height of the steps machined into them at the edges of the graphite shields were measured.

To establish one data point, five separate measurements of the step height were made on each of two separate machined steps. The mean value of

the step height was then computed and this was divided by the test duration to determine the mean erosion rate. Typically the standard deviation associated with these measurements was ± 10% or less. Using this mean erosion rate and the beam ion current density at the location of the test sample, the sputtering yields associated with each test specimen were computed. Because of the low net acceleration voltage and large resultant beam divergence associated with the tests, considerable care had to be exercised to assure that current densities used as input to this computation were correct. This was accomplished by correlating shutter-probe current density measurements with those obtained at the sample location at each ion energy condition. Corrections to the current density to account for fast moving charge-exchange atoms which should also cause sputtering erosion were also incorporated.

The singly-charged ion energies for these tests were determined by the ion source anode-to-ground electrical potential difference. For these tests, values of this potential difference that were twice the anode-to-cathode potential difference observed in thrusters were selected. Under this condition singly-charged ions in the beam of the test set up have an energy equal to the doubly-charged ions that are the dominant cause of sputter erosion in thruster discharge chambers. Doubly-charged ions in the test set up of Figure 16 would have twice this energy and would introduce an error in the sputtering yield results. The discharge voltage was held at the lowest value where a stable discharge would still occur (35v for mercury and 45v for argon) to minimize this error.

In a second series of tests nitrogen was bled into the vacuum facility to increase the pressure by a specified amount after thruster operation had been stabilized. The sputtering of each test sample in this environment was measured using the same procedure described in the preceding paragraphs.

By varying the change in vacuum chamber pressure caused by the nitrogen (nitrogen partial pressure) the effect of this parameter on the sputtering yields of various thruster materials was investigated. The tests were conducted for one ion energy condition when operating with each working fluid (105 eV for mercury and 115 eV for argon).

In a final series of tests, samples were fabricated using alternated 500 Å layers of copper and molybdenum and of copper and 304 stainless steel. These test patches were exposed to argon ion beams ranging in energy from 75 to 115 eV at various nitrogen partial pressures. Molybdenum/copper layered test samples were also exposed to 105 eV mercury ion beams at various nitrogen partial pressures. After the samples had been sputtered the erosion depth was measured using the aforementioned procedure.

Results

Test results showing the effect of argon ion energy in the range 75 to 135 eV on the sputtering yields of tantalum, molybdenum, 304 stainless steel and copper are given in Figure 17. Figure 18 shows the effect of mercury ion energy on the sputtering yields of the same four materials. The argon ion sputtering yield data of Figure 17 for copper are in reasonably good agreement with those obtained by Wehner,[18] the yields for tantalum are about half of the values measured by Wehner[18] and Stuart and Wehner[19] at 135 eV and are in agreement near 75 eV. For mercury the results of Figure 18 can be compared with sputtering yield data obtained by Wehner[18] and Askerov and Sena.[20] The results of these researchers are in reasonably good agreement with each other while the sputtering yields of Figure 18 are in general higher than theirs. The reasons for these differences are not apparent, but one possible explanation for the higher erosion rates observed
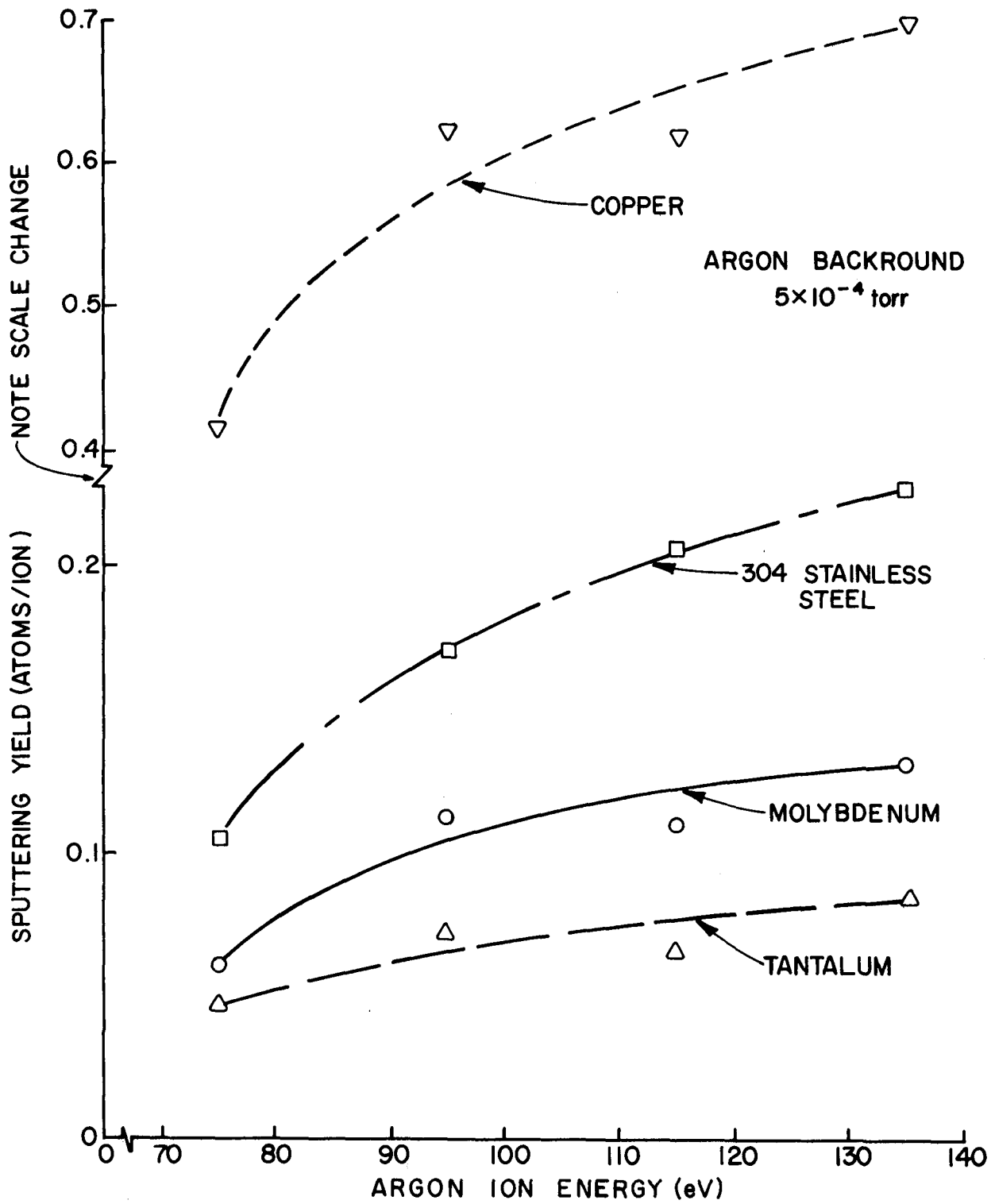
Fig. 17. Argon Ion Sputtering Yields
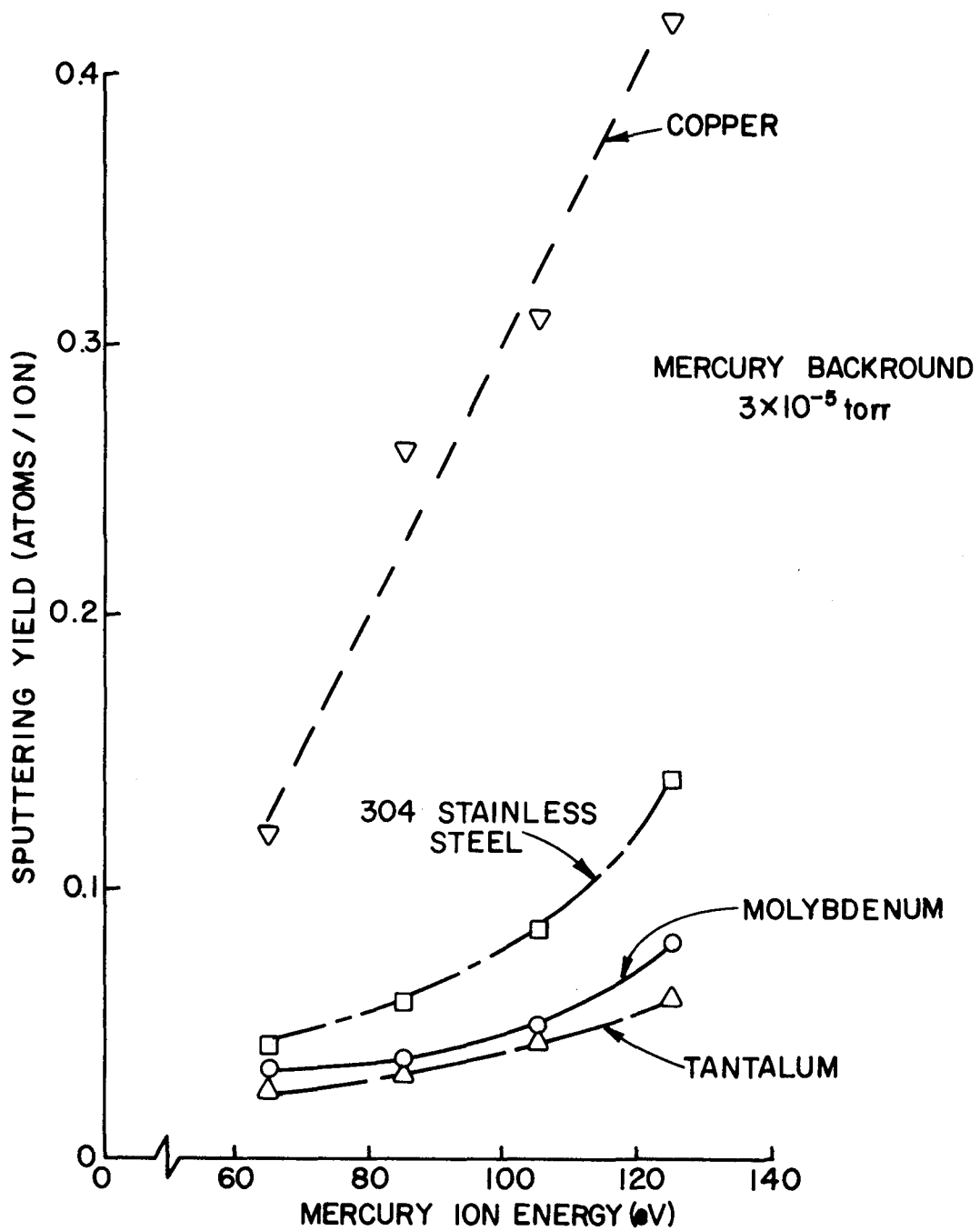
Fig. 18. Mercury Ion Sputtering Yields

in the present mercury experiment is that doubly-charged ion erosion was not negligible as has been assumed. It is interesting to note that the second derivative of sputtering yield with mercury ion energy seems to be positive while for argon it seems to be negative in both the present data and the results of Wehner.[18]

The effect of nitrogen partial pressure on the sputter yields of the various thruster materials being investigated at argon and mercury ion energies of 115 and 105 eV respectively is shown in Figures 19 and 20. Each data point shown is determined by averaging four separate measurements of the erosion depths on each of two separate steps machined by the ion beam. The scatter in these data about the mean values given in Figures 19 and 20 suggest an error of $\pm$ 20% in the data is likely. The data show the expected tendancy for the sputtering yields to drop off substantially as the partial pressure of nitrogen is increased.

The data of Figures 19 and 20 are open to question at the low nitrogen partial pressure levels because the ultimate pressure in the facility, where the sputtering was effected, was $\sim$ 1 X 10^{-6} torr. Other investigators[15,21] have shown using comparative spectroscopic measurements that the onset of the effects of air and nitrogen on sputtering yields occur at pressure at or below 1 X 10^{-6} torr. The data given here suggest that an approximate halving of the sputtering yeilds can be expected for most of these materials as the nitrogen partial pressure is increased from $\lesssim$ 1 X 10^{-6} to a few tens of millitorr.

Erosion rate data obtained from test samples fabricated using alternate layers of copper and molybdenum or 304 stainless steel and copper are shown in Table V. Columns two and three of this table show the nitrogen partial pressures and argon ion energies at which sputtering was effected. The
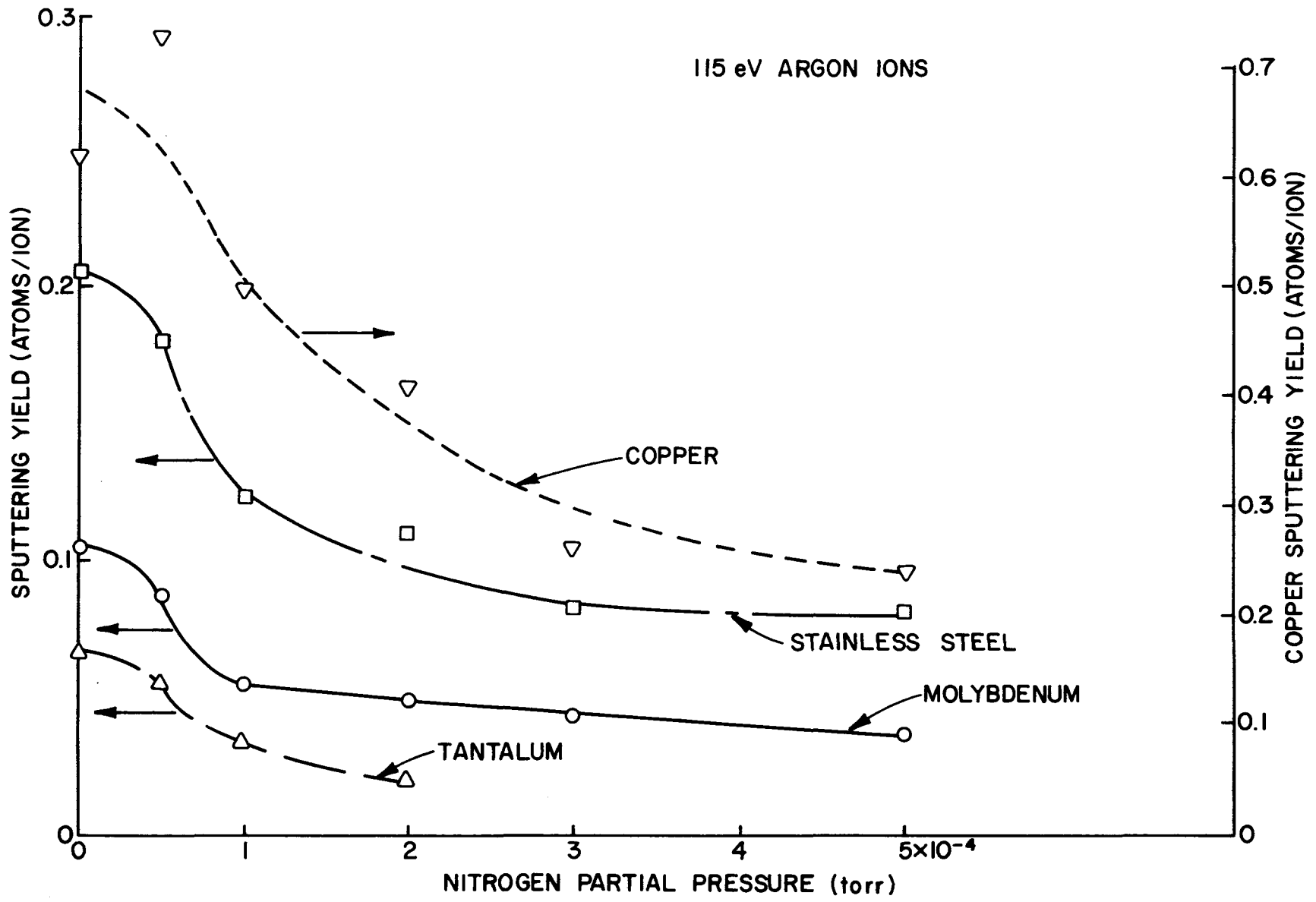
Fig. 19. Effect of Nitrogen on Argon Sputtering Yields
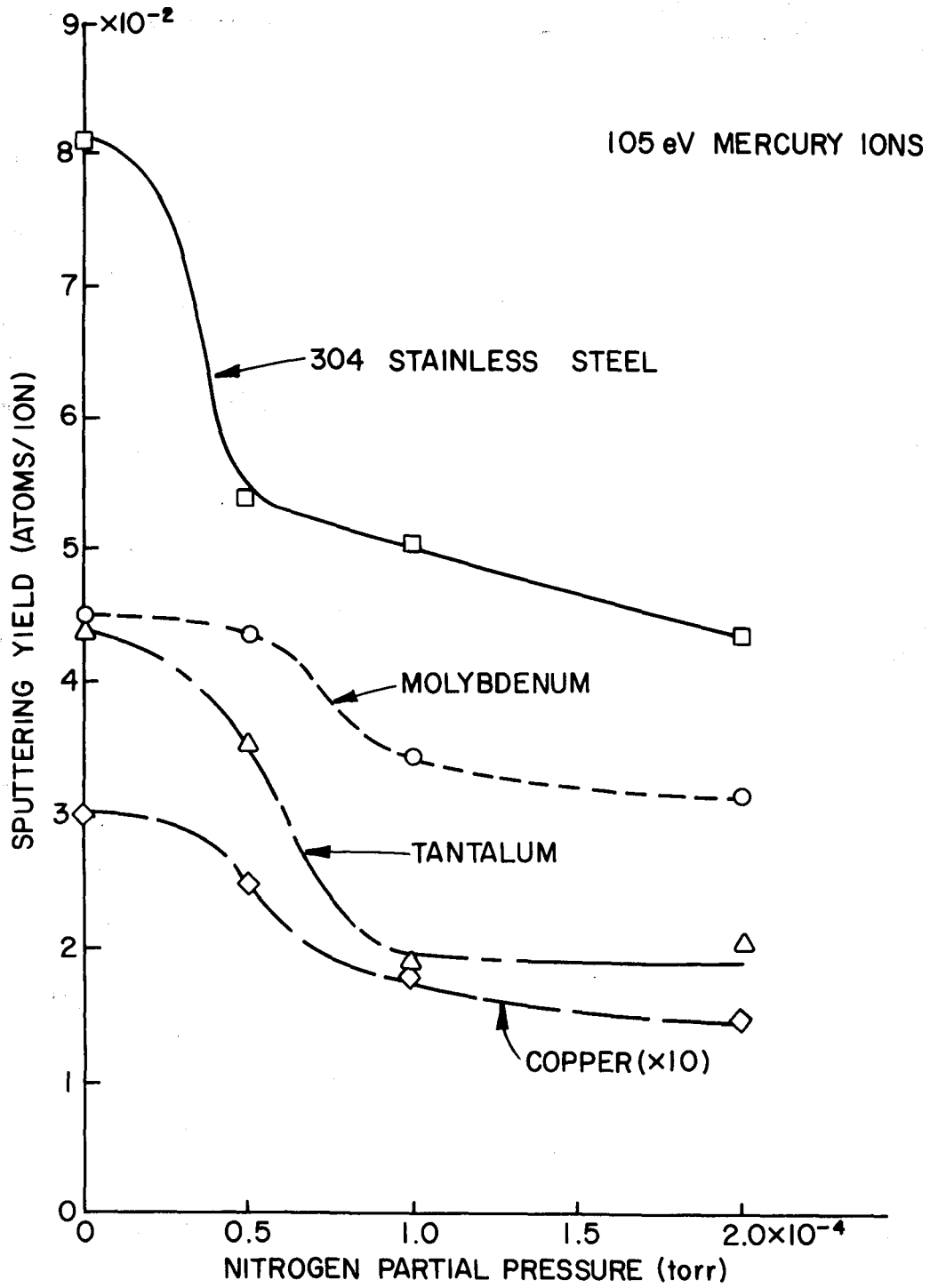
Fig. 20. Effect of Nitrogen on Mercury Ion Sputtering Yields

TABLE V Sputter Erosion Characteristics

of Multilayered Test Samples in an Argon Ion Beam

Test Sample Configuration	Nitrogen Pressure (torr)	Argon Ion Energy (eV)	Erosion Dept (Å)	Test Duration (min)	Calculated Erosion Time (min)
500 Å 304 SS/Copper Layers	$\approx 6 \times 10^{-6}$	115	5930* (3020/2910)	100	96*
500 Å Moly/Copper Layers	$\approx 6 \times 10^{-6}$	75	2945 (1500/1445)	120	129
500 Å Moly/Copper Layers	$\approx 6 \times 10^{-6}$	95	4128 (2128/2000)	!100	92
500 Å Moly/Copper Layers	$\approx 6 \times 10^{-6}$	115	4551 (2500/2051)	100	105
500 Å Moly/Copper Layers	5×10^{-5}	115	4172 (2172/2000)	100	106
500 Å Moly/Copper Layers	1×10^{-4}	115	2598 (1500/1098)	100	113
500 Å Moly/Copper Layers	2×10^{-4}	115	1841 (1000/841)	1000	92
500 Å Moly/Copper Layers	3×10^{-4}	115	1473 (973/500)	100	92
500 Å Moly/Copper Layers	5×10^{-4}	115	1309 (809/500)	100	99

* Mean values based on five separate tests rather than the two tests used
   for each moly/copper configuration tested.

total erosion depth (and in parenthesis erosion depths for the molybdenum or stainless steel [first] / copper [second]) measured after each test is recorded in column four. The durations of the tests producing these erosion depths is given in column five. Column six contains the calculated time required to erode through the depths of the two materials given in column four assuming they have the same erosion rates as the pure materials (from Figures 17 and 19). Typically the calculated erosion time agrees with the measured test duration to within about 10%. This suggests that multilayered molybdenum/copper test patches could be used in argon thrusters to determine erosion rates to within an accuracy of about $\pm$ 10% also.

Table VI contains similar multilayered erosion test patch data obtained using 105 eV mercury ions as the bombarding species. As in Table V the fifth and sixth columns contain the time required to conduct the test and the time that should have been required to erode through the measured depth if erosion rates for the pure base materials at the specified energy and nitrogen partial pressure (from Figures 18 and 20) had been used. In these tests the calculated erosion times are observed to be 10 to 25% below the measured erosion times. This suggests that a phenomenon such as coning may be coming into play when mercury sputtering occurs and that it may be reducing the erosion rates below those expected from measurements obtained on pure materials. Based on these results one would expect 10 to 25% errors in erosion rates obtained using multilayer erosion badges in mercury ion thrusters.

TABLE VI

Sputter Erosion Characteristics

of Multilayered Test Samples in a Mercury Ion Beam

Test Sample Configuration	Nitrogen Pressure (torr)	Mercury Ion Energy (eV)	Erosion Depth (Å)	Test Duration (min)	Calculated Erosion Time (min)
500Å Moly/Copper layers	$\lesssim 1 \times 10^{-6}$	105	2150 (1150/1000)	180	163
500Å Moly/Copper layers	5×10^{-5}	105	1650 (1000/650)	180	142
500Å Moly/Copper layers	1×10^{-4}	105	1760 (1000/760)	240	182
500Å Moly/Copper layers	2×10^{-4}	105	1680 (1000/680)	240	202

SERT II THRUSTER TESTS

Two 15 cm dia., mercury, SERT II thrusters,[22] which were placed in earth orbit February 3, 1970, have been the subject of various tests since that time. Some of the tests have been formulated since the launch date as a result of the changing status of the spacecraft and thruster capabilities identified as desirable in the intervening time. It has been considered desirable to know some characteristics of the thruster plasma and discharge chamber that are not measured on the spacecraft. Ground based tests have therefore been performed under this grant to provide data in support of these space tests.

The SERT II thrusters have both been operated with their grids shorted together and without any high voltage applied to them. The propellant flow rate required to effect discharge operation at the associated currents and voltages were however not known. Flow rate data were measured in ground tests at discharge conditions similar to those measured in space and the results are given in Table VII.

Table VII

SERT II Thruster Flow Rate Data (High Voltage Off)

Dischg. Current (A)	Dischg. Voltage (V)	Keeper Voltage (V)	Main Vaporizer Flow rate (mA eq.)
2.17	39.6	9.4	129
2.11	36.6	8.9	153
2.00	34.7	9.1	190

Mercury flow rates given in Table VII were measured by timing the fall of a mercury column in a 0.9 mm bore glass tube over a period of several minutes. They are considered accurate to within $\pm$ 5 mA. The data of Table VII were obtained with the cathode heater operating at the low power level associated with SERT II thruster operation. Operation at the discharge

conditions of Table VII with this power increased to near its maximum value during another test resulted in flow rates that were a few milliamps lower.

The current drawn to the SERT II neutralizer keeper with the neutralizer off was measured as a function of keeper voltage over a range of flow rates first with the high voltage off and then with it on. The results of these measurements are given in Figure 21 along with corresponding mass flow rates ($\dot{m}$), discharge voltages (V_D), and when the high voltage is on, beam currents (I_B). Keeper voltage is measured relative to vacuum facility ground. With the high voltage on the collected current is seen to be smaller and with the high voltage off the collected current is of the order of the 65 mA measured on-board the spacecraft when its thrusters are operated with a 235 volt keeper bias. The collected current is observed to increase as propellant flow rate is reduced with no high voltage. This behavior is probably a result of the increase in primary electron energy associated with the increase in discharge voltage brought on in turn by the flow rate reduction. This increase in keeper current occurs then because a high primary electron energy facilitates electron escape from the discharge chamber through the grids.

Plasma property data were collected in the beam of a SERT II thruster operating at conditions close to those of the thrusters operating in space with the high voltage on. Figure 22 shows the variation in plasma potential, electron density and electron temperature as a function of radius measured from the thruster centerline at axial locations 5 cm, 15 cm and 75 cm downstream of the accelerator grid. These data were obtained using a spherical, platinum Langmuir probe 2.2 mm in diameter. The thruster was operating under throttled conditions at a beam current of 85 mA, a neutralizer keeper current and voltage of 0.2 A and 28 v respectively and main, cathode
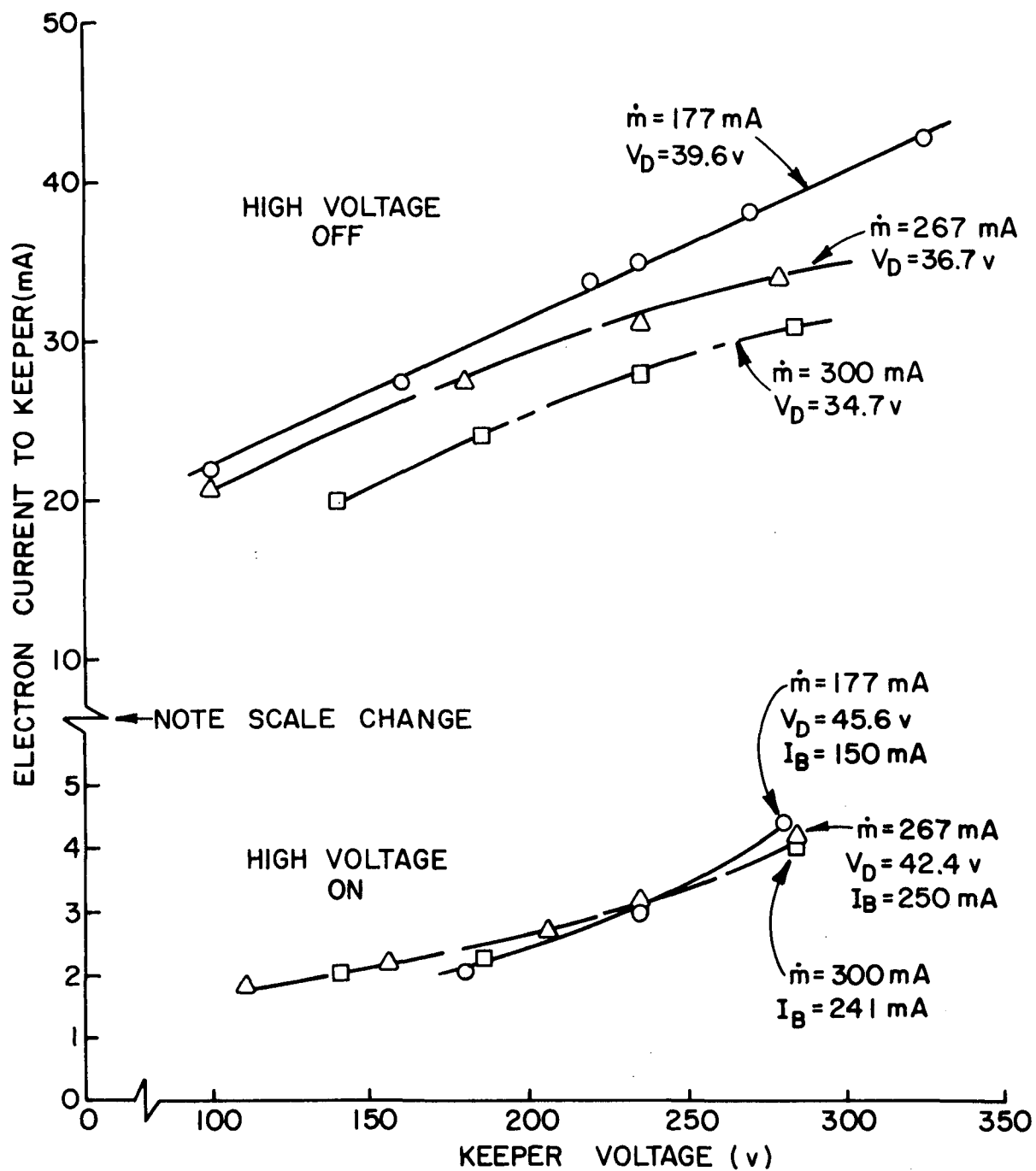
Fig. 21. SERT II Neutralizer Keeper Current Collection
Characteristic - No Neutralizer Flow

PLASMA POTENTIAL (v)

15 cm DOWNSTREAM
OF GRID

75 cm DOWNSTREAM
OF GRIDS

5 cm DOWNSTREAM
OF GRIDS

ELECTRON DESITY 2.0 × 1.0^9 (cm^{-3})

BEAM CURRENT = 85 mA
NEUT. BIAS = 9v BELOW
TANK GROUND

DISCHG. CURRENT = 0.75 A
DISCHG. VOLTAGE = 38 v

V+ = 3 kv
V- = 1.8 kv

ELECTRON TEMP. (eV)

-30   -20   -10   ₵   10   20   30

├─THRUSTER─┤   RADIUS (cm)
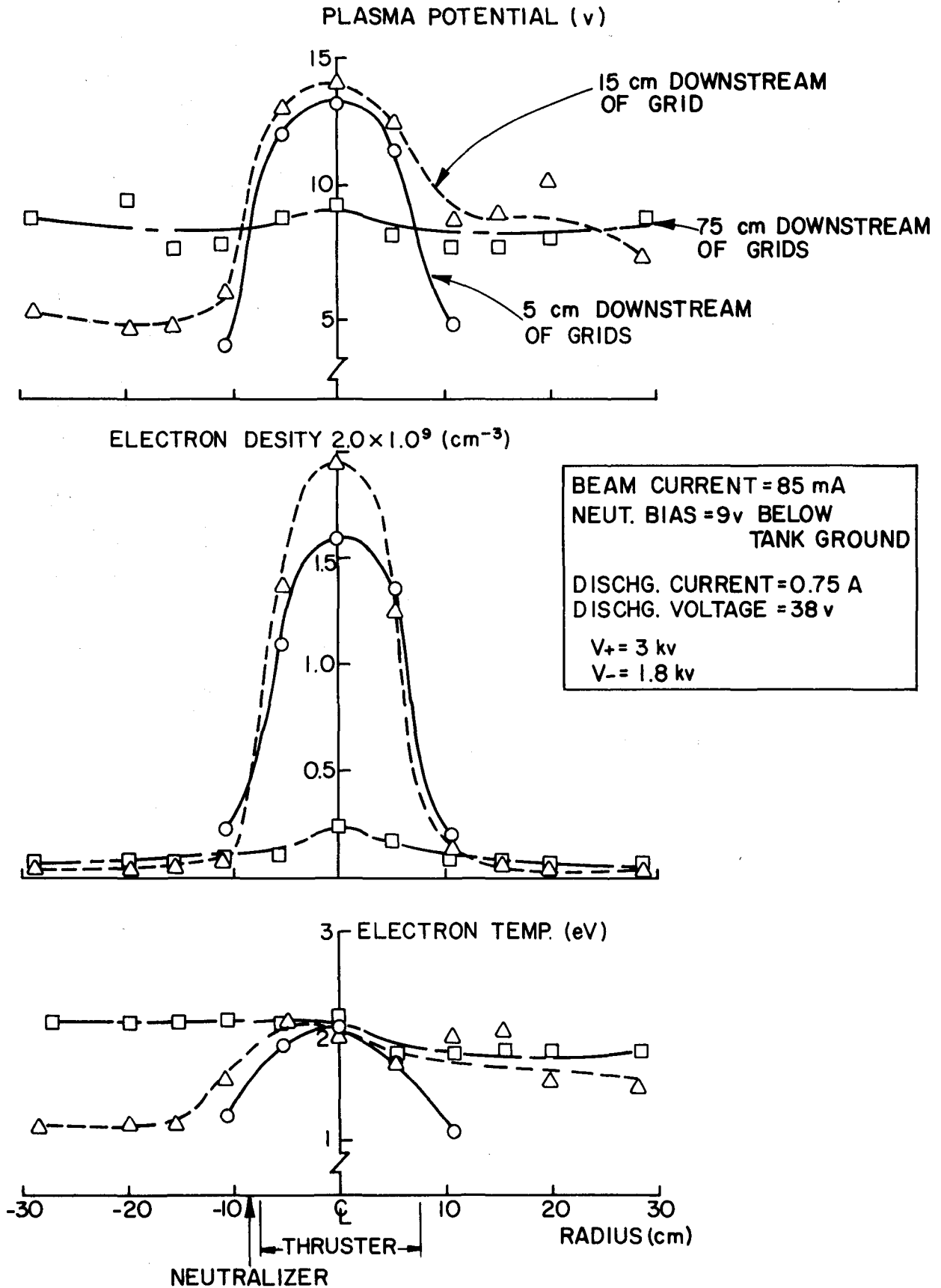
NEUTRALIZER

Fig. 22.   SERT II Beam Plasma Properties

and neutralizer flow rates of 11, 120 and 25 mA respectively. The power supplies were connected in the manner indicated in Figure 23 during the collection of these data. The zener diode clamping circuit acts as an open circuit unless the voltage across it rises above the ~200v set point where it conducts.

For a neutralizer bias voltage of zero, V_G was -9v (neutralizer cathode 9 volts below tank ground). As the bias voltage was varied over a range of several volts, V_G changed such that the neutralizer cathode remained at this same -9v potential and the plasma properties in the beam remained unaltered. The plasma properties in the ion beam were also the same as those shown in Figure 22 when the zener diode clamping circuit was removed and replaced by a power supply used to hold the neutralizer bias voltage at the -9v bias condition where the neutralizer emission balanced the ion beam current. Langmuir probe trace noise was however less significant when the zener diode clamping circuit was in use and the neutralizer emission current was automatically forced to be equal to the beam current.
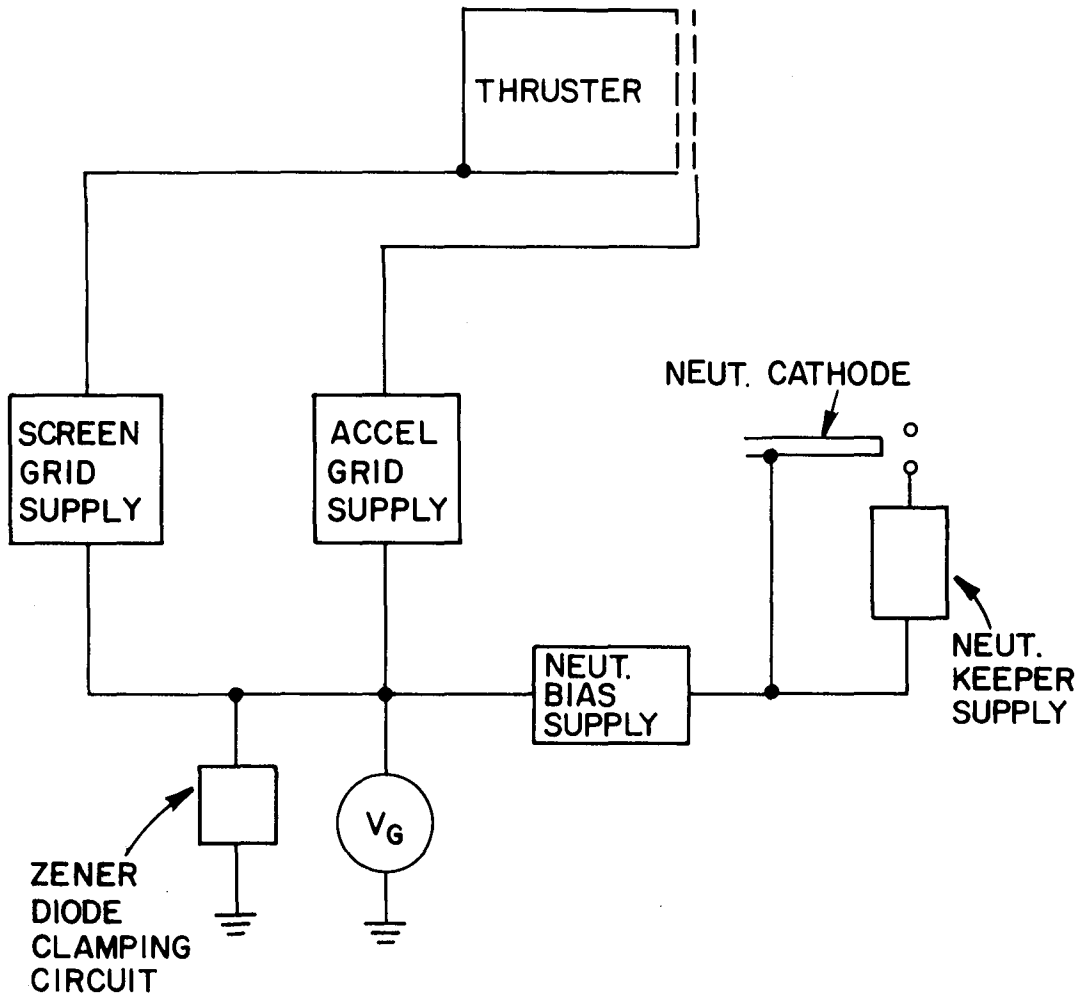
Fig. 23. SERT II Test Circuit Diagram

ELECTROTHERMAL RAMJET

The increased use of space for the benefit of society has pointed the need for low cost launch systems. One class of these systems, that could be used to launch such materials as those needed for orbital construction projects or radioaactive or toxic chemical wastes for extra terrestrial disposal, would involve high acceleration levels. Included in this class of launch systems are those that involve such devices as the rail gun, mass driver and other electromagnetic accelerators. Because of the high acceleration levels at which these devices could operate, the associated launch tracks would be relatively short and the terminal launch velocity could be achieved while the payload was still close to the earth's surface. Achieving terminal velocity in a short distance is considered desirable because the launch could be effected in a tube of reasonable size which would be sealed during the launch sequence if it was necessary to abort the launch. This could facilitate containment if the launch of toxic or radioactive materials were involved.

Another propulsion concept which may be useful in these high acceleration level missions is the electrothermal rocket concept.[23] In these devices on-board propellant is heated electrically and then discharged through a nozzle to produce thrust. Because the heating is accomplished electrically, hydrogen propellant with its attendant high specific impulse capability can be selected. There are several types of electrothermal rockets. In the resistojet for example the propellant is heated by passing it over current carrying, resistive elements and specific impluses as high as 850 sec (8500 m/sec exhaust velocity)[23] have been achieved. Higher specific impulses can be realized if the material limitations imposed by the heating elements are eliminated and joule heating is accomplished by

passing current directly through the propellant. These electrothermal rockets, known as arcjets, have demonstrated specific impulses as high as 1500 sec (15,000 m/sec exhaust velocity).

A basic electrothermal rocket vehicle which might be used in this application is shown schematically in Figure 24a. This rocket would carry on-board propellant which would be metered into the heating chamber where its temperature could be raised by energy either beamed there electro- magnetically or carried there from rails in the launch tube in the form of electrical current.

For the mission under consideration here however where the launch is accomplished close to the earth's surface and in a relatively short distance it is also practical to distribute the propellant along the launch tube. When this is done the propellant can be collected by the launch vehicle and directed into the heating chamber as it moves along. The class of engine that collects its own propellant as it moves through its environment is the jet engine and the simplest of these is the ramjet. Such an engine is considered in this study because of the associated potential for saving energy, simplifying the design and reducing payload delivery costs. Physically the ramjet would operate in the manner sug- gested by Figure 24b by simply drawing propellant in from the tube through an intake diffuser, heating it electrically and then expelling it through a nozzle. Again energy could be transported into the heating chamber either electromagnetically or in the form of electrical current. No com- pressor or other rotating equipment would be needed although an initial velocity would have to be imparted to the vehicle by a booster rocket, an explosive charge or a low terminal velocity electromagnetic driver.

The purpose of this study is to determine for the high acceleration launch mission under consideration the degree to which the performance

INTAKE
DIFFUSER

PROPELLANT

PAYLOAD

PROPELLANT

ELECTROTHERMAL
HEATING
REGION

NOZZLE

LAUNCH
TUBE
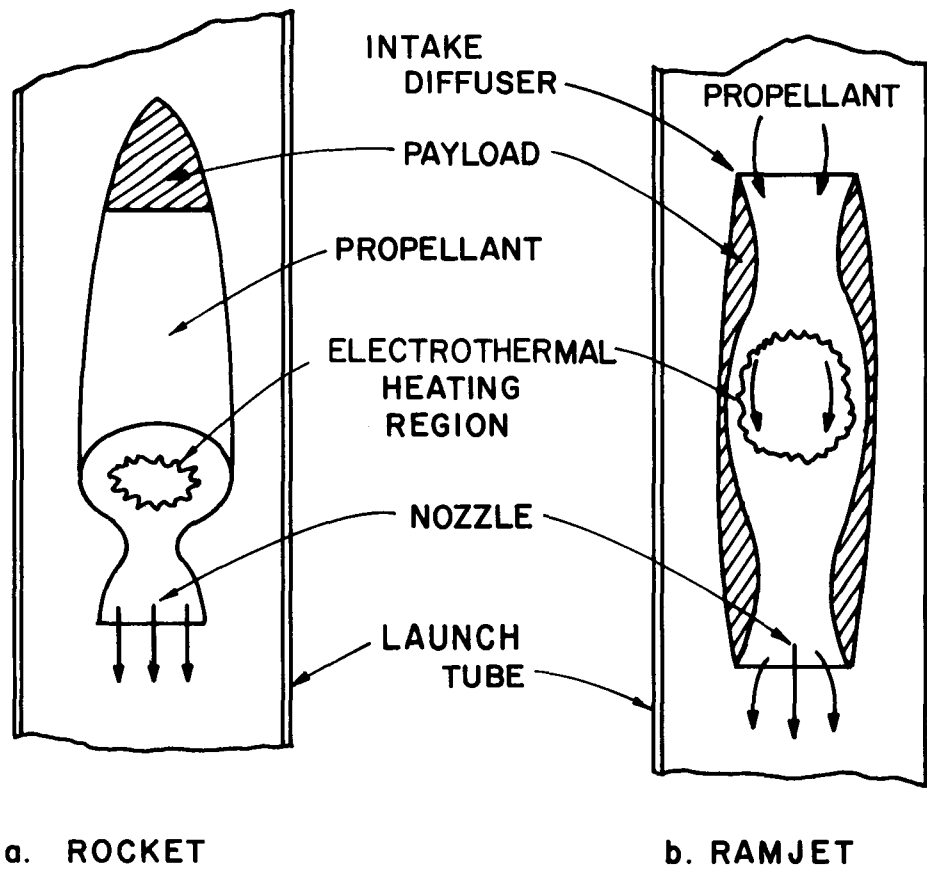
a. ROCKET

b. RAMJET

Fig. 24. Electrothermal Thruster Schematics

of the ideal electromagnetic accelerator might be approached by simpler, presumably less costly and more reliable hydrogen rocket and ramjet engines. The intent of the work described here is to make a preliminary performance comparison of several of these options for a particular mission. The mission selected was a high acceleration earth escape in which sufficient velocity would be imparted to the payload at the earth's surface so that it would be at earth escape velocity when it reached an altitude where atmospheric drag was negligible. The following propulsion schemes are compared in this work:

Thruster	Exhaust Velocity
Chemical Rocket	4,500 m/sec
Resistojet Rocket	8,500 m/sec
Arcjet Rocket	15,000 m/sec
Resisto-ramjet	8,500 m/sec
Arc-ramjet	15,000 m/sec
Electromagnetic gun	--

Constraints at End of Launch Phase

The velocity required at the surface of the earth by a payload intended to escape the earth and the maximum acceleration that such a payload can endure are required as inputs to the problem under consideration. These quantities can be defined if one considers the expulsion of the payload to consist of two phases, namely the launch phase illustrated in Figure 25 and the subsequent phase of vehicle passage through the atmosphere. A vertical launch trajectory is specified and initially the vehicle is assumed to be at rest and to have a mass m_i. When the thruster is started it generates a constant thrust F which produces an initial acceleration σ_i. The launch phase is assumed to continue until time t_f when a terminal launch velocity
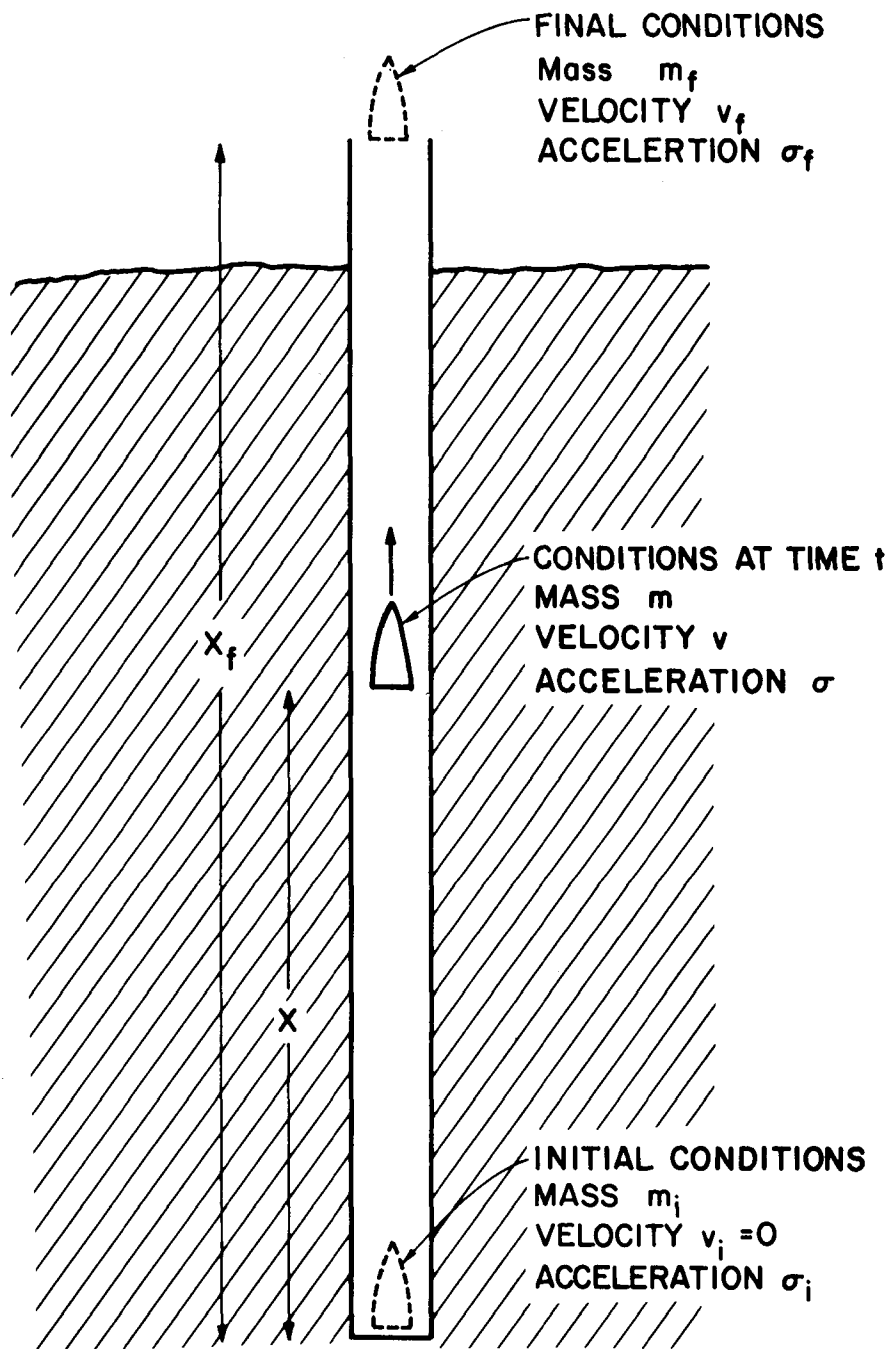
Fig. 25. Launch Phase Nomenclature

v_f is reached. At this point the vehicle mass is m_f, the acceleration is σ_f and the axial location measured from the initial location is x_f. Thrusting stops and the phase of vehicle passage through the atmosphere begins at this point. During this second phase the vehicle velocity decreases as a result of atmospheric drag.

The maximum acceleration (σ_f) that the vehicle can withstand is determined by its mechanical strength. If one assumes the basic vehicle is essentially cylindrical and has a diameter "d" and length "l" then the compressive stress (S) at the base of the vehicle is equal to the thrust force (F) divided by its cross sectional area.

$$S = \frac{4F}{\pi d^2} = \frac{4m_f \, \sigma_f \, g}{\pi d^2} \tag{16}$$

In this equation m_f is the final vehicle mass, σ_f is the final (maximum) acceleration (in G's) and g is the acceleration due to gravity. The ballistic coefficient of the vehicle (B), which pertains to movement through the atmosphere after launch, is given by

$$B = \frac{C_D \, \pi d^2}{4 \, m_f} \, . \tag{17}$$

In this equation C_D is the vehicle drag coefficient and it should have a value near 0.1 for the velocities under consideration here. Combining Eqs. 16 and 17 and solving for the maximum acceleration one obtains

$$\sigma_f = \frac{BS}{C_D \, g} \, . \tag{18}$$

Using Figure 26[24] which was obtained from NASA one determines that a reasonable value for the ballistic coefficient is B = 2 X 10^{-5} m^2/kg. At this value the ratio of atmospheric entrance velocity to the earth escape velocity (v_{esc} =11,200 m/sec) is just under 1.2 and the terminal launch velocity (v_f) would therefore have to be about 13,000 m/sec. If one specifies an
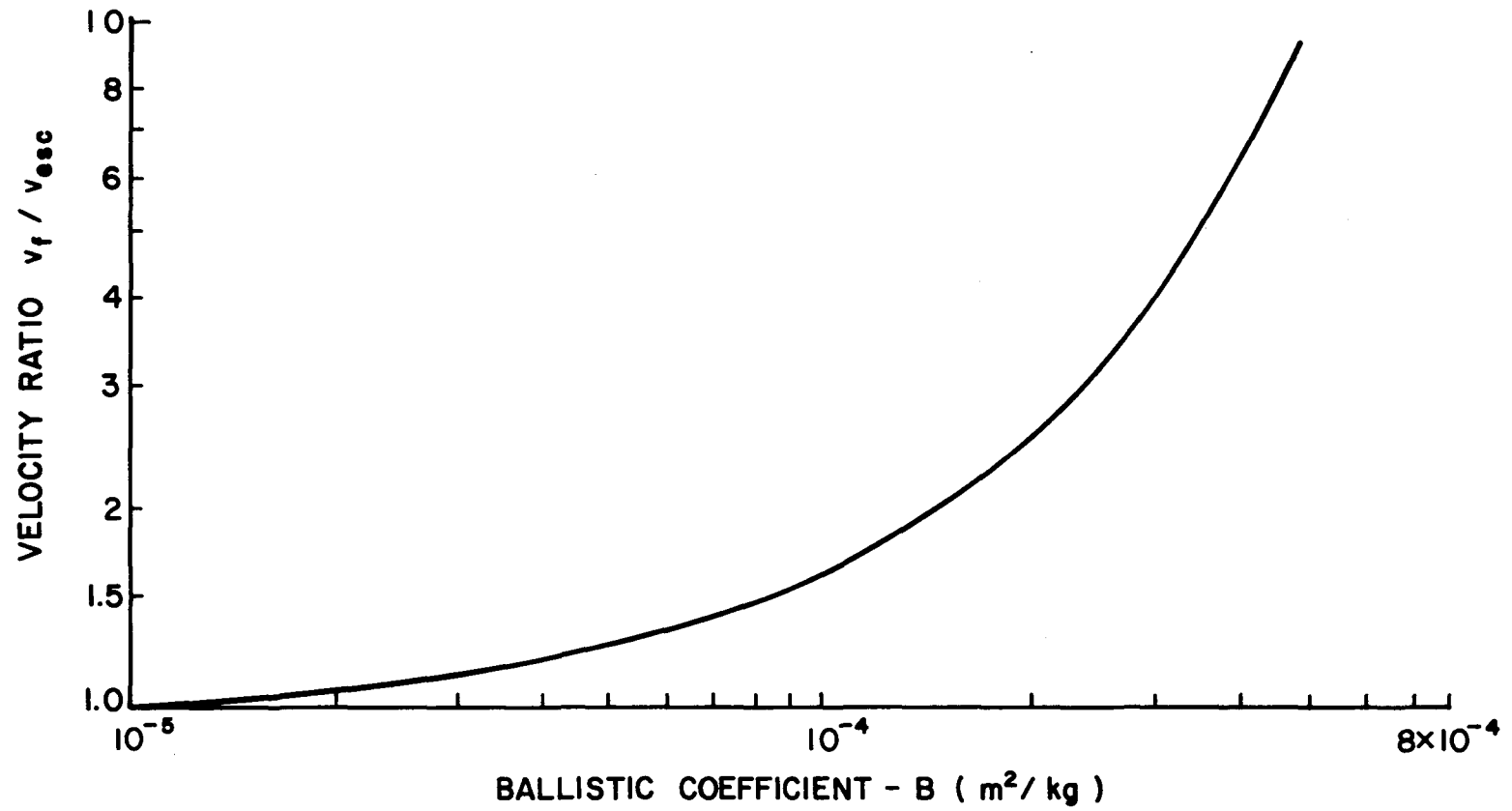
Fig. 26. Velocity Loss Through Atmospheric Drag

allowable stress in the vehicle of 1.4×10^9 nt/m^2 ($\sim$200,000 psi) then the maximum allowable acceleration (Eq. 18) becomes

$$\sigma_f = \frac{(2 \times 10^{-5})(1.4 \times 10^9)}{(0.1)(9.8)} \doteq 30,000 \text{ G's}$$

This acceleration should not be exceeded if compressive stresses are to be held below 1.4×10^9 nt/m^2 during the launch to a velocity of 13 km/sec. This velocity will be sufficient to enable escape from the earth when the vehicle diameter is given by Eq. 16.

Results

A mathematical model developed from a dynamical force balance and energy conservation analysis for each of the thruster cases considered is presented in Appendix B. In each case constant thrust and, for the rockets and ramjets, constant exhaust velocity has been assumed. The results were obtained for a particular case where a 10 kg final mass was launched vertically on an earth escape trajectory. The 10 kg final mass was selected rather arbitrarily but the basic trends and comparisons made here are not affected by this selection.

Figure 27 shows the velocity profiles for the six thruster options being compared. The effect of increasing rocket exhaust velocity from 4,500 to 15,000 m/sec is observed to be a three-to-fourfold reduction in the launch time and a two-to-threefold reduction in the required launch track length (x_f). This points out the great benefit of using the high exhaust velocity electrothermal rocket rather than the conventional chemical rocket motor which is characterized by the lower exhaust velocity. By using a ramjet rather than a rocket further reductions in launch times and track lengths are realized at a given exhaust velocity. This occurs

CONSTANT THRUST
CONSTANT EXHAUST VELOCITY
σ_f = 30000 G's

ELECTROMAGNETIC GUN, X_f = 285 m

RAMJET, U = 15000 m/sec, X_f = 285 m

ROCKET, U = 15000 m/sec, X_f = 390 m

RAMJET, U = 8500 m/sec, X_f = 510 m

ROCKET
U = 8500 m/sec
X_f = 570 m

ROCKET
U = 4500 m/sec
X_f = 970 m
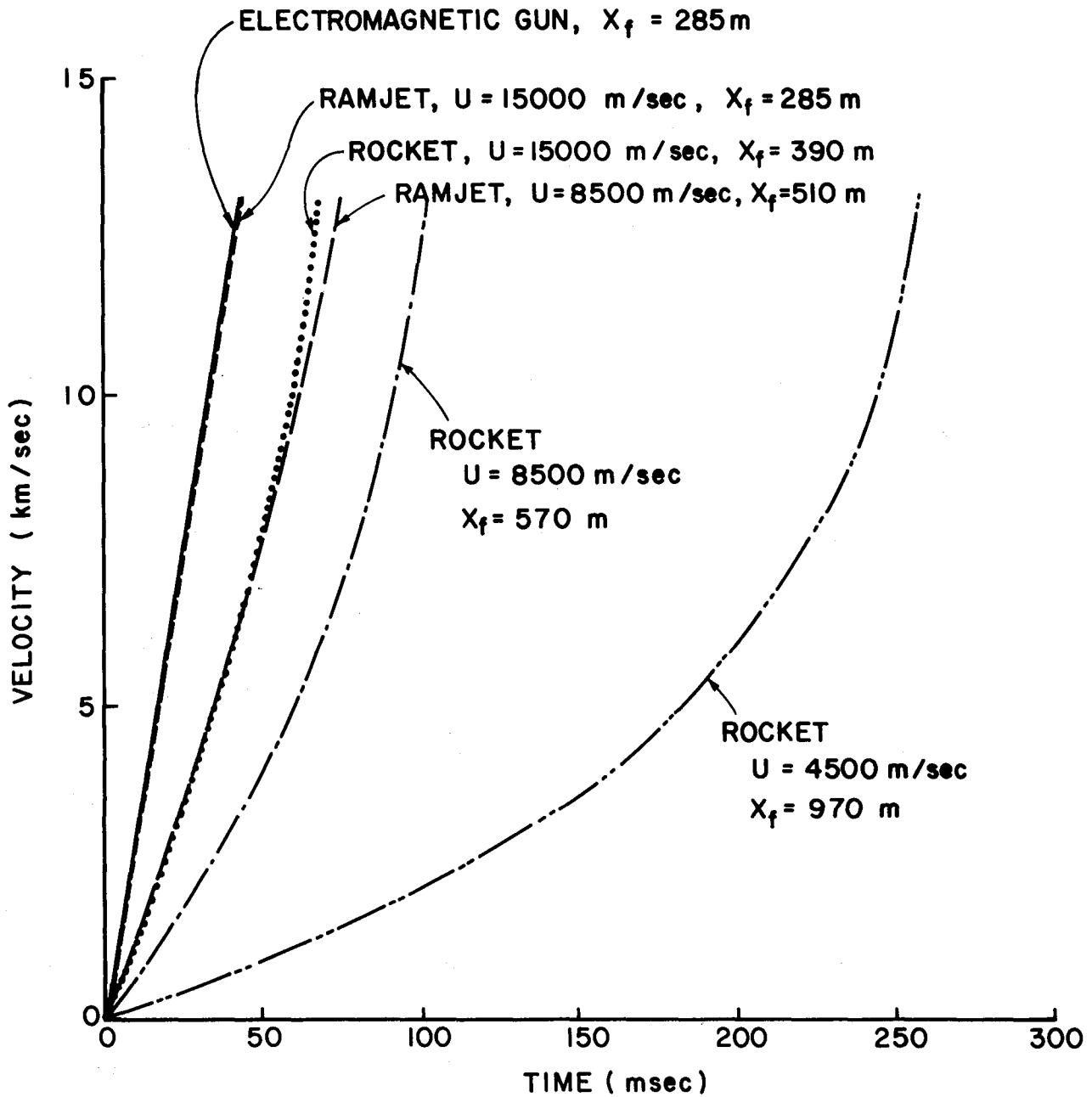
Fig. 27. Velocity Profile Comparison

because the on-board propellant need not be accelerated in the case of the ramjet. At an exhaust velocity of 15,000 m/sec the ramjet performs essentially the same as the electromagnetic accelerator in that it requires the same track length (285 m) and launch time (44 msec). The 8,500 m/sec ramjet is seen to exhibit performance comparable to the 15,000 m/sec rocket.

Figure 28 shows the time profile of the vehicle acceleration for the various thrusters. The acceleration is limited to 30,000 G's and this implies considerably lower initial accelerations for the conventional rockets in which the vehicle mass must decrease with time as on-board propellant is discharged. The shorter launch times and track lengths given in Figure 27 are seen to occur for the cases where the acceleration remains closer to the limiting value throughout the launch.

A discussion of the variation in acceleration for the 8.5 km/sec ramjet will facilitate an understanding of some of the physical character-istics of this thruster. During the first ten milliseconds or so the acceleration of the 8.5 km/sec ramjet increases because on-board mass is being expelled to accelerate the vehicle to the point where the ram pressure is sufficient to effect ramjet operation. This decrease in mass causes the acceleration level to increase with time. During the interval from 10 to 50 milliseconds, ramjet operation occurs and the vehicle acceleration is constant. Near the 50 millisecond point the vehicle velocity gets suf-ficiently close to the thruster exhaust velocity so that ramjet operation is no longer possible.* This means on-board propellant must again be used and

---

* Application of the momentum balance equation demonstrates that the thrust (F) goes to zero as the vehicle velocity (v) approaches the exhaust velocity (U), unless the propellant flow rate ($\dot{m}$) becomes infinitely large (F = $\dot{m}$ [U-v]).

CONSTANT THRUST
CONSTANT EXHAUST VELOCITY
σ_f = 30000 G's

ELECTROMAGNETIC GUN
RAMJET, U = 15000 m/sec
ROCKET, U = 15000 m/sec
RAMJET, U = 8500 m/sec
ROCKET
U = 8500 m/sec
ROCKET
U = 4500 m/sec

ACCELERATION (G's)

3×10^4
10^4
10^3

TIME (msec)
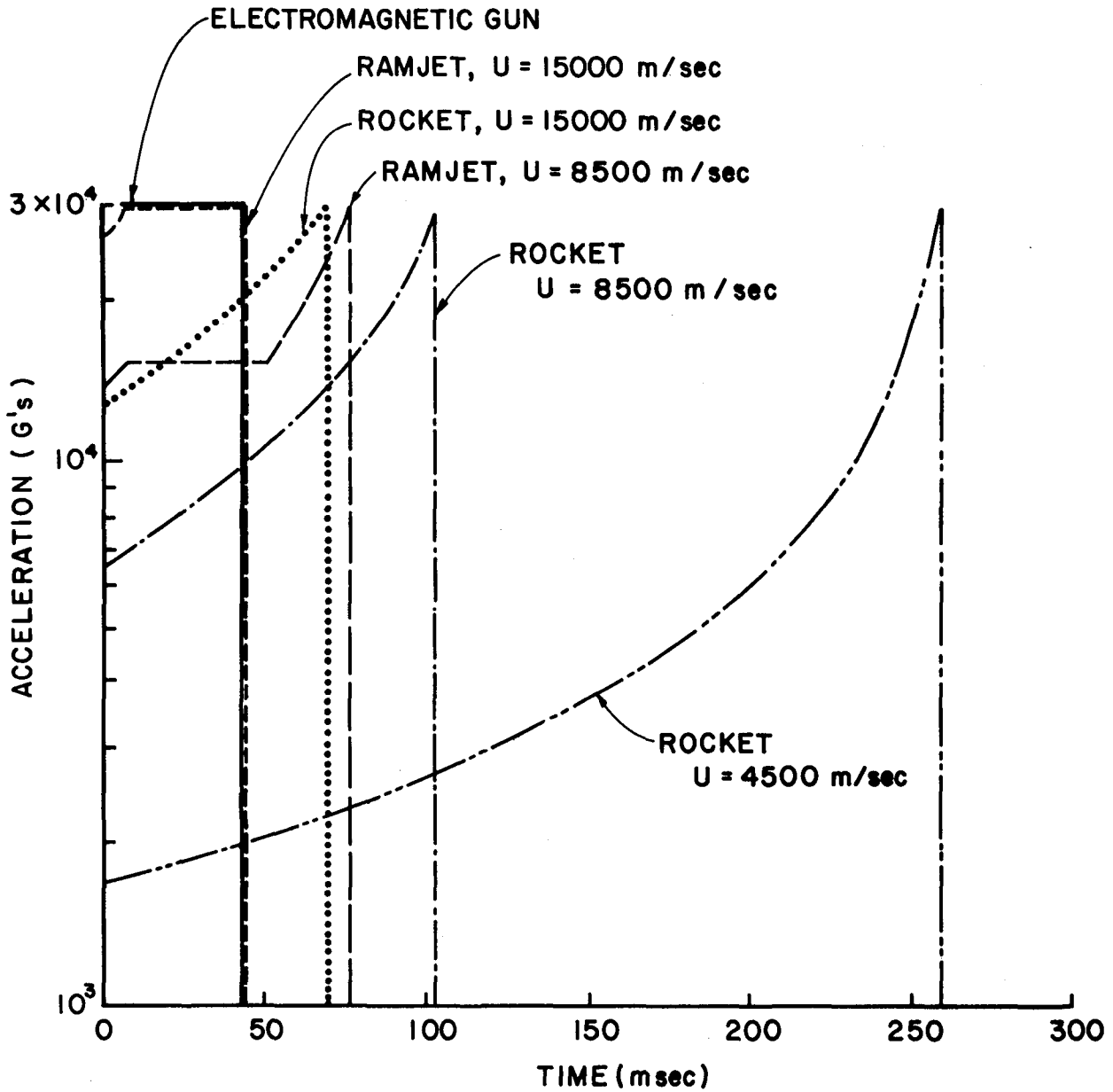
Fig. 28. Acceleration Profile Comparison

acceleration again increases with time. This use of on-board propellant continues until the desired final velocity (13 km/sec) is realized. For the 15 km/sec ramjet the final phase wherein on-board propellant is used is not required because the final velocity is significantly less than the exhaust velocity.

Figure 29 shows the variation in vehicle mass with time for each of the thrusters. These curves simply reflect the variations in acceleration observed in Figure 28. It is noteworthy however that the 4,500 m/sec conventional rocket requires an initial mass of 180 kg to deliver a final mass of 10 kg at 13 km/sec while the 15,000 m/sec ramjet can do it with 11.5 kg and the electromagnetic thruster requires only the desired 10 kg as an initial mass.

The power profiles for each operating condition are compared in Figure 30. The total energy (E) required to accelerate the payload to the specified final velocity for each option is obtained by integrating under the power curves and it is also shown in this figure. The variation in total energy required for the launch is seen to be relatively modest between the various modes, but the ramjet and electromagnetic designs are seen to require substantially greater peak power levels. Figure 30 shows that the peak power levels of the high exhaust velocity ramjet and the electro-magnetic gun are comparable. The electromagnetic gun is observed to require the least energy of any option, but it is important to note that this is a highly idealized model. The energy stored in the magnetic fields of this device, when the vehicle leaves the launch track, as well as joule heating losses will be substantial and they have not been included here. Their inclusion could well make the energy required for the electromagnetic gun more comparable to values obtained with the rockets and ramjets.
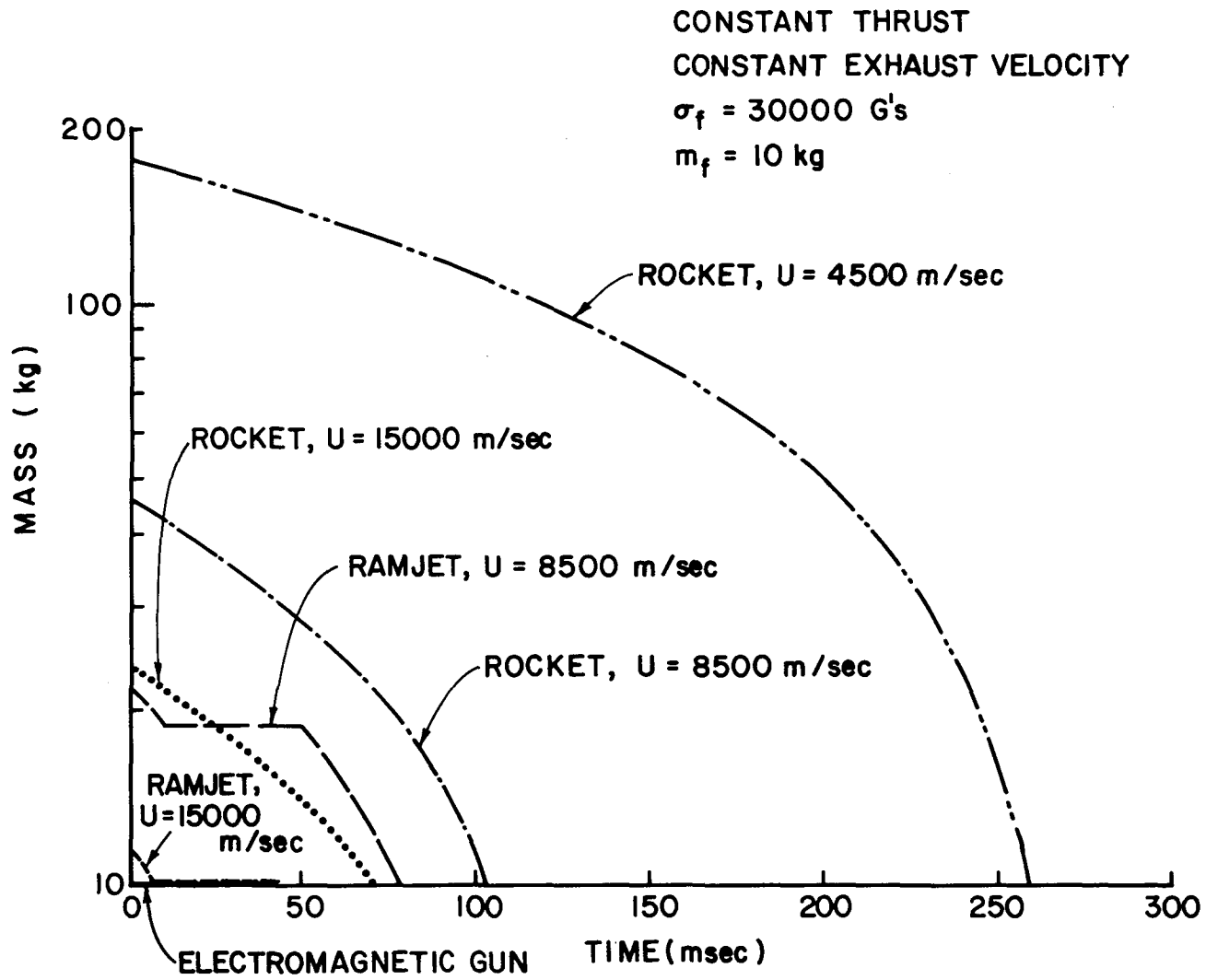
Fig. 29. Mass Profile Comparison
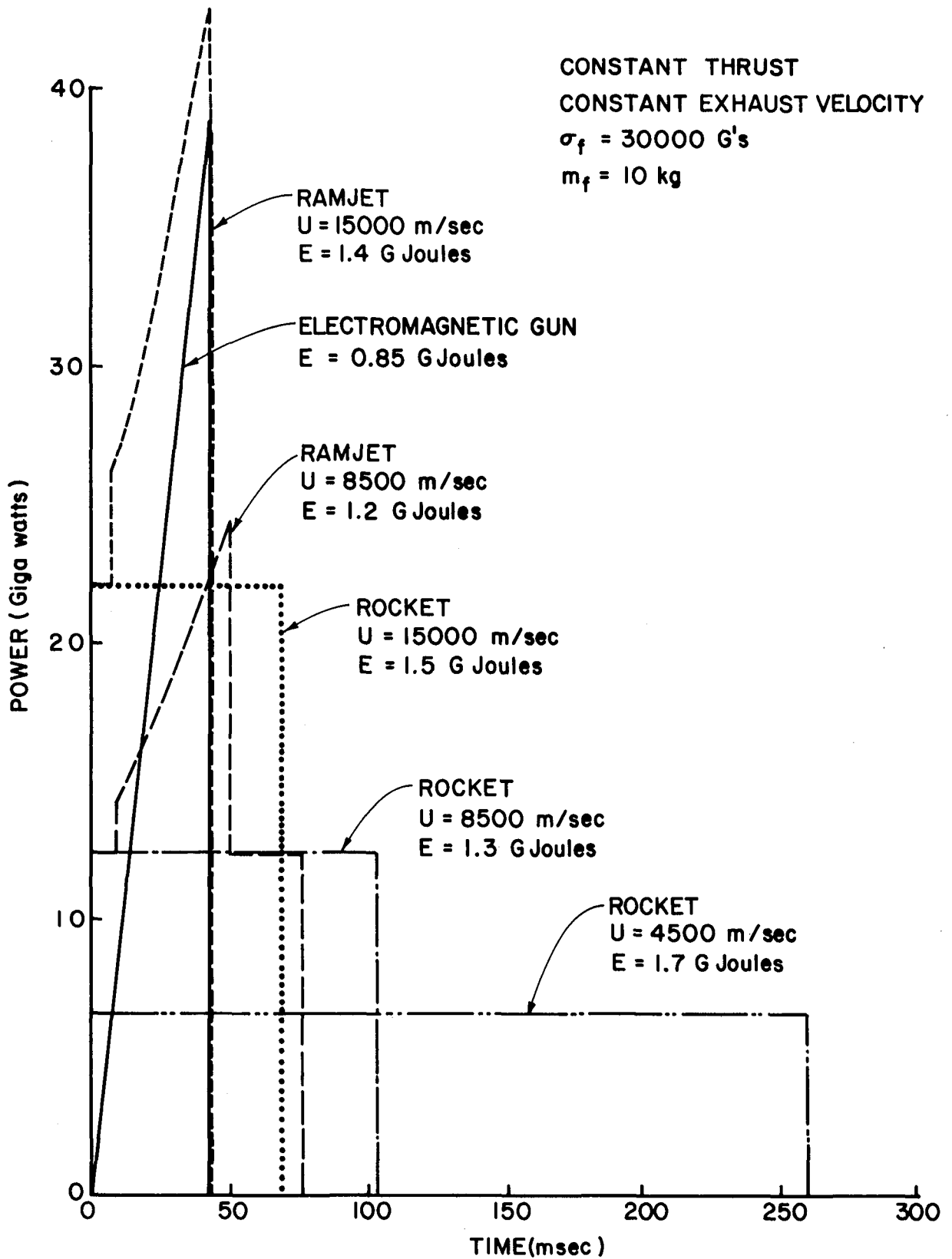
Fig. 30. Power Profile Comparison

It is important to point out that all of the modelling used here is highly idealized. For example losses due to aerodynamic and frictional drag have been neglected for the launch phase, as have propellant pumping powers and losses associated with energy transport through conductors or wave guides. These could change absolute numbers significantly although the comparative results are considered correct.

Conclusions

By using hydrogen propellant in conjunction with an electrothermal thruster one can increase the specific impulse by a factor of two or three over that obtainable with chemical systems. For a high acceleration, escape trajectory launch system the use of such an electric rocket translates into a corresponding theoretical reduction in launch times and track lengths of about the same factor of two or three. Further improvements are realized if a ramjet is used in place of a rocket. For the particular mission considered here an electrothermal ramjet is predicted to exhibit essentially the same performance as such electromagnetic guns as the rail gun or mass driver. Since the electrothermal ramjet has an inherent simplicity that makes it potentially more reliable and less costly than the electromagnetic devices, it appears that it could be a viable alternative. More detailed analysis of the electrothermal ramjet is recommended.

ION BEAMLET VECTORING BY GRID TRANSLATION

John Homa

The study of grid translation effects on ion beam optics has two important applications in the design of electric thrusters. For a dished grid pair, hole misalignments are used to redirect the emerging beamlets in order to minimize the off-axis thrust. A study that would yield correlations or a model of this phenomenon would facilitate design of these grids. In addition, for some applications a vectorable beam is desired,[25] and grid translation is an easily accomplished method of producing a moderate thrust vectoring capability.

Work done by Aston[26] has shown the effects of such parameters as grid separation, grid hole diameter and net-to-total accelerating voltage ratio on optical performance of a two-grid system. Optical performance in this context is defined as the beamlet divergence variation with beam current as well as the maximum perveance that can be obtained. The present study of grid translation is intended to examine the effects of these parameters on vectored beams. Of particular importance is the degradation of optical performance as a function of relative grid displacement expressed in terms of beamlet divergence and maximum perveance capability of vectored beamlets compared to nonvectored ones.

For a simple two-grid system the beam deflection angle can be estimated using linear optics theory[27,28] by

$$\beta = -\varepsilon/(4\ell_g) \, , \tag{19}$$

where ε is the relative accelerator grid displacement and ℓ_g is the grid separation distance. The negative sign indicates that the beam deflection is directed opposite to the direction of relative accelerator grid

displacement. The parameters of Eq. 19 are defined in Fig. 31. This figure also illustrates pertinent grid dimensions including screen and accelerator grid aperture diameters (d_s and d_a), grid thicknesses (t_s and t_a), the grid separation distance (ℓ_g) and the grid offset angle δ. This angle is defined in terms of the linear grid displacement ε by the equation

$$\tan \delta = \frac{\varepsilon}{\ell_g + t_s} \tag{20}$$

Apparatus and Procedure

The beam vectoring study has been initiated on an 8 cm dia., mildly divergent ion source in which the grids have been masked down to a 1 cm^2 aperture area. This masking of the beam results in very uniform plasma properties at each aperture and hence a uniform beam. The thruster uses a tungsten filament cathode and neutralizer and operates with argon as the propellant.

The grids are fabricated from graphite sheets with a hexagonal nineteen hole array. Spacing of the grids is provided by mica insulating sheets. The screen grid can be translated along one axis during thruster operation by a mechanical system coupled to a micrometer assembly as illustrated in Fig. 32, while the accelerator grid is held stationary. The screen grid was selected as the translating grid, because such an arrangement facilitated grid spacing and accelerator grid alterations.

The beam emerging from the grids is probed by a collection of molybdenum, flat plate probes each 1 cm^2 in area, in the manner suggested in Fig. 32. Twenty of these probes are arranged in a horizontal line 14 cm downstream from the grids. In addition, a line of probes extends vertically downward from each end of the horizontal probe rake. By using these three probe rakes
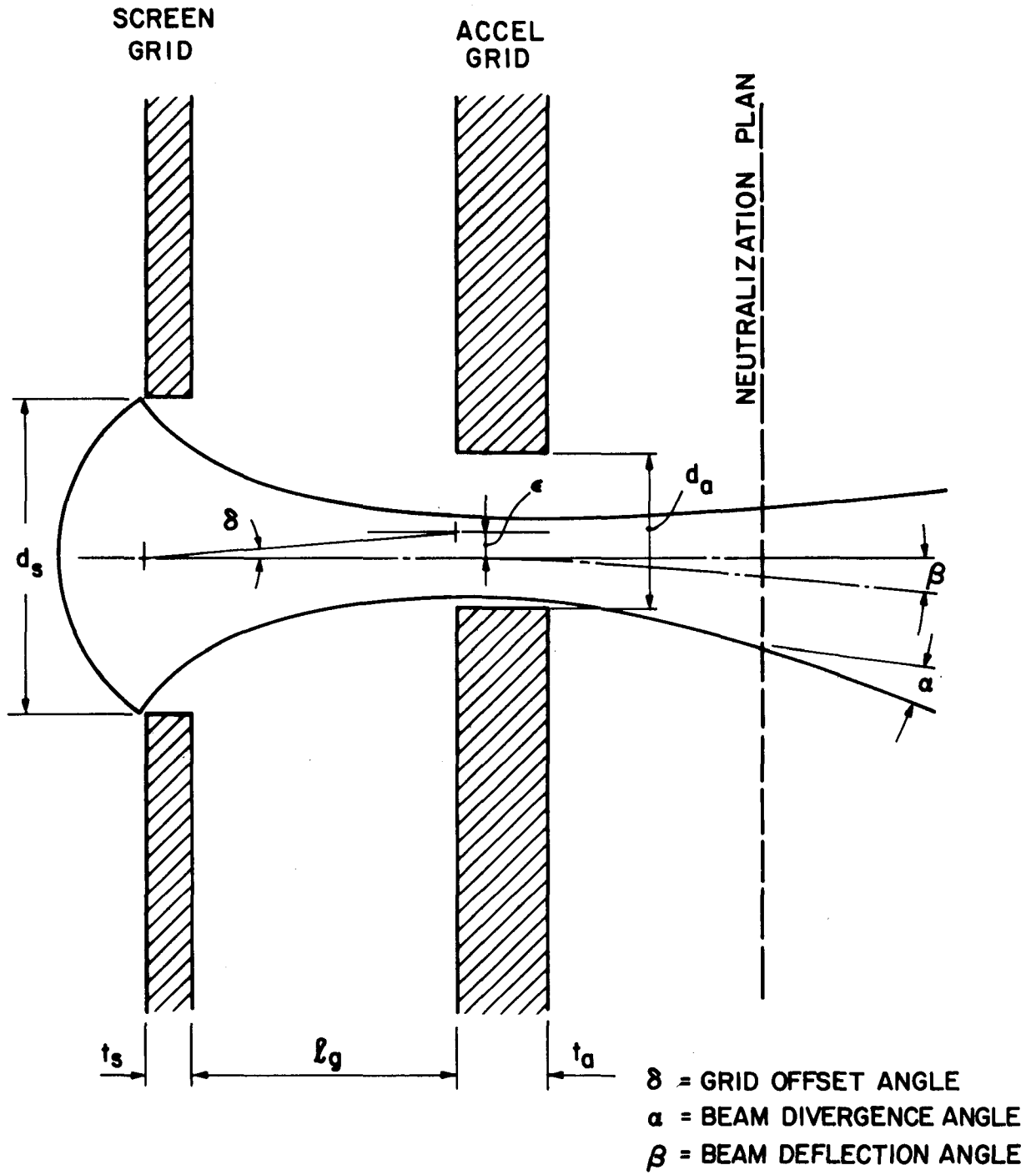
Fig. 31. Deflecting Beamlet Nomenclature

ELECTRON SHIELDING
SCREEN

FARADAY PROBE (typ.)

9.5 cm

HORIZONTAL
PROBE RAKE

VERTICAL
PROBE RAKES

14 cm

8 cm Argon
ION
SOURCE

TO MICROMETER
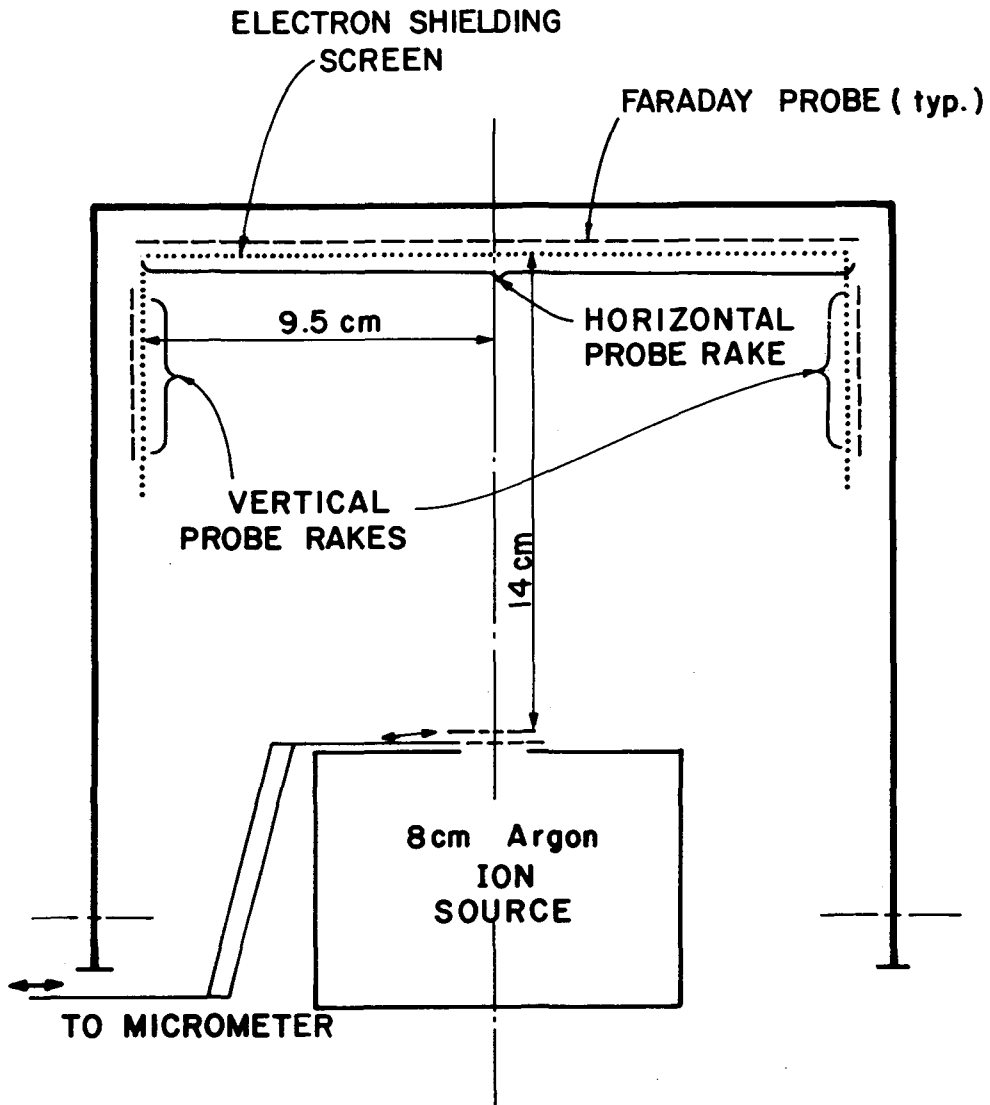
RAKE ASSEMBLY ROTATION
TO FACILITATE ALIGNMENT
WITH BEAM

PROBE RAKE
ASSEMBLY

ION SOURCE
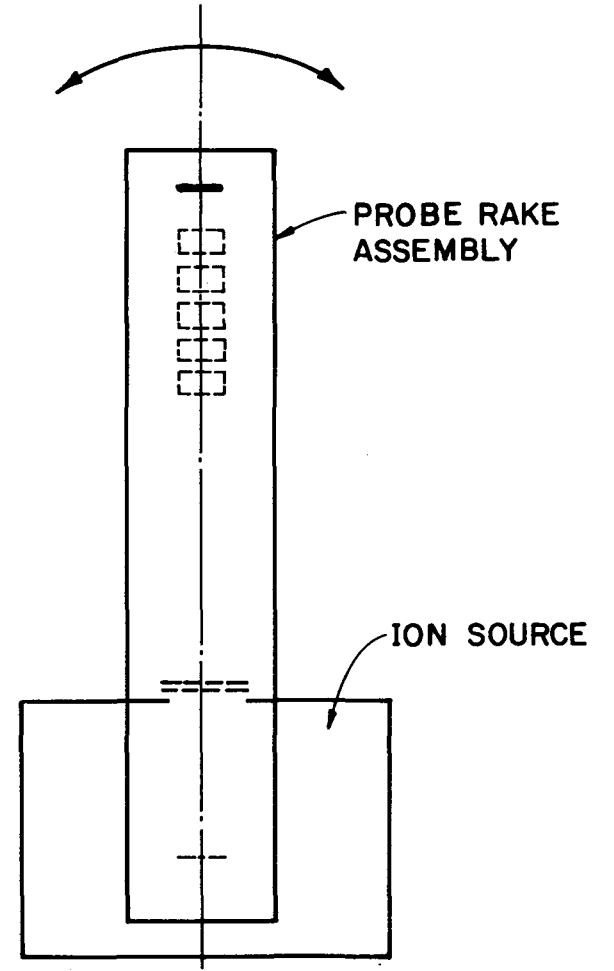
Fig. 32. Deflecting Beamlet Test Apparatus

it is possible to intercept the full beam profile over the complete range
of grid translation. A 70% open area screen is placed in front of the
probes, and is biased 30 v negative relative to ground in order to reflect
neutralizer electrons. The probes themselves are biased 18 v positive
relative to ground to reflect low energy, charge-exchange ions produced
downstream of the grids. The rake assembly is designed so it can be
rotated in the manner suggested in Fig. 32 to facilitate rake axis align-
ment with the beam axis in the plane perpendicular to the direction of grid
translation. Data was initially collected using only the horizontal probe
rake, however beam profiles for vectored beams showed significant currents
being collected on the end probes. The vertical probe rakes were then
added to insure that the entire beam profile was obtained.

Standard thruster operating conditions for preliminary checkout have
been a total accelerating voltage of V_{total} = 600 v with a net accelerating
voltage set to obtain R = V_{net}/V_{total} values of 0.5, 0.7, and 0.9. The
discharge voltage has been 40 v and operating pressures in the range of
2 - 4 X 10^{-5} torr have been used. Once a beam current density profile has
been measured across the beam diameter it is analyzed using a computer
routine. This routine first uses the current density data at the probe
rake locations to compute the current density on a circular arc located on
a 17 cm from the grid center. From this profile the point of maximum
current density is identified. The deflection angle is then computed as
the angle between the perpendicular to the grids and the line from the
screen grid center through the point of maximum current density. Next the
two segments of the current density profile on either side of the maximum
are averaged and the total beam current is estimated by integrating this
average profile for an assumed axi-symmetric distribution about the line

of maximum current density. Inherent in this portion of the analysis is the assumption that the ions are drawn from a point source; this assumption does not introduce a significant error because the beam diameter is small compared to the distance to the probe rake. The beam current obtained in the analysis by integrating the current density is compared to the measured beam current to insure that they agree to within 5-10%. The divergence half angle (α in Fig. 31) is computed as the half angle of the cone enclosing 95% of the integrated beam current determined in the aforementioned analysis. This definition of half angle is the same as the one used in previous work.[26] The 95% criterion was selected as a compromise value that yielded a sensitive indicator of ion beam deflection. A thrust coefficient defined as the fraction of the integrated current that is directed along the deflected beam axis is also calculated.

Results

The data that have been collected so far during this study are considered preliminary, but they do seem to be self-consistent and in agreement with results obtained by others. Figure 33 shows typical results wherein the beam deflection angle (β) is seen to vary linearly with the grid offset angle (δ) over the range $\pm$ 15° ($\pm$ 10° deflection angle). Beyond this point, the accelerator grid impingement current increases rapidly, due to direct interception of the beam, and the beam deflection becomes nonlinear.

The divergence angle and thrust coefficient are shown in Fig. 34, as a function of grid displacement. The graph shows a general increase in divergence angle which reaches a peak near the point at which accelerator impingement increases. The decrease in divergence angle with further grid displacement is probably due to interception by the accelerator grid of
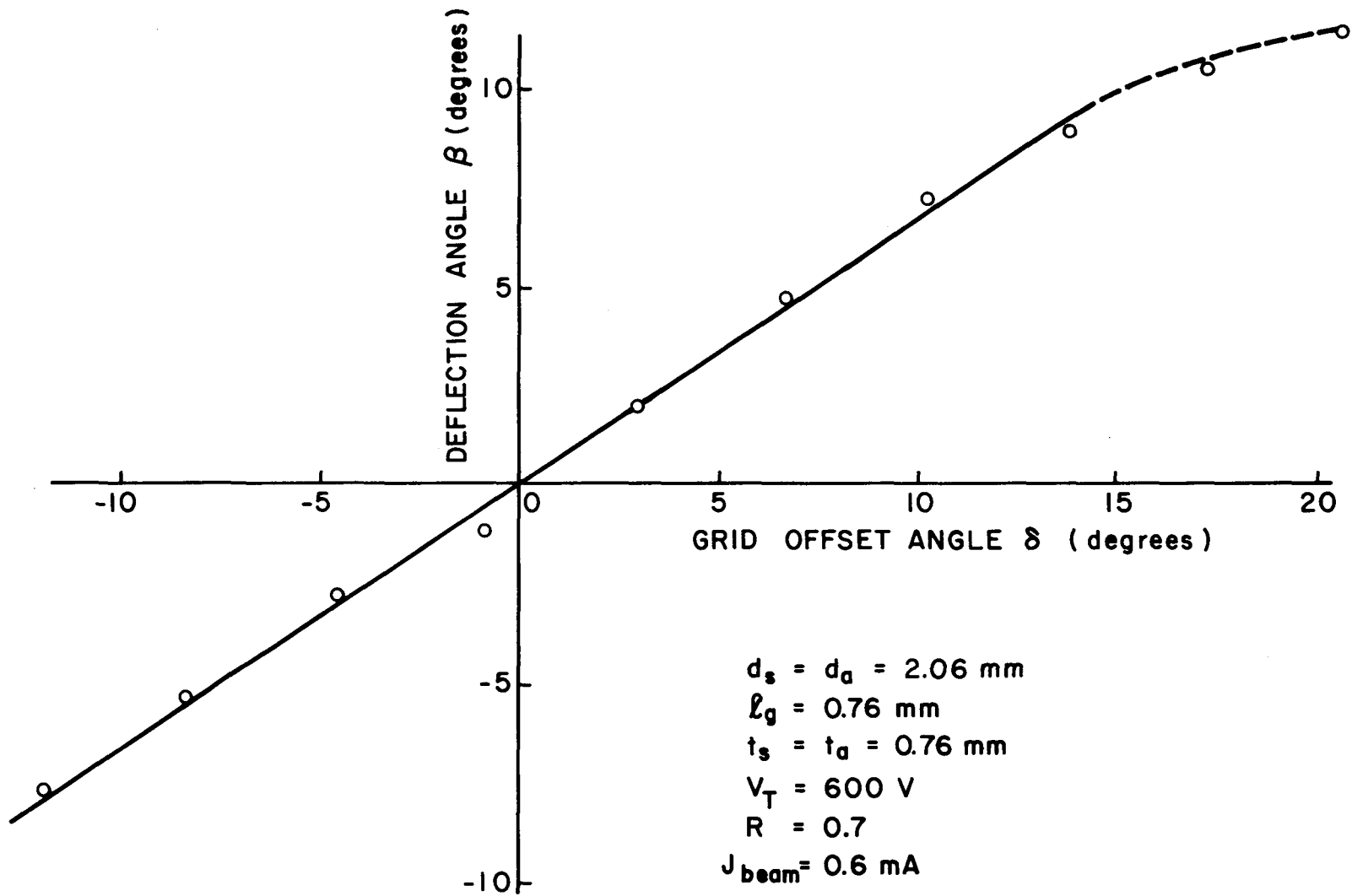
Fig. 33. Beamlet Deflection Characteristic

$d_s = d_a = 2.06$ mm
$\ell_g = 0.76$ mm
$t_s = t_a = 0.76$ mm
$V_T = 600$ V
$R = 0.7$
$J_{beam} = 0.6$ mA
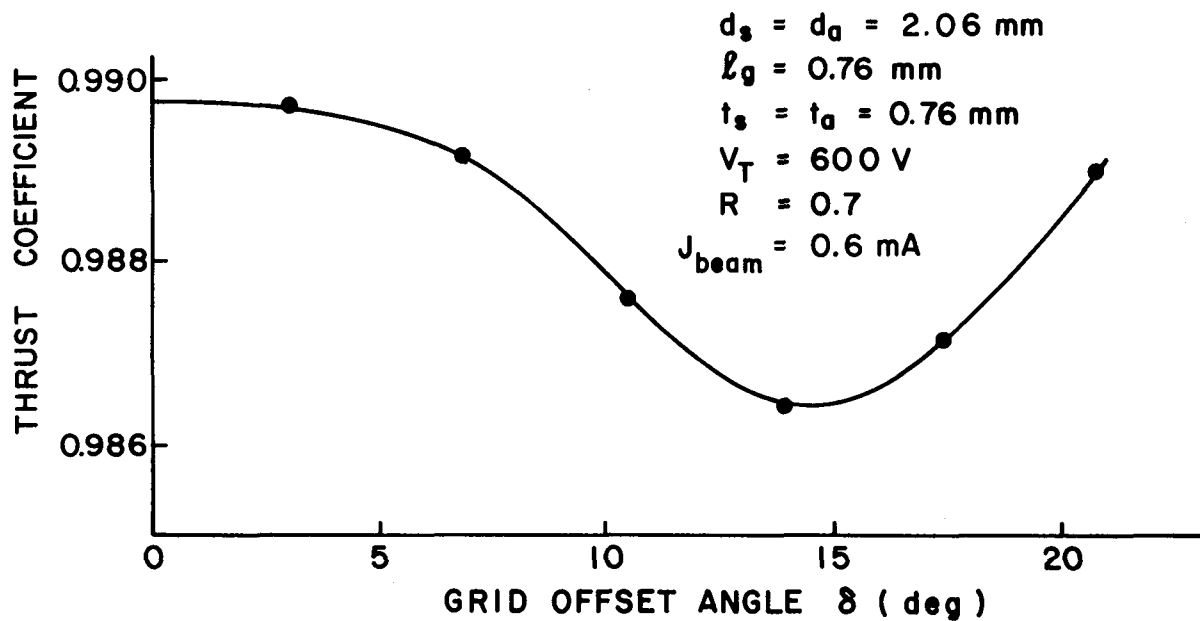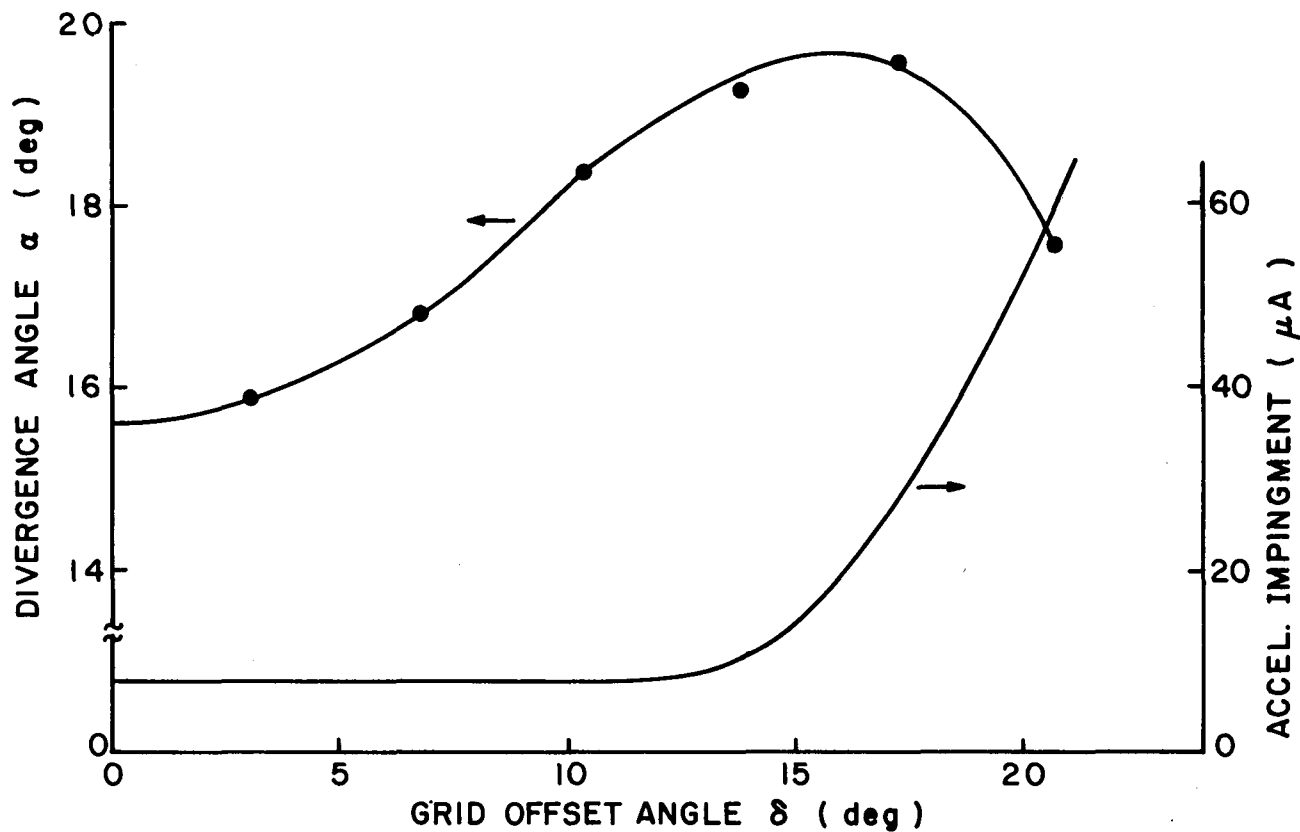
Fig. 34. Beamlet Divergence Characteristic

the beam edge resulting in a less divergent beam. It is noteworthy that the divergence angle is not a strong function of grid offset angle for the particular grid and operating condition being investigated here.

Conclusion

The beam vectoring apparatus functions properly and consistent results have been obtained. Further work is needed to investigate the effects of variations in accelerator and screen grid thicknesses and hole diameters, grid separation total accelerating voltage, and net-to-total accelerating voltage ratio.

MULTIPLE CATHODE STUDY

John R. Brophy

Introduction

One method of increasing the thrust density from electrostatic ion engines is to increase the ion beam current density extracted by the accelerator system. This in turn requires an increase in the plasma density from which the ions are extracted. To increase this plasma density may require that the thruster be operated at discharge currents of several tens of amperes. Cathodes operating at these current levels may also be required in large diameter thrusters. Two methods of generating these high discharge current levels have been suggested. The first requires the development of a high power cathode capable of emitting tens of amperes while still having a lifetime comparable to those of existing cathodes. The second method would involve parallel operation of several conventional hollow cathodes. The number of cathodes would in this case be selected so the emission current requirement for each individual cathode would be within the capability of presently available designs. The problem with this latter solution is the tendancy for cathodes to share the emission load unequally during operation or for some of the cathodes to fail to start. The experiment described in this section was designed to determine how this potential problem might be overcome.

Apparatus

A 15 cm diameter multipole thruster[29] was modified to operate with two hollow cathodes supplying electrons to the main discharge chamber in the manner suggested by Fig. 35. The cathode discharge region as shown here is seen to be a torus of rectangular cross section that is connected
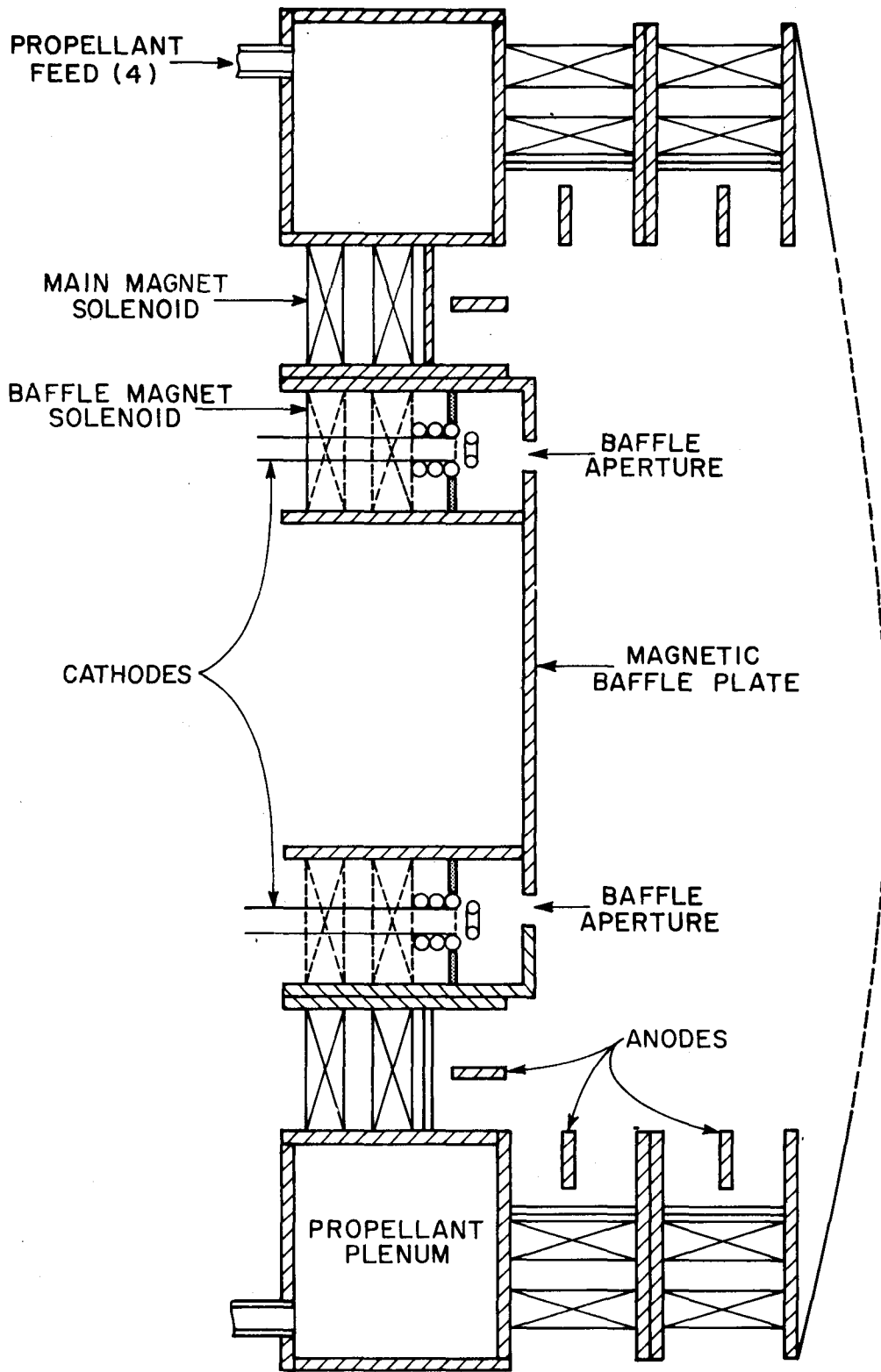
Fig. 35. 15 cm Multipole Multicathode Thruster

to the main discharge chamber by an annular baffle aperture on its down-stream side. The cathodes are located diametrically opposite each other at the upstream side of the cathode discharge region. Each cathode is electrically isolated from the other one and from the thruster body as suggested by the electrical schematic shown in Fig. 36. In order to achieve complete isolation of the two cathodes it was necessary to use separate keeper, vaporizer and tip heater power supplies as well as separate propellent feed systems for each cathode. Electrical isolation of the cathodes was required to facilitate measurement and subsequent control of the two emission currents. The separate propellent feed systems were required not only for the electrical isolation of the cathodes but also to facilitate independent measurement of the flow rates to each cathode.

Discussion

The first problem encountered in the operation of the multi-cathode thruster was associated with the ignition of both hollow cathode/keeper discharges. On several occasions it was observed that the initiation of one of the cathode/keeper discharges, while the second discharge failed to start, resulted in coupling of the plasma from the operating cathode to the keeper of the nonemitting cathode. This coupling effectively prevented the ignition of the second cathode. To assure that both cathodes could be started it was found that they had to be isolated from each other, either with a physical or a magnetic barrier, that prevented this coupling. In the thruster configuration tested here it was found that increasing the magnetic baffle current would create a leakage magnetic field of sufficient magnitude to isolate the cathodes. Isolating the cathodes with a magnetic field in this manner generally allowed both cathodes to be
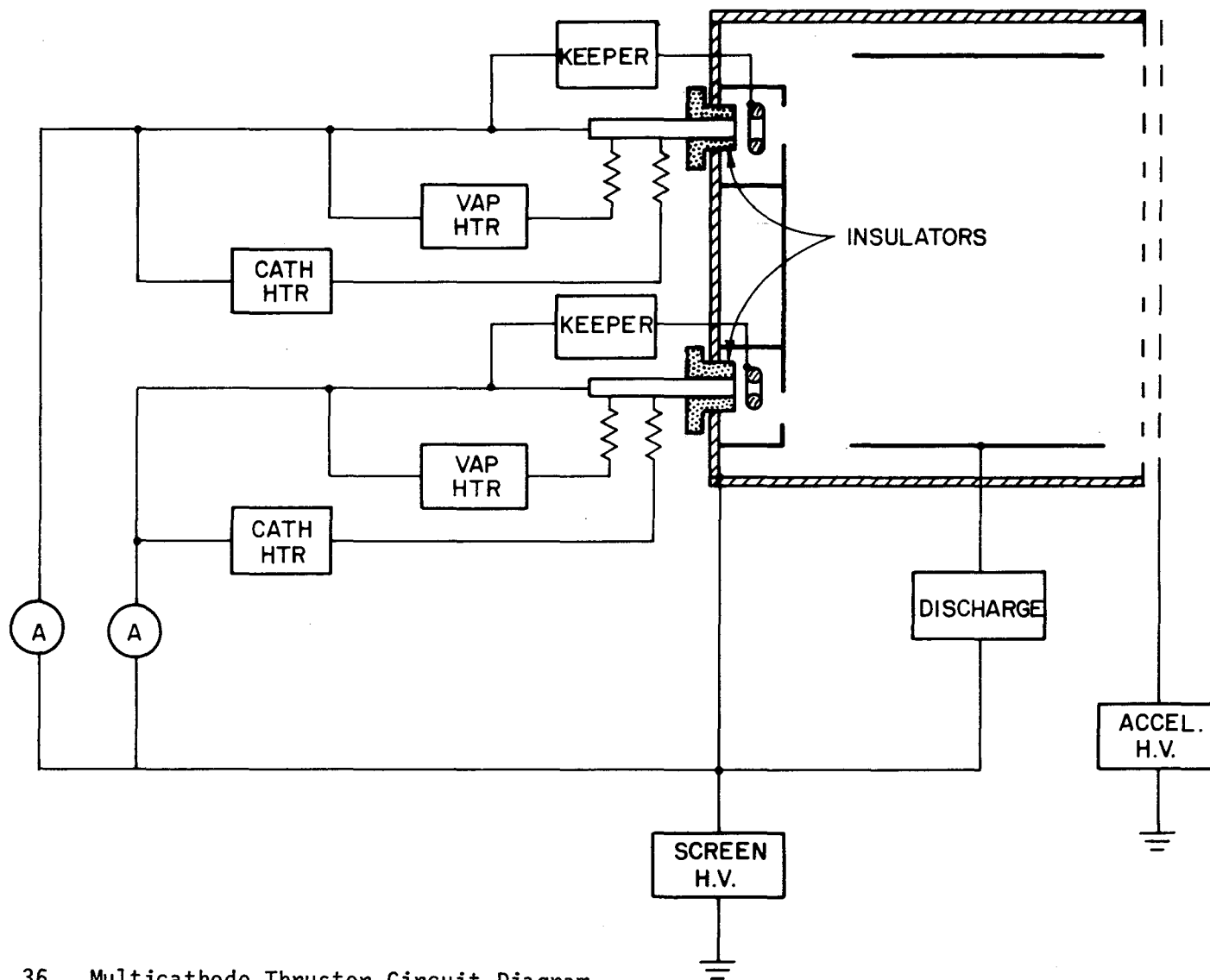
Fig. 36. Multicathode Thruster Circuit Diagram

started without great difficulty.

After both cathodes had been started and the main discharge had been initiated the problem became one of control of the relative emission currents from the two cathodes so they were nearly equal. It was found that this control could be effected by placing variable resistors in the leads to each cathode in the manner suggested by Fig. 37. The resistance in each lead could then be adjusted until the emission currents were equal. Figure 38 indicates the magnitude of the resistances required to equalize the emission currents at several discharge current levels. Emission currents shown in Figure 38 have been normalized with the discharge current. For the cathodes used in this study it was found that the one designated as the left cathode would, under normal operating conditions, tend to emit most of the required current. For this reason the resistance in the lead to the right cathode was set to zero and the resistance in the lead for the left cathode was varied from zero to 10Ω to generate the data shown in Fig. 38. Two interesting things should be noted from this Figure. First, the resistance required is independent of the magnitude of the discharge current, and second, the total cathode emission current is less than the current collected at the anode (i.e. the discharge current). In fact the emission current in these cases accounted for just under 70% of the discharge current. The remaining 30% of the discharge current is due to the electrons left behind by ions which either recombine on the discharge chamber walls or are extracted into the ion beam. The details of the main discharge current balance are discussed in Ref. 2.

One disadvantage of using resistances to control the relative emission between cathodes operating in parallel is that power is wasted in the resistors. For this reason control of the relative emission currents was
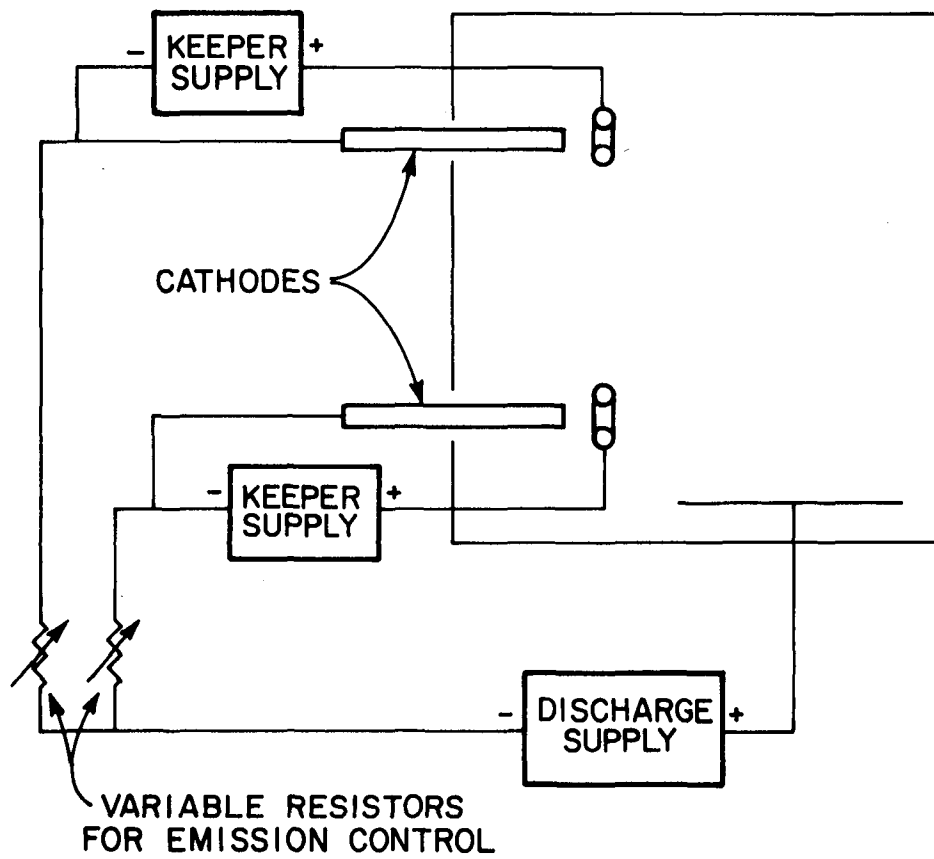
Fig. 37. Location of Tuning Resistors for Control of
          Relative Cathode Emission
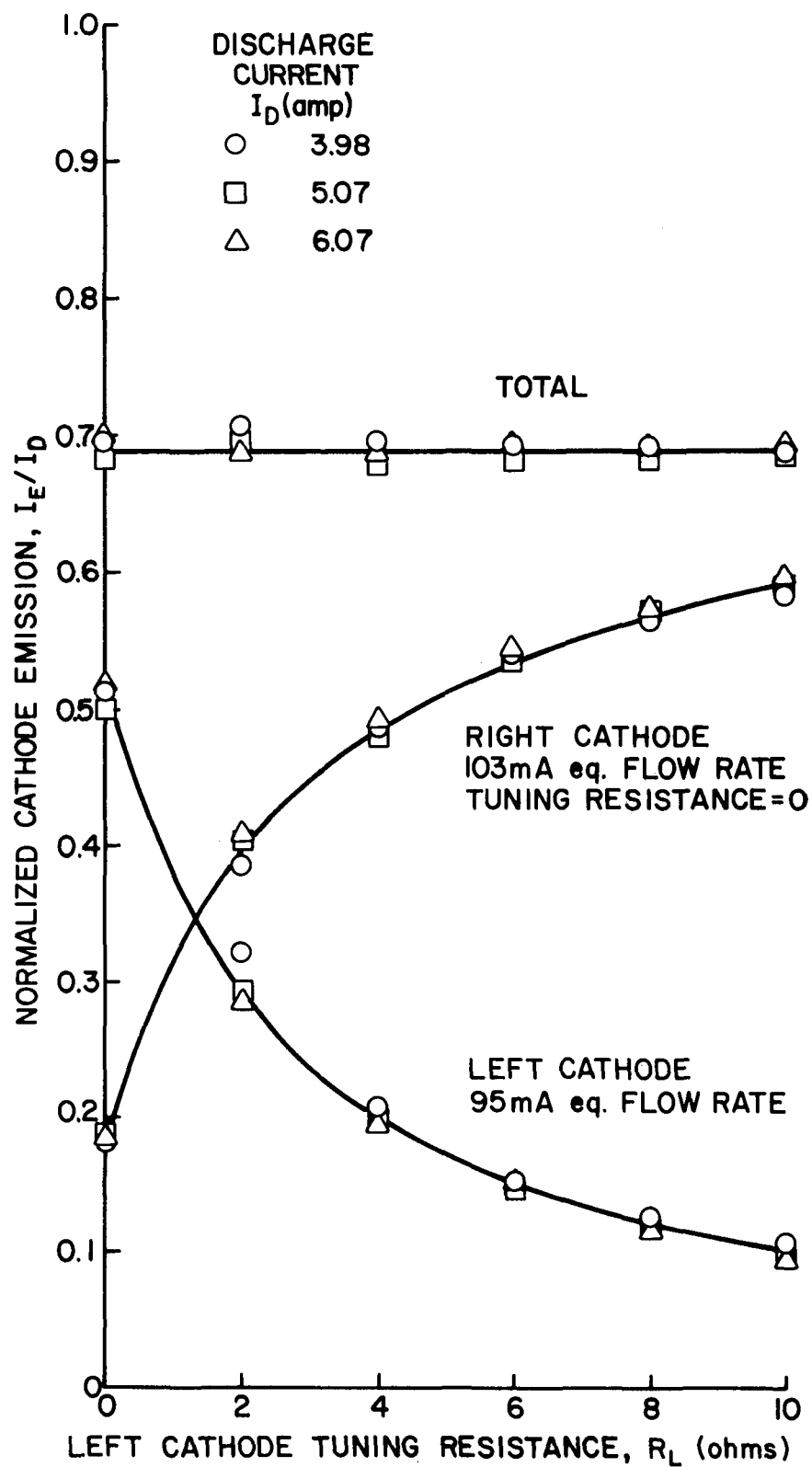
Fig. 38. Cathode Emission Control Using Tuning Resistors

attempted through adjustment of the cathode tip heater powers and neutral flow rates only. It was found that the response time of the relative emission currents to manual adjustments of these parameters was sufficiently rapid to allow control to be achieved in this manner. Typical test results showing the emissions from two parallel cathodes together with variations in cathode heater currents and cathode propellant flow rates required to achieve control are shown in Fig. 39. Initially the left cathode had an emission current of 3.8 amps and the right cathode was emitting 2.0 amps as shown in Fig. 39a. By turning the left cathode tip heater off and adjusting the right cathode heater current and neutral flow rates during the test in the manner shown in Figs. 39b and 39c, the emission currents were maintained essentially equal from the time 30 minutes into the test to its conclusion. The frequent small adjustments of the heater current required to maintain control can be seen in Fig. 39b. The less frequent adjustments required in the neutral flow rates can be seen in Fig. 39c.

Concluding Remarks

It is possible to operate an electron bombardment ion thruster with multiple cathodes supplying the emission current to the main discharge chamber. Starting more than one cathode can be difficult if the cathodes are not separated either physically or with a magnetic field. The most effective physical separation would probably be for each cathode to be in its own separate cathode discharge chamber. Control of the emission current split between the cathodes can be achieved through the use of variable resistors in the leads to the cathodes and by controlling the tip heater powers and neutral flow rates to these cathodes.
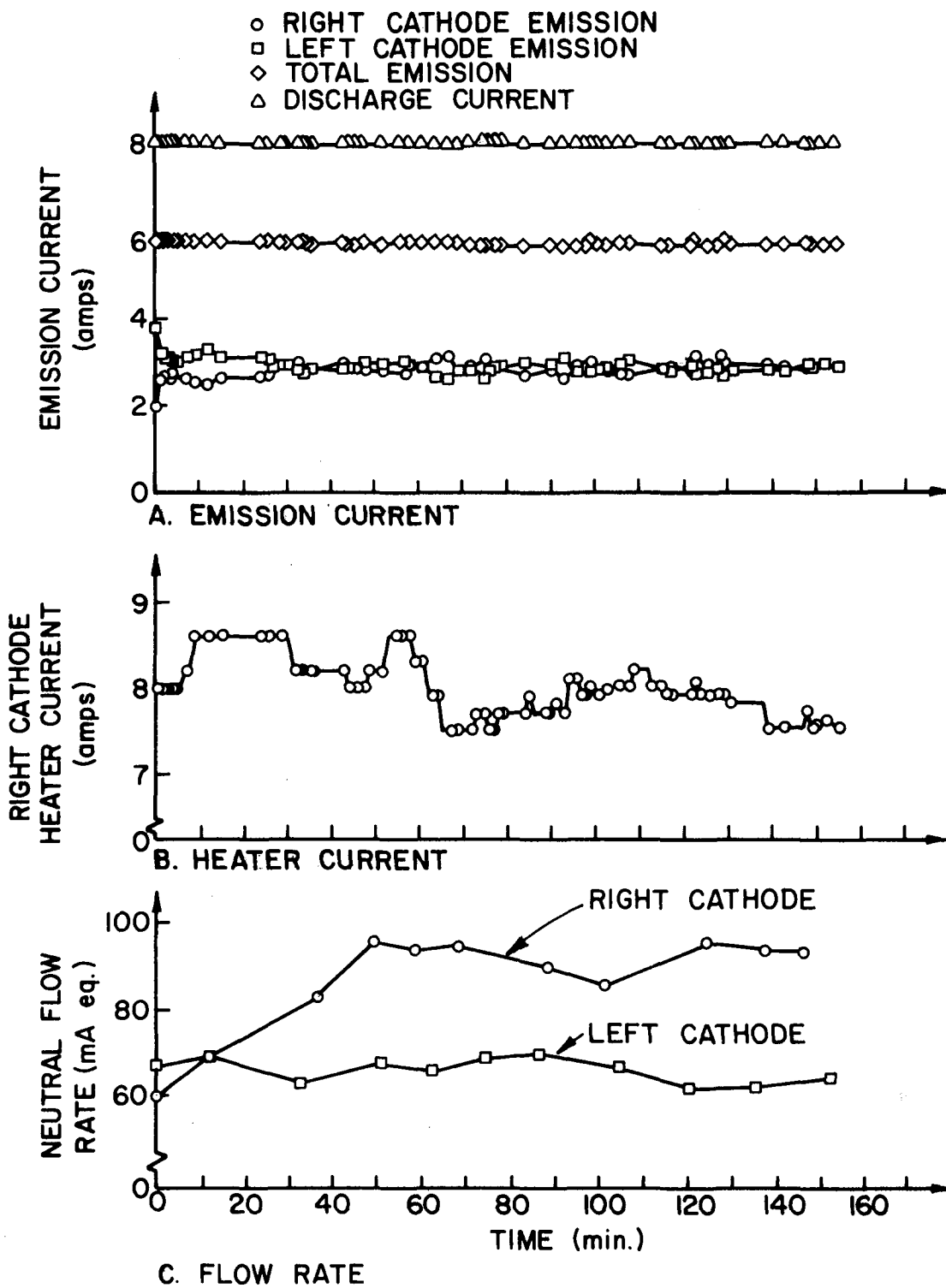
Fig. 39. Control Parameter Profiles

MODIFIED BOHM VELOCITY FOR PLASMA CONTAINING
PRIMARY ELECTRONS AND DOUBLY CHARGED IONS

John R. Brophy

The Bohm criterion is useful in ion thruster work because it provides a model describing the rate of ion migration toward discharge chamber boundaries. The initial model developed by Bohm[30] assumed only Maxwellian electrons were present in the plasma. Masek[31] modified this to account for the density of primary electrons. The purpose of this work is to investigate the effects of both the energy of the primary electrons and of doubly-charged ions that are generally present in ion thruster discharge chamber plasmas. Consideration of these species is becoming increasingly important as thruster size and power density increase and induce a corresponding increase in the densities of doubly-charged ions and primary electrons.

The one-dimensional Poisson equation that applies in the sheath region is,

$$\frac{d^2\phi}{dx^2} = \frac{-e}{\epsilon_0} [n_+(x) + 2n_{++}(x) - n_m(x) - n_p(x)] \tag{21}$$

where ϕ, the potential in the sheath, is taken as zero at the plasma sheath boundary, e is the electronic charge and ϵ_0 is the permeability of free space. The position variable (x) in this equation is taken to be zero at the sheath edge and n_+, n_{++}, n_m and n_p are the singly-charged ion, doubly-charged ion, Maxwellian electron and primary electron densities respectively. The Maxwellian electron density within the sheath is determined by the barometric equation in the form,

$$n_m(x) = n_m(o) \, e^{e\phi/kT} \tag{22}$$

where $n_m(o)$ is the electron density at the plasma sheath interface, T is the temperature of the Maxwellian population and k is the Boltzmann

constant. For the primary electrons a corresponding equation can be developed by considering the continuity of primary electrons through the sheath;

$$n_p(x) v_p(x) = n_p(o) v_p(o) \left(1 + \frac{2e\phi}{m_e v_p^2(o)} \right) \qquad (23)$$

In this equation $v_p(x)$ and $v_p(o)$ are the velocities of the primary electrons in the sheath and at the sheath edge respectively. The term multiplying the right hand side of this equation accounts for electron reflection induce by the electric field in the sheath. Conservation of energy for the primary electrons in the sheath is expressed through the equation

$$\frac{1}{2} m_e v_p^2(x) - e\,\phi(x) = \frac{1}{2} m_e v_p^2(o) \qquad (24)$$

where m_e is the electron mass. Combining Eqs. 23 and 24 one obtains the primary electron density variation through the sheath in the form,

$$n_p(x) = n_p(o) \left[1 + \frac{e\phi}{\varepsilon_p} \right]^{\frac{1}{2}} \qquad (25)$$

where $n_p(o)$ is the primary electron density at $x = 0$ and ε_p the energy of the primary electrons in the bulk plasma, is given by,

$$\varepsilon_p = \frac{1}{2} m_e v_p^2(o) \quad . \qquad (26)$$

The singly and doubly-charged ion densities in the sheath are also found by combining their respective continuity equations,

$$\begin{aligned} n_+(x)\, v_+(x) &= n_+(o)\, v_+(o) && \text{for singly-charged ions} \\ n_{++}(x)\, v_{++}(x) &= n_{++}(o)\, v_{++}(o) && \text{for doubly-charged ions} \end{aligned} \qquad (27)$$

with the corresponding energy conservation equations,

$$\begin{aligned} \frac{1}{2} m_i v_+^2(x) &= \frac{1}{2} m_i v_+^2(o) - e\,\phi(x) && \text{for singly-charged ions} \\ \frac{1}{2} m_i v_{++}^2(x) &= \frac{1}{2} m_i v_{++}^2(o) - 2e\,\phi(x) && \text{for doubly-charged ions} \end{aligned} \qquad (28)$$

to obtain,

$$n_+(x) = n_+(o) \left[\frac{\varepsilon_+}{\varepsilon_+ - e\phi}\right]^{\frac{1}{2}} \qquad \text{for singly-charged ions}$$

(29)

$$n_{++}(x) = n_{++}(o) \left[\frac{\varepsilon_{++}}{\varepsilon_{++} - 2e\phi}\right]^{\frac{1}{2}}, \qquad \text{for doubly-charged ions}$$

In these equations $n_+(o)$ and $n_{++}(o)$ are the singly and doubly-charged ion densities at $x = o$ respectively and ε_+ and ε_{++} are the corresponding energies at $x = o$. Substituting Eqs. 22, 25 and 29 into Eq. 21 yields,

$$\frac{d^2\phi}{dx^2} = -\frac{e}{\varepsilon_0}\left[n_+(o)\left(\frac{\varepsilon_+}{\varepsilon_+ - e\phi}\right)^{\frac{1}{2}} + 2n_{++}(o)\left(\frac{\varepsilon_{++}}{\varepsilon_{++} - 2e\phi}\right)^{\frac{1}{2}}\right.$$
$$\left. - n_m(o)\, e^{e\phi/kT} - n_p(o)\left(1 + \frac{e\phi}{\varepsilon_p}\right)^{\frac{1}{2}}\right].$$

(30)

Multiplying Eq. 30 by $d\phi/dx$, integrating and solving for the constant of integration satisfying the boundary condition $d\phi/dx = 0$ at $\phi = 0$ yields,

$$\left(\frac{d\phi}{dx}\right)^2 = \frac{4e}{\varepsilon_0}\left[\frac{n_+(o)}{e}\,\varepsilon_+\left(\sqrt{1 - \frac{e\phi}{\varepsilon_+}} - 1\right) + \frac{n_{++}(o)}{e}\,\varepsilon_{++}\left(\sqrt{1 - \frac{2e\phi}{\varepsilon_{++}}} - 1\right)\right.$$
$$\left. + \frac{kT n_m(o)}{2e}\left(e^{e\phi/kT} - 1\right) + \frac{n_p(o)\varepsilon_p}{3e}\left(\left\{1 + \frac{e\phi}{\varepsilon_p}\right\}^{3/2} - 1\right)\right].$$

(31)

But the quantity $(d\phi/dx)^2$ must always be greater than or equal to zero because an imaginary potential gradient is not physically meaningful. Application of this constraint yields

$$n_+(o)\,\varepsilon_+\left(\sqrt{1 - \frac{e\phi}{\varepsilon_+}} - 1\right) + n_{++}(o)\,\varepsilon_{++}\left(\sqrt{1 - \frac{2e\phi}{\varepsilon_{++}}} - 1\right) + \frac{kT n_m(o)}{2}\left(e^{e\phi/kT} - 1\right)$$
$$+ \frac{n_p(o)\varepsilon_p}{3}\left(\left\{1 + \frac{e\phi}{\varepsilon_p}\right\}^{3/2} - 1\right) \geq 0.$$

(32)

This equation can be simplified by expanding the various terms using the following power series:

$$e^{e\phi/kT} = 1 + \frac{e\phi}{kT} + \frac{1}{2}\left(\frac{e\phi}{kT}\right)^2 + \dots$$

$$\left(1 - \frac{e\phi}{\epsilon_+}\right)^{1/2} = 1 - \frac{e\phi}{2\epsilon_+} - \frac{1}{8}\left(\frac{e\phi}{\epsilon_+}\right)^2 + \dots$$

$$\left(1 - \frac{2e\phi}{\epsilon_{++}}\right)^{1/2} = 1 - \frac{e\phi}{\epsilon_{++}} - \frac{1}{2}\left(\frac{e\phi}{\epsilon_{++}}\right)^2 + \dots \tag{33}$$

$$\left(1 + \frac{e\phi}{\epsilon_p}\right)^{3/2} = 1 + \frac{3e\phi}{2\epsilon_p} + \frac{3}{8}\left(\frac{e\phi}{\epsilon_p}\right)^2 + \dots$$

These expressions are now substituted into Eq. 32 and it is recognized that

$$\frac{e\phi}{\epsilon_+} \ll 1, \; \frac{2e\phi}{\epsilon_{++}} \ll 1, \; \frac{e\phi}{\epsilon_p} \ll 1, \; \frac{e\phi}{kT} \ll 1 \tag{34}$$

so one need only retain the terms in Equation 33 that are of quadratic or lower powers. The result is

$$-n_+(o)\left(\frac{e\phi}{2} + \frac{(e\phi)^2}{8\epsilon_+}\right) - n_{++}(o)\left(e\phi + \frac{(e\phi)^2}{2\epsilon_{++}}\right) + \frac{n_m(o)}{2}\left(e\phi + \frac{(e\phi)^2}{2kT}\right)$$

$$+ n_p(o)\left(\frac{e\phi}{2} + \frac{(e\phi)^2}{8\epsilon_p}\right) \geq 0 \; . \tag{35}$$

Recalling that charge neutrality exists at the plasma sheath boundary the equation

$$2n_{++}(o) + n_+(o) = n_m(o) + n_p(o) \tag{36}$$

may be substituted into Eq. 35 to yield,

$$-\frac{n_+(o)}{\epsilon_+} - \frac{4n_{++}(o)}{\epsilon_{++}} + \frac{2n_m(o)}{kT} + \frac{n_p(o)}{\epsilon_p} \gtrless 0 \; . \tag{37}$$

Noting that the doubly-charged ion energy at the sheath edge should be twice the single ion energy, i.e.

$$\epsilon_{++} = 2\epsilon_+ \tag{38}$$

Eq. 37 becomes,

$$\frac{-n_+(o)}{\varepsilon_+} - \frac{2n_{++}(o)}{\varepsilon_+} + \frac{2n_m(o)}{kT} + \frac{n_p(o)}{\varepsilon_p} \geq 0 \quad . \tag{39}$$

Solving Eq. 39 for the singly-charged ion energy at the plasma sheath boundary yields,

$$\varepsilon_+ \geq \frac{n_+(o) + 2n_{++}(o)}{\left(\frac{2n_m(o)}{kT} + \frac{n_p(o)}{\varepsilon_p}\right)} \quad . \tag{40}$$

Making use of the relationship

$$\varepsilon_+ = \frac{1}{2} m_i v_+^2 \tag{41}$$

Eq. 40 can be written in terms of the ion velocity at the sheath edge as,

$$v_+ \geq \sqrt{\frac{kT}{m_i} \left[\frac{(n_+(o) + 2n_{++}(o))/n_m(o)}{1 + \left(\frac{kT}{2\varepsilon_p}\right)\left(\frac{n_p(o)}{n_m(o)}\right)}\right]} \quad . \tag{42}$$

If Eq. 36 is substituted into Eq. 42 the result is,

$$v_+ \geq \sqrt{\left(\frac{kT}{m_i}\right)\left[\frac{1 + n_p(o)/n_m(o)}{1 + \left\{\frac{kT}{2\varepsilon_p}\right\}\left\{\frac{n_p(o)}{n_m(o)}\right\}}\right]} \quad . \tag{43}$$

This equation is the one sought initially namely the one reflecting the effects of primary electron energy and doubly-charged ions. For the usual case where

$$\frac{kT}{2\varepsilon_p}\left\{\frac{n_p(o)}{n_m(o)}\right\} \ll 1$$

this simplifies to

$$v_+ \geq \sqrt{\frac{kT}{m_i}\left\{1 + \frac{n_p(o)}{n_m(o)}\right\}} \tag{44}$$

which is the result given by Masek.[31] It is interesting to note that the doubly-charged ion density does not appear explicity in Eq. 43. The Bohm

velocity for doubly-charged ions is obtained from Eq. 43 by using

$$\epsilon_{++} = 2\epsilon_+ = \frac{1}{2} m_i v_{++}^2 = m_i v_+^2 \tag{45}$$

or

$$v_{++} = \sqrt{2} \; v_+$$

to obtain

$$v_{++} \gtrsim \sqrt{\left(\frac{2kT}{m_i}\right)\left(\frac{1 + n_p(o)/n_m(o)}{1 + \frac{kT}{2\epsilon_p}\left(\frac{n_p(o)}{n_m(o)}\right)}\right)} \; . \tag{46}$$

In the limit of a high primary-to-Maxwellian electron density ratio Eqs. 43 and 46 suggest ion velocities of

$$v_+ = \frac{v_{++}}{\sqrt{2}} \gtrsim \sqrt{\frac{2\epsilon_p}{m_i}} \; . \tag{47}$$

This appears to be a physically reasonable limiting condition.

REFERENCES

1. Aston, G., "Ion Extraction from a Plasma," NASA CR-159849, June 1980.

2. Brophy, J., "Baffle Aperture Design Study of Hollow Cathode Equipped Ion Thrusters," NASA CR-165164, October 1980.

3. Siegfried, D. E. and Wilbur, P. J., "An Investigation of Mercury Hollow Cathode Phenomena," AIAA Paper No. 78-705, April 25-27, 1978.

4. Siegfried, D. E. and Wilbur, P. J., "Studies on an Experimental Quartz Tube Hollow Cathode," AIAA Paper No. 79-2056, Oct. 30 - Nov. 1, 1979.

5. Cobine, J. D., Gaseous Conductors-Theory and Engineering Applications, 1st ed., Dover Publications, Inc., New York, 1958, Chps. 5, 8, 9.

6. Crawford, F. W. and Freestone, I. L., "The Double Sheath at a Discharge Constriction," Proceedings of the 6th International Conference of Ionization Phenomena in Gases, Paris, July 1963.

7. Hensley, E. B., "Thermionic Emission Constants and their Interpretation," Journal of Applied Physics, Vol. 32, No. 2, Feb. 1961, pp. 301-308.

8. Kohl, W. H., Handbook of Materials and Techniques for Vacuum Devices, Reinhold Publishing Corp., New York, 1967, Ch. 16.

9. Byers, D. C., "Effect of Power Supply Impedance on the Sert II Neutralizer," NASA Technical Memorandum, NASA TM X-52543, 1969.

10. Crawford, F. W., "Electrostatic Sound Wave Modes in a Plasma," Physical Review Letters, Vol. 6, No. 12, June 15, 1961, pp. 663-667.

11. Waymonth, J. F., "Perturbation of a Plasma by a Probe," The Physics of Fluids, Vol. 7, No. 11, Nov. 1964, pp. 1843-1854.

12. Self, S. A. and Shih, C. H., "Theory and Measurements for Ion Collection by a Spherical Probe in a Collisional Plasma," The Physics of Fluids, Vol. 11, No. 7, July, 1968, pp. 1532-1545.

13. Huddlestone, R. H. and Leonard, S. L., Plasma Diagnostic Techniques, Academic Press Inc., New York, 1965, Ch. 4.

14. Wehner, G. and Medicus, G., "Reliability of Probe Measurements in Hot Cathode Gas Diodes," Journal of Applied Physics, Vol. 23, No. 9 Sept. 1952, pp. 1035-1046.

15. Rawlin, V. K. and M. A. Mantenieks, "Effect of Facility Background Gases on Internal Erosion of the 30-cm Hg Ion Thruster," AIAA Paper 78-665, April 1978.

16. Meadows, G. A. and B. A. Free, "Effect of a Decel Electrode on Primary and Charge-Exchange Ion Trajectories," AIAA Paper No. 75-427, 1975.

17. Wehner, G. K. and D. J. Hajicek, "Cone Formation on Metal Targets During Sputtering," Jour. of App. Phys., V. 42, No. 3, March, 1971, pp. 1145-1149.

18. Wehner, G. K., "Sputtering Yield data in the 100 to 600 eV Energy Range," General Mills Report 2309, July 15, 1962.

19. Stuart, R. V. and G. K. Wehner, "Sputtering Yields at Very Low Bombarding Ion Energies," Jour. of App. Phys., V. 33, No. 7, July, 1962, pp. 2345-2352.

20. Askerov, S. G. and L. A. Sena, "Cathode Sputtering of Metals by Slow Mercury Ions," Soviet Physics - Solid State, Vol. 11, No. 6, Dec. 1969, pp. 1288-1293.

21. Beattie, J. R., "A Model for Predicting the Wearout Lifetime of the LeRC/Hughes 30-cm Mercury Ion Thruster," AIAA Paper 79-2079, October 1979.

22. Kerslake, W. R. et. al., "SERT II: Mission, Thruster Performance, and In-Flight Test Measurements," Journal of Spacecraft and Rockets, Vol. 8, No. 3, March 1971, pp. 213-224.

23. Jahn, R. G., Physics of Electric Propulsion, Chapter 6, 1968, McGraw Hill.

24. Kerslake, W. R., Private Communication, NASA Lewis Research Center, Oct. 1980.

25. Lathem, W. C. and W. B. Adam, "Theoretical Analysis of a Grid Translation Beam Deflection System for a 30 cm diameter Kaufman Thruster," NASA TM X-67911, 1971.

26. Aston, G., "The Ion-Optics of a Two-Grid Electron-Bombardment Thruster," NASA CR-135034, 1976.

27. Whealton, J. H., "Linear Optics Theory of Ion Beamlet Steering," Rev. of Sci. Instrum. Vol. 48, No. 11. p. 1428, 1977.

28. Kaufman, H. R., "Technology of Electron-Bombardment Ion Thrusters," Advances in Electronics and Electron Physics, Vol. 36, pp. 324-327, 1974.

29. Longhurst, G. R. and P. J. Wilbur, "15-cm Mercury Multipole Thruster," Jour. of Spacecraft and Rockets, Jan-Feb. 1979, pp. 42-47.

30. Bohm, D., "Minimum Ionic Kinetic Energy for a Stable Sheath," The Characteristics of Electrical Discharges in Magnetic Fields, A. Guthrie and R. K. Wakerling, eds., McGraw-Hill Book Co., Inc., 1949, pp. 77-86.

31. Masek, T. D., "Plasma Properties and Performance of Mercury Ion Thrusters," AIAA Paper No. 69-256, March 3-5, 1969.

APPENDIX A

Langmuir Probe Sweep Circuitry

The circuit diagram for the equipment designed to sweep the Langmuir probe over a desired voltage range is shown in Figure A1. The sweep circuit employs an operational amplifier-integrator circuit to produce a voltage ramp. This signal is then fed into a series pass power transitor to provide the necessary current output. Input terminals and switching are also provided for biasing the probe to keep it clean. A trace is taken by first pressing button S_3. This switches the probe from the cleaning circuit to the voltage sweep circuit and at the same time engages the servo for the x-y recorder. Then pressing button S_1 activates the recorder pen and begins the voltage sweep. The sweep rate is controlled by adjusting resistor R_4, the start voltage by resistor R_3, and the final voltage by resistor R_7. The sweep rate range can also be changed by changing the value of capacitor C_1. The circuit will provide currents up to 500 mA for voltages swept between -15 to +15 v over a wide range of sweep rates. A probe cleaning circuit is also shown as an integral part of the design. Switches 5 and 6 provide manual override for the recorder pen and servo to aid in setting up the axes for the trace. The x-voltage follower uses an operational amplifier in a noninverting unity gain amplifier circuit to drive the x-channel of the recorder without drawing any appreciable current through the current sensing resistor R10.
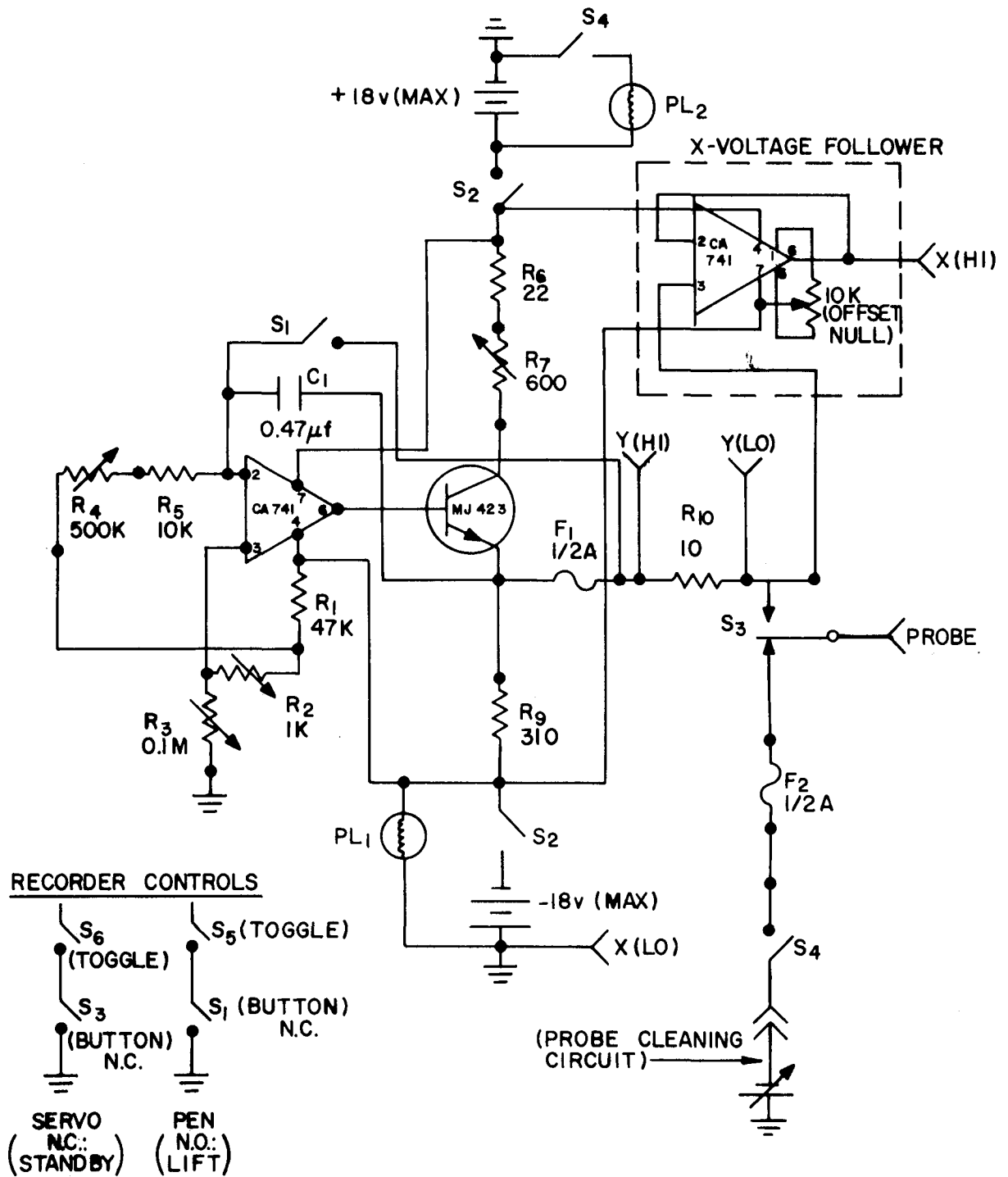
Fig. A1. Probe Voltage Sweep Circuit

APPENDIX B

Electrothermal Launch System Dynamics

Nomenclature (mks units)

F — Thrust Force

g — Acceleration due to gravity

$\dot{m}$ — Mass flow rate of Propellant

m — Mass of Vehicle

P — Input Electrical Power

t — Time

U — Thruster exhaust velocity

v — Vehicle velocity

x — Position

σ — Acceleration (G's)

Subscripts

i — initial condition

f — final condition

p — pertaining to the pumping process

1f — pertaining to the end of phase one in ramjet mode

2f — pertaining to the end of phase two in ramjet mode

In this development it has been assumed that

- the launch would be vertical,

- drag and frictional forces are negligible,

- any thruster exhaust is fully expanded isentropically,

- any engine operates at constant thrust and exhaust velocity, and
- the launch is effected close to the earth's surface so the acceleration due to gravity is constant.

The basic schematic of the launch process has been shown previously in the text (Figure 25 - page 78).

Rocket Model

The thrust of a rocket engine which receives its propellant from on-board tanks is given by

$$F = \dot{m}U. \tag{B1}$$

Balancing this thrust against the weight and acceleration of the vehicle yields

$$F = mg\sigma = m_i g\sigma_i = gm + m\frac{dv}{dt} . \tag{B2}$$

Integration of Eqn. B1 gives vehicle mass as a function of time

$$m = m_i - \frac{Ft}{U} \tag{B3}$$

and combining Eqs. B2 and B3 one obtains an expression for the vehicle acceleration as a function of time

$$\sigma = \frac{F}{g(m_i - \frac{Ft}{U})} . \tag{B4}$$

Integrating Eq. B2 one obtains the following expression for vehicle velocity as a function of time

$$v = -U \ln(1 - \frac{Ft}{Um_i}) - g t . \tag{B5}$$

A second integration of this equation gives position as a function of time.

$$x = \frac{U^2}{F} (m_i - \frac{Ft}{U}) \ln(1 - \frac{Ft}{Um_i}) + Ut - \frac{gt^2}{2} \tag{B6}$$

The input power required is given by

$$P = \frac{\dot{m}U^2}{2} + P_p \tag{B7}$$

where P_p is the pumping power. A preliminary analysis has shown the pumping power is only a few percent of the total power so it will be neglected here.

Electromagnetic Accelerator Model

For this case the vehicle mass remains constant as does the thrust defined by the electromagnetic mechanism used to produce it. In this case the force balance on the vehicle becomes

$$F = m_i g \sigma = m_i g \sigma_i = g m_i + m_i \frac{dv}{dt} \; . \tag{B8}$$

The vehicle mass is given by

$$m = m_i \tag{B9}$$

and the acceleration for Eq. B8 by

$$\sigma = \sigma_i \; . \tag{B10}$$

Integration of Equation B8 gives the velocity as a function of time

$$v = (\frac{F}{m_i} - g)t \; . \tag{B11}$$

A second integration gives the variation in position with time

$$x = (\frac{F}{m_i} - g) \frac{t^2}{2} \; . \tag{B12}$$

The required input power in this case will be idealized to the extent that losses associated with magnetic energy stored at the conclusion of the launch phase and joule heating losses are neglected. For this ideal launch case the input power is given by

$$P = Fv = F(\frac{F}{m_i} - g)t \; . \tag{B13}$$

Ramjet Model

During the first phase of operation of a ramjet it is necessary to increase the vehicle velocity from zero to the point required to produce the stagnation pressure needed for proper engine operation. This initial acceleration could be accomplished using an expanding explosive, an electromagnetic starter or an auxiliary rocket. The rocket is assumed here because it seems simplest although it introduces some penalty in terms of vehicle mass required. With the application of thrust using on-board propellant and a rocket motor Eqs. B1 through B7 describe the first phase of operation. This phase is continued until the vehicle velocity is sufficient to satisfy the equation

$$v_{1f} = \frac{2 \, P_0^*}{\rho} \tag{B14}$$

where P_0^* is the required engine stagnation pressure and ρ is the propellant density. For the case under consideration here it was determined that a vehicle velocity about 15% of the jet velocity was sufficient to assure the required pressure.

During the second phase of ramjet operation the inertial force of the incoming propellant must be considered and the net thrust on the vehicle obtained from a momentum balance becomes

$$F = \dot{m} \, (U - v) \; . \tag{B15}$$

During this phase the vehicle mass remains constant at a value of

$$m = m_{1f} = m_i - \frac{F t_{1f}}{U} \; . \tag{B16}$$

Because the mass is constant the acceleration of the vehicle also remains constant and is given by

$$\sigma = \frac{F}{gm_{1f}} = \frac{F}{g(m_i - \frac{Ft_{1f}}{U})} \quad . \tag{B17}$$

Integration of Equation B2 under the boundary condition that the velocity is v_{1f} at time t_{1f} and using the fact that the mass remains constant during this phase gives

$$v = v_{1f} + (\frac{F}{m_{1f}} - g) (t - t_{1f}) \quad . \tag{B18}$$

A second integration gives the variation in vehicle position with time

$$x = x_{1f} + v_{1f}(t - t_{1f}) + \frac{1}{2} (\frac{F}{m_{1f}} - g) (t - t_{1f})^2 \quad . \tag{B19}$$

The power consumption during this phase must reflect the fact that some of the power input to the propellant comes from the velocity of the propellant relative to the vehicle $(\frac{\dot{m}v^2}{2})$ and this can be subtracted from the power of the exhaust stream $(\frac{\dot{m}U^2}{2})$. Thus the input power becomes

$$P = \frac{\dot{m}U^2}{2} - \frac{\dot{m}v^2}{2} \tag{B20}$$

where the actual pumping power required has again been neglected.

A third phase of ramjet operation is required when the desired terminal velocity is greater than the vehicle exhaust velocity. The reason for this is seen from Eq. B15 which shows the thrust goes to zero as the vehicle velocity approaches the exhaust velocity. Under the constraint of operation at constant thrust and exhaust velocity being considered here, this equation also suggests the mass flow rate would have to become infinite as $v \to U$. In order to limit the required mass flow rate to a reasonable value this third phase has been defined rather arbitrarily as starting when the vehicle velocity is 90% of the exhaust velocity. The

basic equations written for phase one apply here again although integration between different limits is required.

The expression for the vehicle mass is obtained by integration of Eq. B10.

$$m = m_{1f} - \frac{F}{U} (t - t_{2f}) \quad . \tag{B21}$$

The acceleration is obtained by combining Eqs. B2 and B21 to obtain

$$\sigma = \frac{F}{g[m_{1f} - \frac{F}{U} (t - t_{2f})]} \quad . \tag{B22}$$

Integration of Eq. B2 using the initial conditions for this phase gives

$$v - v_{2f} - U \ln [1 - \frac{F}{m_{1f}U} (t - t_{2f})] - g(t - t_{2f}) \tag{B23}$$

Integration of this equation yields

$$x = x_{2f} + v_{2f}(t - t_{2f}) + U \{[\frac{m_{1f}U}{F} - (t - t_{2f})] \ln [1 - \frac{F}{m_{1f}U} (t - t_{2f})]$$

$$+ t - t_{2f}\} - \frac{g}{2}(t - t_{2f})^2 \quad . \tag{B24}$$

For each mode of operation the total time required for the launch is determined by the equation for vehicle velocity through the specification of desired final velocity.

DISTRIBUTION LIST

National Aeronautics and Space Administration
Washington, DC 20546
Attn: RS/Mr. Dell Williams, III   1
       RTS-6/ Mr. Wayne Hudson   1
       RTS-6/ Mr. Jerome Mullin   1
       MT/ Mr. Ivan Bekey   1

National Aeronautics and Space Administration
Lewis Research Center
21000 Brookpark Road
Cleveland, OH 44135
Attn: Research Support Procurement Section
       Mr. G. Golinski, MS 500-306   1
       Technology Utilization Office, MS 3-19   1
       Report Control Office, MS 5-5   1
       Library, MS 60-3   2
       Mr. N. Musial, MS 500-113   1
       Dr. M. Goldstein, Chief Scientist, MS 5-3   1
       Mr. T. Cochran, M.S. 501-8   1
       Dr. F. Teren, MS 501-5   1
       Mr. R. Finke, MS 77-4   1
       Mr. B. Banks, MS 501-7   1
       Mr. D. Byers, MS 501-7   1
       Mr. W. Kerslake, MS 501-7   30

National Aeronautics and Space Administration
Lyndon B. Johnson Space Center
Houston, TX 77058
Attn: Mr. Hu Davis   1

National Aeronautics and Space Administration
Marshall Space Flight Center
Huntsville, AL 35812
Attn: Mr. Jerry P. Hethcoate   1
       Mr. John Harlow   1
       Mr. John Brophy   1

Research and Technology Division
Wright-Patterson AFB, OH 45433
Attn: (ADTN) Mr. Everett Bailey   1

NASA Scientific and Technical
Information Facility
P. O. Box 8757
Baltimore, MD 21240
Attn: Accessioning Dept.   1

Case Western Reserve University
10900 Euclid Avenue
Cleveland, OH 44106
Attn: Dr. Eli Reshotko   1

Royal Aircraft Establishment
Space Department
Farnborough, Hants
ENGLAND
Attn: Dr. D. G. Fearn   1

United Kingdom Atomic Energy Authority
Culham Laboratory
Abingdon, Berkshire
ENGLAND
Attn: Dr. P. J. Harbour   1
      Dr. M. F. A. Harrison   1

National Aeronautics and Space Administration
Goddard Space Flight Center
Greenbelt, MD 20771
Attn: Mr. W. Isley, Code 734   1
      Mr. A. A. Vetman   1
      Dr. David H. Suddeth   1

COMSAT Laboratories
P. O. Box 115
Clarksburg, MD 20734
Attn: Mr. B. Free   1
      Mr. O. Revesz   1

Comsat Corporation
950 L'Enfant Plaza, SW
Washington, DC 20024
Attn: Mr. Sidney O. Metzger   1

Rocket Propulsion Laboratory
Edwards AFB, CA 93523
Attn: LKDA/Mr. Tom Waddell   1
      LKDH/Dr. Robert Vondra   1

DFVLR - Institut fur Plasmadynamik
Technische Universitat Stuttgart
7 Stuttgart-Vaihingen
Allmandstr 124
West Germany
Attn: Dr. G. Krulle   1

Copies

DFVLR - Institut fur Plasmadynamik
33 Braunschweig
Bienroder Weg 53
West Germany
Attn: Mr. H. Bessling   1

Giessen University
1st Institute of Physics
Giessen, West Germany
Attn: Professor H. W. Loeb   1

Jet Propulsion Laboratory
4800 Oak Grove Drive
Pasadena, California 91102
Attn: Dr. Kenneth Atkins   1
       Technical Library   1
       Mr. Eugene Pawlik   1
       Mr. James Graf   1

       Mr. Dennis Fitzgerald   1
       Dr. Graeme Aston   1

Electro-Optical Systems, Inc.
300 North Halstead
Pasadena, California 91107
Attn: Dr. R. Worlock   1
       Mr. E. James   1
       Mr. W. Ramsey   1

TRW Inc.
TRW Systems
One Space Park
Redondo Beach, California 90278
Attn: Dr. M. Huberman   1
       Mr. H. Ogawa   1
       Mr. Sid Zafran   1

National Aeronautics and Space Administration
Ames Research Center
Moffett Field, California 94035
Attn: Technical Library   1

National Aeronautics and Space Administration
Langley Research Center
Langley Field Station
Hampton, Virginia 23365
Attn: Technical Library   1
       Mr. B. Z. Henry   1

Hughes Research Laboratories
3011 Malibu Canyon Road
Malibu, California 90265
Attn: Mr. J. H. Molitor   1
       Dr. R. L. Poeschel   1
       Dr. Jay Hyman   1
       Mr. R. Vahrenkamp   1
       Dr. J. R. Beattie   1
       Dr. W. S. Williamson   1

Princeton University
Princeton, NJ 08540
Attn: Mr. W. F. Von Jaskowsky   1
       Dean R. G. Jahn   1
       Dr. K. E. Clark   1

Joint Institute for Laboratory Astrophysics
University of Colorado
Boulder, Colorado 80302
Attn: Dr. Gordon H. Dunn   1

Boeing Aerospace Co.
P. O. Box 3999
Seattle, Washington 98124
Attn: Mr. Donald Grim, M.S. 8K31   1
       Mr. Russell Dod   1

Lockheed Missiles and Space Co.
Sunnyvale, California 94088
Attn: Dr. William L. Owens
       Propulsion Systems, Dept. 62-13   1

Fairchild Republic Co.
Farmingdale, New York 11735
Attn: Dr. Domenic J. Palumbo   1

Electrotechnical Laboratory
1-1-4, Umezono, Sakura-Mura,
Niihari-Gun
Ibaraki, Japan
Attn: Dr. Katsuya Nakayama   1

Bell Laboratories
600 Mountain Avenue
Murray Hill, NJ 07974
Attn: Dr. Edward G. Spencer   1
       Dr. Paul H. Schmidt   1

Sandia Laboratories
Mail Code 5743
Albuquerque, NM 87115
Attn: Mr. Ralph R. Peters   1

Ion Tech, Inc.
P. O. Box 1388
1807 E. Mulberry
Fort Collins, Colorado 80522
Attn: Dr. Gerald C. Isaacson   1

EG & G Idaho
P. O. Box 1625
Idaho Falls, Idaho 83401
Attn: Dr. G. R. Longhurst, TSA-104   1

The Aerospace Corporation
P. O. Box 95085
Los Angeles, CA 90045
Attn: Dr. B. A. Haatunion   1
       Mr. A. H. Silva   1

Michigan State University
East Lansing, MI 48824
Attn: Dr. J. Asmussen   1
       Dr. M. C. Hawley   1

General Dynamics
Kearney Mesa Plant
P. O. Box 1128
San Diego, CA 92112
Attn: Dr. Ketchum   1

Ford Aerospace Corp.
3939 Fabian Way
Palo Alto, CA 94303
Attn: Mr. Robert C. Kelsa   1

Hughes Aircraft Co.
Space and Communication Group
P. O. Box 92919
Los Angeles, CA 90009
Attn: Dr. M. E. Ellison   1
       Dr. B. G. Herron   1

The Aerospace Corporation
Space Sciences Lab.
P. O. Box 92957
Los Angeles, California 90009
Attn: Dr. Y. T. Chiu   1

The Takagi Research Laboratory
Department of Electronics
Kyoto University
Yoshidahonmachi Sakyo-ku Kyoto 606
JAPAN
Attn: Dr. Toshinori Takagi   1

Department of Aeronautics
Faculty of Engineering
University of Tokyo
7-3-1, Hongo, Bunkyo-ku
Tokyo JAPAN
Attn: Prof. Itsuro Kimura   1

Prof. Tom Maul
P. O. Box 98182
Tsim Sha Tsui Post Office
Kowloon, Hong Kong
British Crown Colony   1

Mr. Susumu Masaki
Department of Electronics
Tokyo National Technical College
No. 1220-2
Kunugida-cha, Hachioji 193
Tokyo, JAPAN   1

Mr. Curtis Haynes
Tektronix Inc.
M.S. SO-431
P. O. Box 500
Beaverton, Oregon 97077   1

Dr. Pradosh Ray
Tuskegee Institute
School of Engineering
Tuskegee Institute, Ala. 36088   1

Dr. John Barber
International Applied Phyics Inc.
7546 McEwen Road
Dayton, Ohio 45459   1

Dr. Ron Hawke
Lawrence Livermore Laboratory
Livermore, California 94550   1

Dr. Richard A. Marshall
University of Texas
Taylor Hall 167
Austin, Texas   78712   1

Dr. V. V. Zhurin
Computing Center of the USSR
    Academy of Sciences
Vavilova 40
117333 Moscow, B-333
USSR   1